



저작자표시-비영리-동일조건변경허락 2.0 대한민국

이용자는 아래의 조건을 따르는 경우에 한하여 자유롭게

- 이 저작물을 복제, 배포, 전송, 전시, 공연 및 방송할 수 있습니다.
- 이차적 저작물을 작성할 수 있습니다.

다음과 같은 조건을 따라야 합니다:



저작자표시. 귀하는 원저작자를 표시하여야 합니다.



비영리. 귀하는 이 저작물을 영리 목적으로 이용할 수 없습니다.



동일조건변경허락. 귀하가 이 저작물을 개작, 변형 또는 가공했을 경우에는, 이 저작물과 동일한 이용허락조건하에서만 배포할 수 있습니다.

- 귀하는, 이 저작물의 재이용이나 배포의 경우, 이 저작물에 적용된 이용허락조건을 명확하게 나타내어야 합니다.
- 저작권자로부터 별도의 허가를 받으면 이러한 조건들은 적용되지 않습니다.

저작권법에 따른 이용자의 권리는 위의 내용에 의하여 영향을 받지 않습니다.

이것은 [이용허락규약\(Legal Code\)](#)을 이해하기 쉽게 요약한 것입니다.

[Disclaimer](#)

공학박사 학위논문

**Compositional and Structural Control
at Nanoscale for Bone Implant:
Whitlockite and Nanochannel**

나노 스케일에서의

골 임플란트 조성 및 구조 제어를 위한

whitlockite과 nanochannel에 관한 연구

2014년 2월

서울대학교 대학원

재료공학부

장 해 린

Compositional and Structural Control at Nanoscale for Bone Implant: Whitlockite and Nanochannel

지도 교수: 홍 국 선, 남 기 태

이 논문을 박사 학위논문으로 제출함

2014 년 2 월

서울대학교 대학원

재료공학부

장 해 린

장해린의 박사 학위논문을 인준함

2014 년 2 월

위 원 장 _____ 강 기 석 (인)

부위원장 _____ 홍 국 선 (인)

위 원 _____ 남 기 태 (인)

위 원 _____ 이 호 영 (인)

위 원 _____ 김 진 영 (인)

Abstract

Compositional and structural control at nanoscale for bone implant: Whitlockite and Nanochannel

Hae Lin Jang

Department of Materials Science and Engineering

The Graduate School

Seoul National University

Naturally existing hard materials, such as bone in the hard tissue of the living system, are hierarchically self-assembled by nanoparticles which are thermodynamically the most stable state. Inspired from these biominerals, previous researchers have been successfully made similar artificial materials in micrometer scale and applied into various fields. However, investigation of biominerals in nanometer scale is still remained a challenge and thus the related effects in living organism are unclear. Therefore, in this thesis, we discussed about compositional and structural control at nanometer scale for bone implant in order to understand and recreate natural minerals.

In the first part of the thesis, in order to develop similar structure to bone, we discussed about whitlockite (WH: $\text{Ca}_{18}\text{Mg}_2(\text{HPO}_4)_2(\text{PO}_4)_{12}$) which is one of the most abundant inorganic phases in bone along with hydroxyapatite (HAP: $\text{Ca}_{10}(\text{PO}_4)_6(\text{OH})_2$). Until now, most of the previous researches related to the bone implant had been conducted by utilizing HAP because WH was difficult to be synthesized in physiologically relevant condition. Here, we described large-scale synthesis of pure phase of WH nanoparticles in ternary $\text{Ca}(\text{OH})_2$ - $\text{Mg}(\text{OH})_2$ - H_3PO_4 aqueous system based on the systematic approach. In addition, we showed material properties of synthesized WH compare to its synthetic analogue tricalcium phosphate (TCP: $\text{Ca}_3(\text{PO}_4)_2$). During synthesis process, kinetic mechanism of the precipitated WH was analyzed to comprehend the formation mechanism of WH in our body system. Although,

HAP is most stable at above neutral pH, as the pH of the synthetic system changed from basic to acidic environment, it dissolved and transformed into newly stable WH structure based on the dense construction of Ca^{2+} and PO_4^{3-} ions around Mg^{2+} and HPO_4^{2-} in the center of ions. When WH was fabricated into scaffold, it showed higher cellular proliferation rate than well-known HAP and TCP implant materials in the *in vitro* test. The human bone cells grown on the surface of WH also actively involved in the bone mineralization process showing an excellent biocompatibility. In addition, based on the strong mechanical property of WH compare to that of HAP and TCP, WH was easily produced into various types of implants. It also showed high capability to co-exist with free fluoride ions which can be further used as a toothpaste material. In this regard, WH had high potential to be applied in various fields as a biomaterial.

In the latter half of the thesis, to recreate bone-like structure in nanometer scale, we designed and fabricated dimension tunable nanochannel with its width changed from micrometer scale to nanometer scale in HAP scaffold. Tree-like pore networks in nanometer scale are well known for the most optimized structure to maximize capillary effect and thus to occur efficient supply. Especially, tapered channels are simultaneously good at permeability from its wide entrance which also induces fast circulation. In this research, we applied additional pressure energy during the sintering process to induce phase separation between polyethylene glycol polymer and HAP nanoparticles. Notably, pressure energy was gradually increased to make different levels of phase separation which changed dimension of the nanochannel. The resulted well Aligned Multiple Capillary networks with gradually decreasing Diameter were directly observed by FIB-FESEM, TEM, Nano-CT analyses and confirmed that these networks were continuously connected with each other. In addition, the capillary power was found to be stronger when the direction of the decreasing dimension of the channel was parallel to the supply direction of the fluid than when it was placed in the opposite direction. Remarkably, small organisms such as human cells and bacteria were able to proliferate at the end of the nanochannels, solely depending on the nutrients supply through the nanochannel, indicating the significance of the nanochannels in the living system.

The compositional and structural control at nanometer scale for bone implant in this thesis will be useful to understand the formation mechanism and the role of biomineral in the living system. We believe that this study will directly contribute to make more bone-like implants and provide inspiration and foundation knowledge to the other various research fields related to nanometer scale.

**Keywords: calcium phosphate, biomineral, whitlockite, nanochannel,
bone, implant**

Student Number: 2010-30784

Contents

Abstract	i
Contents	iv
List of Tables.....	vii
List of Figures	viii
Chapter 1. Introduction	1
1.1 Introduction of biomineral and calcium phosphate compound ..	1
1.2 Revisiting whitlockite: its occurrence and importance	3
1.3 Designing living scaffold: considering efficient supply	7
1.4 Objective of the thesis.....	12
1.5 Organization of the thesis.....	15
Chapter 2. Theoretical background of composition and structure of biominerals	17
2.1 The mineral in tooth and bone.....	17
2.1.1 The mineral in enamel and dentin of human tooth	18
2.1.2 The mineral in human bone	25
2.2 General chemistry of calcium phosphate compounds	32
2.2.1 Kinetically favored intermediate phases; brushite and monetite	34
2.2.2 Hydroxyapatite and nonstoichiometric apatites	37
2.2.3 β -Tricalcium phosphate	40
2.2.4 Whitlockite	41
2.3 Previous approaches for the fabrication of macroporous bioceramics.....	45
Chapter 3. Experimental Procedures	53

3.1 Sample preparation of whitlockite.....	53
3.2 Analysis methods of synthesized whitlockite.....	55
3.3 Design and fabrication of AMCD-HAP.....	59
3.4 Analysis methods of AMCD-HAP structure.....	61
3.5 Biological evaluation of whitlockite and AMCD-HAP.....	65

Part I. Compositional control at nanoscale for bone implant.....75

Chapter 4. Synthesis of whitlockite nanoparticles in physiologically relevant condition of ternary Ca(OH)₂-Mg(OH)₂-H₃PO₄ system75

4.1 Introduction.....	75
4.2 Synthesis of whitlockite nanoparticles in ternary Ca(OH) ₂ -Mg(OH) ₂ -H ₃ PO ₄ system.....	77
4.3 Characterization of whitlockite nanoparticle.....	86
4.4 Distinction between whitlockite and β-tricalcium phosphate..	88
4.5 Stability of whitlockite.....	91
4.6 Summary.....	94

**Chapter 5. Phase transformation from hydroxyapatite to whitlockite: interplay of two major biominerals in bone. ...
.....95**

5.1 Introduction.....	95
5.2 Formation of whitlockite from serial transition of pH in Ca(OH) ₂ -Mg(OH) ₂ -H ₃ PO ₄ aqueous system.....	96
5.3 Kinetic path of the whitlockite in the ternary Ca(OH) ₂ -Mg(OH) ₂ -H ₃ PO ₄ system.....	99
5.4 Summary.....	113

Chapter 6. Biocompatibility evaluation of whitlockite as a cell scaffold 115

6.1 Introduction	115
6.2 Whitlockite observation in human tooth.....	117
6.3 Cell proliferation level on whitlockite scaffold.....	119
6.4 Cellular activity level on whitlockite scaffold	121
6.5 Cellular resorption on whitlockite scaffold.....	123
6.6 Summary	126
Chapter 7. Other application studies of whitlockite	128
7.1 Introduction	128
7.2 Fabrication of whitlockite into various types of bone implant according to its mechanical property.....	129
7.3 Whitlockite for toothpaste application.....	132
7.4 Utilization of hydrogen peroxide catalyst for rapid production of whitlockite	135
7.5 Summary	138
Part II. Structural control at nanoscale for bone implant	140
Chapter 8. Making bone implant ‘alive’ with built-in self-powered capillary supply of nutrients.....	140
8.1 Introduction	140
8.2 Bioinspired capillary fluid transport by the change in diameter of the channel	141
8.3 Generation of continuous graded pore structures in bioceramic through the new sintering method with sloped pressurization.....	152
8.4 Capillary rise in arborized channels of a bioceramic.....	170
8.5 Nutrient supply for the living organisms by AMCD	177
8.6 Summary	182
Chapter 9. Concluding remarks	183
9.1 Summary	183
9.2 Further suggested research ideas	186

List of Tables

Table 2.1 Concentration of main components in human tooth	19
Table 2.2 Concentration range of main constituents in bone mineral ..	27
Table 2.3 Various calcium phosphates with their molar ratios of Ca/P, mineral names and chemical formulae.....	33
Table 3.1 Synthesis condition for whitlockite in Ca(OH) ₂ -Mg(OH) ₂ -H ₃ PO ₄ aqueous system.....	54
Table 3.2 List of primers used for real time PCR	68
Table 3.3 List of 1 st antibodies used for western blot.....	71
Table 5.1 Stages I~VI classified by pH, amount of H ₃ PO ₄ and experiment time during formation of whitlockite in Ca(OH) ₂ -Mg(OH) ₂ -H ₃ PO ₄ aqueous system.....	98

List of Figures

Figure 1.1 Occurrence of whitlockite in hard tissue of human body.....	5
Figure 1.2 Basal metabolic rates for living organisms respect to their masses on a logarithmic scale, which accord to three-quarter power scaling law.	7
Figure 1.3 Various structural types of supply networks.....	8
Figure 1.4 Spontaneous movement of water droplet, which prey are suspended in, by tapered structure of beak of shorebird.....	9
Figure 1.5 Tapered nanochannels inside the natural hard tissues.....	11
Figure 2.1 Dental enamel composed of different levels of hierarchical structures from nanometer to micrometer scales based on calcium phosphate crystallites.	22
Figure 2.2 The seven hierarchical levels of bone structure.....	31
Figure 2.3 Stability curves of calcium phosphate compounds in $\text{Ca}(\text{OH})_2\text{-H}_3\text{PO}_4$ aqueous system at 37 °C, based on the solubility.....	35
Figure 2.4 Scheme of kinetic pathways of calcium phosphates at various pH conditions.	39
Figure 2.5 Previously predicted probable location of whitlockite, under physiologically relevant condition of $\text{Ca}(\text{OH})_2\text{-Mg}(\text{OH})_2\text{-H}_3\text{PO}_4$ aqueous system.....	44
Figure 2.6 Current methods to fabricate porous bioceramics in micrometer scale.....	46
Figure 2.7 Fabrication mechanism of freeze casting method and similar natural structure.....	50
Figure 4.1 Ternary diagram of well-known precipitants in a $\text{Ca}(\text{OH})_2\text{-Mg}(\text{OH})_2\text{-H}_3\text{PO}_4$ aqueous system at 80 °C.	78
Figure 4.2 Crystal structure of whitlockite compare to tricalcium phosphate and magnesium-substituted tricalcium phosphate.....	79
Figure 4.3 Synthetic conditions of pure whitlockite from $\text{Ca}(\text{OH})_2\text{-Mg}(\text{OH})_2\text{-H}_3\text{PO}_4$ system, which are plotted as blue cross symbols, with the x-axis being the ratio of the anion (P) to cations (Ca+Mg) in mole% and the y-axis being the content of Mg in the total cation (Ca+Mg), also in mole%.....	82
Figure 4.4 Ternary diagram of precipitants in a $\text{Ca}(\text{OH})_2\text{-Mg}(\text{OH})_2\text{-H}_3\text{PO}_4$ aqueous system after 24 hours of aging at 80 °C..	84

Figure 4.5 XRD analysis of precipitants formed in the binary system of dicalcium phosphate anhydrous (DCPA: CaHPO_4) and dimagnesium phosphate (MP: MgHPO_4), with different Mg contents in total cation (Ca+Mg).....	85
Figure 4.6 XRD patterns showing the pure phase of the synthesized whitlockite.....	86
Figure 4.7 Homogeneously synthesized whitlockite nanoparticles.....	87
Figure 4.8 Distinction of whitlockite from tricalcium phosphate compounds based on HPO_4^{2-} group in its chemical structure.....	89
Figure 4.9 Stability test of whitlockite.....	92
Figure 4.10 Solubility test of whitlockite and hydroxyapatite in the acidic pH region.....	93
Figure 5.1 Serial pH transition from basic to acidic during formation of whitlockite in $\text{Ca}(\text{OH})_2\text{-Mg}(\text{OH})_2\text{-H}_3\text{PO}_4$ system.....	97
Figure 5.2 pH transition during whitlockite precipitation in $\text{Ca}(\text{OH})_2\text{-Mg}(\text{OH})_2\text{-H}_3\text{PO}_4$ system at 70 °C and 80 °C.....	97
Figure 5.3 XRD analysis of the intermediate phases of whitlockite during addition of H_3PO_4 in the $\text{Ca}(\text{OH})_2\text{-Mg}(\text{OH})_2$ aqueous system at 70 °C.....	100
Figure 5.4 XRD analysis of the intermediate phases of whitlockite during aging process in the $\text{Ca}(\text{OH})_2\text{-Mg}(\text{OH})_2\text{-H}_3\text{PO}_4$ system at 70 °C.....	101
Figure 5.5 XRD analysis of the intermediate phases of whitlockite during addition of H_3PO_4 in the $\text{Ca}(\text{OH})_2\text{-Mg}(\text{OH})_2$ aqueous system at 80 °C.....	102
Figure 5.6 XRD analysis of the intermediate phases of whitlockite during aging process in the $\text{Ca}(\text{OH})_2\text{-Mg}(\text{OH})_2\text{-H}_3\text{PO}_4$ system at 80 °C.....	103
Figure 5.7 Kinetic path of whitlockite at 70 °C in $\text{Ca}(\text{OH})_2\text{-Mg}(\text{OH})_2\text{-H}_3\text{PO}_4$ aqueous system.....	104
Figure 5.8 Morphologies of the intermediate phases of whitlockite (WH) during precipitation in $\text{Ca}(\text{OH})_2\text{-Mg}(\text{OH})_2\text{-H}_3\text{PO}_4$ system.....	106
Figure 5.9 Change of the amount of the Ca^{2+} and Mg^{2+} in the precipitant and filtrate during the precipitation process of whitlockite.....	110
Figure 5.10 Kinetic path of precipitation of whitlockite in $\text{Ca}(\text{OH})_2\text{-Mg}(\text{OH})_2\text{-H}_3\text{PO}_4$ system depending on different temperature condition.....	112

Figure 5.11 Partial transition of hydroxyapatite into whitlockite after aging with excessive Mg^{2+} and H_3PO_4 at 90 °C for 3 days	113
Figure 6.1 Direct observation of whitlockite in human tooth	118
Figure 6.2 MTT cell proliferation test of human osteoblast cells grown on the surface of hydroxyapatite, tricalcium phosphate and whitlockite in cylindrical pellet form.	120
Figure 6.3 Direct observation of cells grown on the surface of scaffold made by hydroxyapatite, tricalcium phosphate and whitlockite.	121
Figure 6.4 Relative gene expression evaluated by quantitative real time PCR indicated that osteoblasts grown on whitlockite expressed equivalent level of bone formation associated genes compared to the cells grown on hydroxyapatite.....	122
Figure 6.5 Western blot images of proteins extracted from osteoblasts grown on hydroxyapatite and whitlockite scaffolds.	123
Figure 6.6 Mature states of multinucleated osteoclasts grown on the bottom of the well plate, next to whitlockite pellet.	124
Figure 6.7 Lacunae formation on the surface of hydroxyapatite, whitlockite and tricalcium phosphate pellets by osteoclast resorption activity.	125
Figure 7.1 Vickers Hardness values of whitlockite, hydroxyapatite and tricalcium phosphate depending on different sintering temperatures... ..	130
Figure 7.2 Images of porous implants with size of approximately 1 mm with pore dimension of about 330 μm	131
Figure 7.3 Images of cylindrical implant with both diameter and length were designed to be approximately 4 mm.	132
Figure 7.4 Fluoride uptake level (%) of hydroxyapatite, whitlockite, magnesium-substituted tricalcium phosphate and tricalcium phosphate after 24 hours of reaction with NaF in aqueous solution at room temperature.....	134
Figure 7.5 Rapid production of whitlockite in $Ca(OH)_2$ - $Mg(OH)_2$ - H_3PO_4 system at 80 °C, with different amount of H_2O_2 addition.	137
Figure 7.6 Image of rapidly precipitated whitlockite supported by green catalyst.	138
Figure 8.1 Bio-inspired capillary fluid transport in diameter-tapered channels.	142

Figure 8.2 Capillary rise height depending on the level of gradient angle of the tube.....	145
Figure 8.3 Simplified Laminar fluid with radius of s and thickness of the fluid as ds	147
Figure 8.4 Conical tube and cylindrical tube with different geometry while their radii are same as a at height L	148
Figure 8.5 Flux in the conical tube	149
Figure 8.6 Phase segregation of polyethylene glycol polymer and hydroxyapatite during pressurized sintering process, depicting formation of an interconnected pore structure.....	154
Figure 8.7 Phase diagram of AMCD-HAP components.	155
Figure 8.8 Generation of networked and graded capillary structures in bio-ceramic material through the application of unidirectional gradient of pressure during sintering.	156
Figure 8.9 N_2 adsorption-desorption isotherm confirmed augmentation of porosity generated by the applied pressure.	158
Figure 8.10 Schematic representation of AMCD-HAP with four different porosity sections shown.	159
Figure 8.11 Mechanical strength of AMCD-HAP	160
Figure 8.12 FESEM images of pores from the H (highest pressure) section, where pore diameters were approximately in the micrometer range.....	161
Figure 8.13 Reconstruction of nanochannels inside the scaffold.	162
Figure 8.14 Reconstruction of nanochannel by Nano-CT.....	164
Figure 8.15 Internal structure of the AMCD-HAP pellet	164
Figure 8.16 Electron microscopic characterization of AMCD-HAP.....	166
Figure 8.17 EELS mapping images of LL section from Figure 8.13a....	167
Figure 8.18 EELS mapping images of pores with nanometer dimension from Figure 8.15a.....	168
Figure 8.19 Tapered nanochannel in whitlockite made by controlling the sintering temperature at $900\text{ }^\circ\text{C}$	169
Figure 8.20 Tapered nanochannel in whitlockite made from controlling the ratio of the poly ethylene glycol to whitlockite as 1:2.	170
Figure 8.21 <i>in situ</i> FDG-PET imaging showed that the AMCD-HAP sample exhibited a greater capillary force than a control nonporous HAP sample.....	172
Figure 8.22 Computed tomography (CT) scanning of the inner	

hierarchy structure of the bone implant material.....	173
Figure 8.23 Capillary rise of AMCD-HAP.....	175
Figure 8.24 Porosity of the PEG-HAP pellet depending on the molecular weight of PEG and applied pressure level during sintering process.....	176
Figure 8.25 Human osteoblast cells grown on AMCD-HAP ceramic material.....	179
Figure 8.26 Relative gene expression measured by quantitative real time PCR revealed that osteoblasts grown on top of AMCD-HAP samples expressed similar levels of bone-related genes compared to the expression profile for osteoblasts grown on fully immersed HAP samples.....	180
Figure 8.27 Bacterial growth atop the AMCD-HAP pellets.....	181

Chapter 1. Introduction

1.1 Introduction of biomineral and calcium phosphate compound

Biominerals can be defined as inorganic compounds which are formed by direct or indirect interaction of living organism¹. Most of their roles are vital for the maintenance of the life and thus understanding the science of biominerals can eventually lead to the brightening the origins and the mechanism of life. In fact, based on the substantial progress of comprehending biominerals, innovative applications in biology, chemistry, material science and medical engineering have been achieved. The most representative example would be implant related biomineral researches, which provided better treatments of bone replacement or coating of bone prostheses to numerous bone disease related patients.

Among various biominerals, calcium phosphate compounds have been received considerable attention from scientists, because most of the inorganic parts in our hard tissue are composed of calcium and phosphate¹⁻⁵. The major phase and the second most abundant phase of our tooth and bone are hydroxyapatite (HAP: $\text{Ca}_{10}(\text{PO}_4)_6(\text{OH})_2$) and whitlockite (WH: $\text{Ca}_{18}\text{Mg}_2(\text{HPO}_4)_2(\text{PO}_4)_{12}$), respectively¹. Study of calcium phosphate compound *in vivo* is complex due to the simultaneous intervention of various ions, organics, proteins, hormones and cells in our body. Therefore, the investigation of calcium phosphate phase in individually simplified system can provide foundations to understanding the complicated interactions of biomineral with our dynamic body system. Until now, significant

development has been achieved in revealing chemistry and characterization of HAP by previous researchers while there are still many unknown problems for WH to be solved. In this regard, here, we devoted to provide an integrated knowledge of WH based on the new finding of synthesis technique of pure WH nanoparticles. We also expect that our scientific methodology for determining the synthesis condition of WH can provide a new platform for searching other important precipitants in physiological systems.

Along with the chemical properties, another important aspect of biominerals is their unique structures that will induce effective circulation for the vital activity. Well organized self-assembled structure, hierarchical structure, fractal structure and spiral structure in nature have been inspired to many engineers with their advantages of spontaneous organization, efficient circulation, enhancement of mechanical property and attainment of thermodynamically stable state. For instance, HAP nanoparticles in our osseous tissue are self-assembled in hierarchical structure^{3,6-8}. At the same time, tree-like channels which supply nutrients and fluids also exist inside of these self-assembled hard tissues, with different levels of scales from micrometer to nanometer^{9,10}. In this respect, the structural issue with calcium phosphate compound is also discussed in this study. Especially, having been inspired from the real bone structure, we designed and built aligned multiple channels with decreasing its diameter (AMCD) in bioceramic scaffold with novel pressurized sintering technique based on the organic-inorganic phase separation mechanism. From our approach, we tried to mimic and prove that bioceramic composite is 'alive' in our body system by dynamic circulation.

Biomaterial, particularly calcium phosphate compound, function as

important foundation role to maintain most of living organism. We believe that our new findings in this study will contribute into deeper understanding of body system, improve applications of biomaterials and stimulate further biomineral related research.

1.2 Revisiting whitlockite: its occurrence and importance

Whitlockite (WH: $\text{Ca}_{18}\text{Mg}_2(\text{HPO}_4)_2(\text{PO}_4)_{12}$) exist in various places such as terrestrial mineral near volcanic region¹¹⁻¹³, sedimentary rocks, meteorite and igneous rocks from the extraterrestrial space¹⁴ but also, even in the hard tissues of living organism^{1,2,15-18}. Interestingly, the ratio of WH is known to be higher in younger aged creatures¹⁹ and during the earlier stages of mineralization in the body system²⁰. Distribution feature of WH implies that this material is intimately related to the origins and the evolutions of minerals and planetary bodies. However, the genesis of WH is still in very controversial debate and most of its fundamental effects or significance of existence remains unsolved problems.

The terrestrial existence of WH was firstly reported in 1941 by Frondel in granite pegmatites from the Palermo pegmatite quarry, North Groton, New Hampshire^{11,12}. XRD pattern of analyzed material showed distinct difference with hydroxyapatite (HAP: $\text{Ca}_{10}(\text{PO}_4)_6(\text{OH})_2$) while similar patterns to tricalcium phosphate (TCP: $\text{Ca}_3(\text{PO}_4)_2$). WH was also found in mantle xenoliths from Siberia and suggested that it can be the major host of trace elements or rare earth elements in the upper mantle¹³. Moreover, WH is

the most common phosphate compound in lunar and Martian rocks as well as meteorite from the outer space, which shows even more higher ratio than HAP^{14,21-24}. Furthermore, notably, WH is estimated as the second most abundant bioceramic in our body system, based on the amount of magnesium¹. The majority of our hard tissue is composed of HAP which is one of the most thermodynamically stable calcium phosphate compounds near neutral pH region²⁵. However, it is also known that HAP structure almost cannot incorporate Mg²⁺ in its structure^{1,26}. In this premise, the amounts of WH in human dentin and bone are estimated as 26 to 58 wt% and approximately 20 wt%, respectively¹. WH in our body system can be directly observed by HRTEM rather than XRD, as it usually exists in short-ranged order¹.

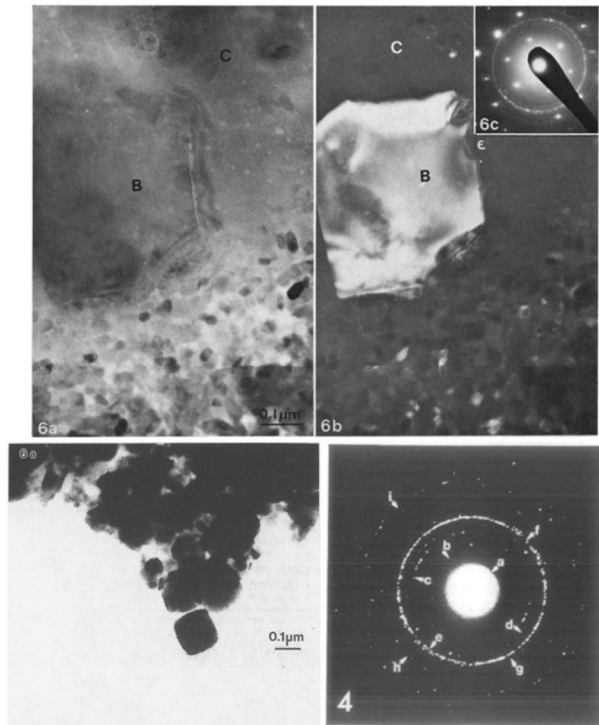


Figure 1.1 Occurrence of whitlockite (WH) in hard tissue of human body.

Top: Bright field and dark field analyses of unerupted human tooth showed a distinction of crystal B with surrounding amorphous C. Top inset: The selected area diffraction pattern analysis of B confirmed the area as a WH¹⁸.

Bottom left: TEM image of nanocrystal isolated from human articular cartilage showed rhombohedral morphology which corresponded to WH¹⁶.

Bottom right: D-spacing value of the mineral obtained from the surface of the intact enamel matched with that of WH¹⁷.

However, despite of the significant occurrence in minerals and large ratio of existence in our body, research related to WH has not been fully

developed due to the difficulty of the synthesis of pure WH nanoparticles in mass scale without any effect of buffer or other additives. As a result, the mechanism of WH formation, significance of existence of WH and interaction of WH with our whole body system are still in unknown state. In contrast, there are numerous reports to synthesize other calcium phosphate compounds. For example, pure phase of HAP nanoparticles can be easily synthesized in aqueous system without involving secondary ions^{1,2,27,28}. Based on the advantage of synthetic simplicity, HAP has been actively investigated with its fundamental science and it is already utilized into various applications. For instance, HAP has been used in medical implant, tooth paste, cosmetics and deodorants²⁹⁻³⁴. Furthermore, TCP, the synthetic analogue of WH, has been also widely utilized in similar industrial fields based on its biocompatibility and convenience of production even though it does not exist in our body^{29,35,36}.

Therefore, in this research, we designed and presented synthesis method of pure WH nanoparticles in physiological condition of ternary Ca(OH)_2 - Mg(OH)_2 - H_3PO_4 aqueous system with clear characterization of its material property, biocompatibility, and other notable qualities to reveal its basic science along with the kinetic mechanism of formation and to apply in various fields.

1.3 Designing living scaffold: considering efficient supply

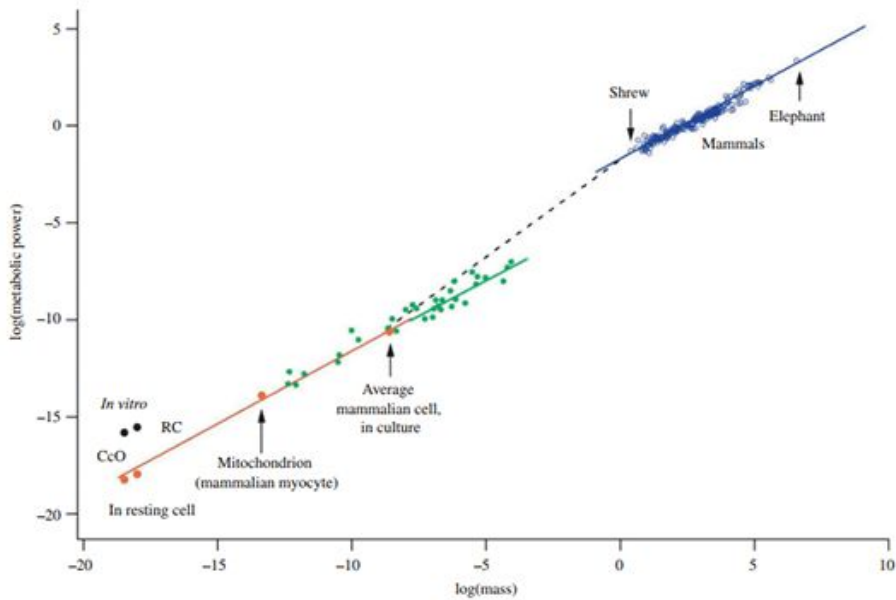


Figure 1.2 Basal metabolic rates for living organisms respect to their masses on a logarithmic scale, which accord to three-quarter power scaling law³⁷.

Nature designs living organisms with efficient hierarchical systems and surface energy gradients for conduction, distribution, and supply of fluids. Well-known examples include tree and blood circulations. Allometric scaling laws in biology found that basal metabolic rate is proportional to mass scale by 3/4 power law^{38,39}. From an isolated small cell to a large elephant, metabolic rate increases as shown in Figure 1.2³⁷. This can be attributed in part to efficient circulatory network support⁴⁰. As the size of the body increases, the circulation system becomes more complex and hierarchical, consisting of global transport in bigger main channels and local

distribution by smaller branched channels. The result is an optimal efficiency by shortest distance to the source *via* a maximal network, as represented in Figure 1.3⁴⁰.

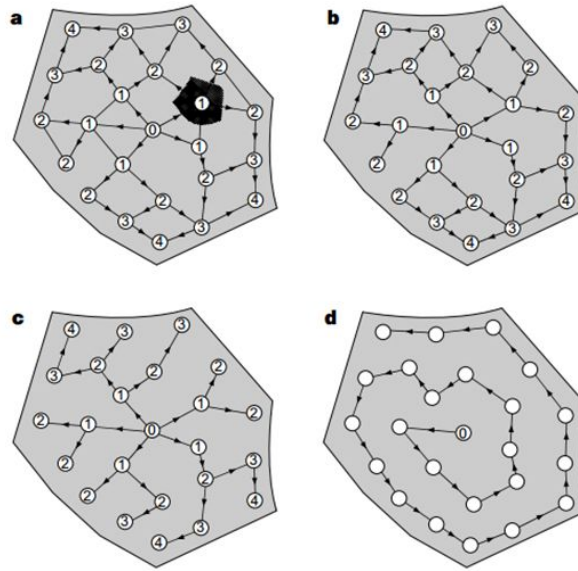


Figure 1.3 Various structural types of supply networks⁴⁰. The node number shows minimum number of sites passed through from, the source (0) to the final site. **a**, Fully connected network in which every node is linked to each other. **b**, Maximal directed network, where total volume of the fluid should be abundant to maintain its connection. **c**, Tree-like network. Each site is efficiently linked to the origin by the shortest single path that the smallest fluid volume is required to maintain the transportation system. **d**, A helical pattern.

In trees, whose height exceeding more than a hundred meters, the networked channel diameters decrease into nanometer range to maximize capillarity, as the capillary force is inversely proportional to channel diameter ($h = \frac{2\gamma \cos \theta}{\rho g r}$). Therefore, channels are larger where more fluid flow is needed, and become thin and tapered where strong capillarity is needed. Another example is, as shown in Figure 1.4, the beaks of shorebirds move water droplets spontaneously toward a specific direction by altering the contact angle⁴¹. Similarly, spider silk collects water droplets from humid air by gradual change in surface energy and difference in the Laplace pressure between joint and spindle-knot sites⁴². The difference of Laplace pressure between these sites moves collected water droplets toward high surface energy with low-contact angle areas in the spindle-knot sites, providing directional accumulation of water.

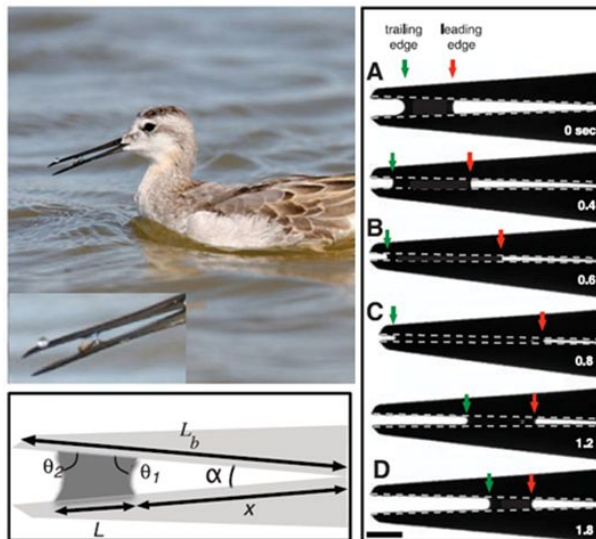


Figure 1.4 Spontaneous movement of water droplet, which prey are

suspended in, by tapered structure of beak of shorebird (left upper inset).

From the difference between the contact angles of both ends of droplet, water droplet transports toward the mouth of shorebirds (left bottom). This phenomenon can be reproduced by mechanical beak with identical principle (right)⁴¹.

In fact, interconnected channel network not only exist in soft tissues such as xylems of tree or vascular networks^{43,44}, but also in hard tissues. For example, there are small channels inside bone^{9,10}, egg shell⁴⁵, crustacean tergite⁴⁶ and nail⁴⁷ as shown in Figure 1.5. Through these channels, gases or fluids are exchanged by linking all the parts to maintain constant range of pressure and/or to supply fluid and nutrients. Specifically, the pores in bones exhibit a gradual decrease in their diameters from the interior to the outer surface with hierarchically arranged capillaries spreading from a central blood vessel to peripheral tissues^{9,10}. The circulatory system moves blood cells and plasma by muscle contraction controlled by the pericytes in very thin arborized capillary beds, complemented by capillary transport and distribution to peripheral sites.

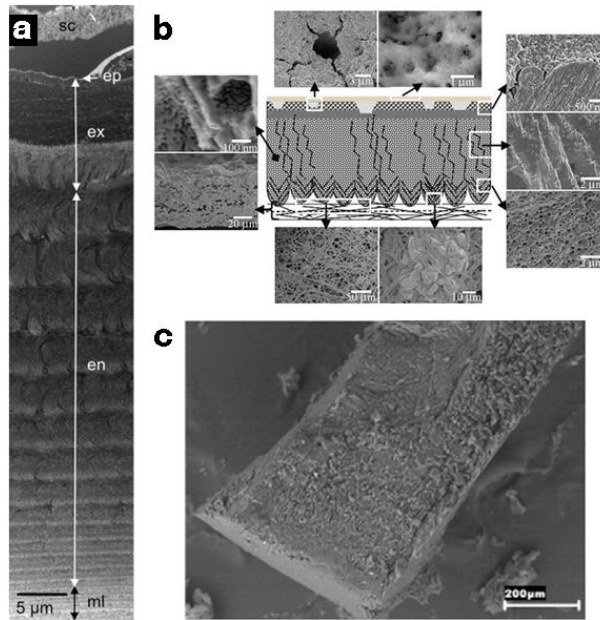


Figure 1.5 Tapered nanochannels inside the natural hard tissues. **a**, Tergite cuticle of *Tylos europaeus* shows tapered nanochannels from its exterior to interior structure (sc: surface coat, ep:epicutile, ex: exocuticle, en: endocuticle, ml: membranous layer)⁴⁶. **b**, Eggshell also shows hierarchical pore structure from nanometer to micrometer scales⁴⁵. **c**, Cross-section view of human nail tip also shows high porosity at the surface and low porosity at the internal structure⁴⁷.

For many applications, including the ones we are pursuing, the capillary drawing power alone may not suffice. The overall permeability matters, just as much. To achieve both, one would need, and indeed the proposed effort seeks, to devise a volume-production strategy to engineer high volume-densities of networked and tapered capillaries into ceramic composites. In this thesis, we developed a ‘living composite’ that could

enable biomedical applications such as bone implants and skeletal repairs. The presented ‘living composite’ operates on the basis of self-powered, pore-gradient driven micrometer and nanometer capillary networks that can achieve unidirectional supply of nutrients within a load-bearing composite.

1.4 Objective of the thesis

Priority aim of this thesis was to describe new findings of synthesis technique of pure whitlockite (WH: $\text{Ca}_{18}\text{Mg}_2(\text{HPO}_4)_2(\text{PO}_4)_{12}$) nanoparticles and fabrication method of aligned multiple channels with decreasing its diameter (AMCD) in HAP scaffold (AMCD-HAP). Along with this direct outcome reporting, another intended objective in this thesis was to show systematic approach of designing and presenting new concept of materials and to provide useful platforms for other researchers.

In the first half of thesis, we introduced WH as a new bioceramic for the bone implant or as a new biological scaffold for the cell growth. Although WH is the second most abundant bioceramic in bone, the importance of its biological role and its consequent applications have never been emphasized at the necessary level. In contrast, hydroxyapatite (HAP: $\text{Ca}_{10}(\text{PO}_4)_6(\text{OH})_2$), the major component of bone, has been actively investigated and tricalcium phosphate (TCP: $\text{Ca}_3(\text{PO}_4)_2$), synthetic analogue of WH, has been widely used as a commercial implant material. We thought that the major reason for this lack of emphasis was due to the difficulty of synthesizing pure WH in aqueous solution without using any additives or buffers. The identification of synthetic conditions under a physiologically similar environment is a key challenge to be addressed. However, the

synthesis of WH was difficult because its theoretical composition is within the range that usually produces nonstoichiometric HAP, which means that HAP is the majority product formed when the theoretical ratio of WH (Ca:Mg:P = 18:2:14 (mole%)) is mixed in a ternary Ca(OH)₂-Mg(OH)₂-H₃PO₄ system. In this regard, our aim was to clearly show the facile, scalable process to make nano-sized WH in physiologically relevant condition and reveal the precipitation mechanism that may provide a new insight to understand its biological formation in bone.

This new finding became possible from the inspiration of synthetic analog TCP, which becomes stabilized in the acidic after the incorporation of Mg²⁺ in its chemical structure. Another rationale to design the experiment, we focused on the HPO₄²⁻ group in the chemical structure of WH and analyzed binary CaHPO₄-MgHPO₄ system. With slow increase of H₃PO₄ ions that can kinetically tune the transformation of HAP/other calcium phosphate compounds to WH and controlling accurate ratio between Ca²⁺, Mg²⁺ and HPO₄²⁻, we have successfully synthesized the pure phase of WH in nanoparticles. To clearly characterize the properties of WH, several profound analysis techniques including XRD, FESEM, HRTEM, FT-IR, TGA, ICP and ion chromatography were conducted relative to well-known commercially utilized references, HAP and TCP. We also tried to evaluate basic biocompatibility level of pure WH compare to HAP and TCP, *in vitro*, by cellular proliferation tests and activity tests such as MTT test, staining method, real time PCR and western blot. To our surprise, nano-WH exhibited similar or even better biocompatibility to the growth of human bone cells than HAP. In addition, we tried to investigate stability of WH compare to HAP and found that WH was not only favored to precipitate in

acidic conditions but was also more stable than HAP when the pH was below 4.2.

From all these positive outcomes, the systematic approach to determine the synthesis conditions of WH was expected to provide a new platform for discovering other important chemical compounds in aqueous systems. In this respect, our object of this thesis was also to deliver our new findings and knowledge to other researchers so that profound understanding of the chemical mechanism of bone formation and active application in various fields can be induced.

Another purpose in the latter half of this thesis was to mimic the hierarchical channels ubiquitous in many biological systems, including natural bone structure, and we have successfully fabricated a long-ranged-, nano-capillary network within a bulk ceramic biocompatible material. While fabricating nanopores or nanochannels inside of a ceramic material has been remained a challenge in this field, previously reported nanopores or nanochannels incorporated inside ceramic materials were disconnected or continuous changes of diameters were limited. Based on the advantages of gradually changing diameters in aligned nanochannels, our objective was to incorporate a network of interconnected, aligned nanochannels with gradually decreasing diameter in scaffold made of calcium phosphate inorganic compound. We also aimed to show that fluid and small substances can be transported continuously and spontaneously through the solid ceramic that is also capable of load bearing and is, in fact, stronger than bone. Moreover, it enabled and sustained cell growth and differentiation, effectively making the man-made structure close to being “active and alive”. We tried our best knowledge to describe in detail of the methodology we

employed for the formation of the nano-capillary network by phase segregation in pressurized sintering, as well as the counter-intuitive finding of the inverse relation between the applied pressure and the capillary diameter, with desirous to be utility to other investigators in allied fields of research.

1.5 Organization of the thesis

This thesis consists of two parts with nine chapters. To begin with, in order to introduce basic scientific information of biominerals and calcium phosphate compounds which would be supportive to understand our experimental outcomes, a brief description of each important concept is given; In Chapter 2, the distribution of biomineral in living organism, general chemistry and structure of important calcium phosphate compounds related to biomineral including WH and current methods to produce porous scaffold from calcium phosphate compound are explained. In Chapter 3, experimental procedures are described, including methods for synthesis of pure WH nanoparticles and fabrication of AMCD-HAP with their characterization and biocompatibility evaluation.

In part I, synthesis of WH nanoparticles with its characterization analysis and biocompatibility evaluation is discussed; In Chapter 4, large-scale synthesis of pure WH in ternary $\text{Ca}(\text{OH})_2\text{-Mg}(\text{OH})_2\text{-H}_3\text{PO}_4$ system is introduced with confirmation of its phase. In Chapter 5, kinetic path of the formation of WH in $\text{Ca}(\text{OH})_2\text{-Mg}(\text{OH})_2\text{-H}_3\text{PO}_4$ aqueous system is dealt, depending on the pH of the system. In Chapter 6, biocompatibility of WH is

shown with cellular level of proliferation and their bone related activities compared to that of previous known biomaterials such as HAP and TCP. Chapter 7 describes other remarks on notable properties and potential applications of WH for further advanced research.

In Part II, we discuss about new concept of designing a ‘living’ bone implant with built-in self-powered capillary supply of fluids and nutrients. In Chapter 8, we explain how to fabricate dimension tunable nanochannels in bioceramic depending on phase separation mechanism and show enhancement of supply power. Especially we showed that small living organisms can proliferate solely depending on the supply power of the nanochannel.

Finally, in Chapter 9, there is concluding remarks with overall summary and further suggested research ideas.

Chapter 2. Theoretical background of composition and structure of biominerals

2.1 The mineral in tooth and bone

Hard tissues, including tooth and bone are important part of body for maintaining life. Most of vertebrates use teeth to eat food in small pieces and some use teeth for defensive purposes or hunting. Bone supports our body and at the same time, protects organs inside our body. Additionally, bone produces various blood cells and act as a central storehouse for minerals in our body. Significance of hard tissue in living system cannot be emphasized anymore.

Generally, most of tooth and bone have heterogeneous structures consisting of well-organized small mineral particles with organic materials such as collagen and other proteins. Like the mortar between the bricks, gel-like aqueous organic matter and inorganic nano materials are regularly assembled in hierarchical structure which leads to the maximized mechanical property⁴⁸⁻⁵⁰. There are also living cells, ameloblasts, odontoblasts or osteoblasts, which mainly act in producing new minerals and continuously remodel the old and weak part of hard tissue to a healthy new state. The rest components are mostly water. In this chapter, we will describe general chemistry, structure and physical properties of biomineral in natural human tooth and bone which can be useful for understanding our present research.

2.1.1 The mineral in enamel and dentin of human tooth

Mineralization in tooth begins with the secretion of ameloblasts and odontoblasts. During amelogenesis, ameloblasts produce amelogenine, tuft protein and other various proteins for the formation of enamel^{51,52}. Odontoblasts synthesize a predentin in the form of so-called matrix vesicles which mineralize earlier than enamel matrix⁵³. These matrix vesicles act as loci of initial calcification, while matrix vesicles are in intact state, where minerals are in amorphous phase^{54,55}. After plasma membrane of matrix vesicle break, the mineral particles crystallize and rapidly grow. Then, maturation of enamel occurs by loss of some water and protein which are replaced into mineral. During the secondary mineralization, crystallites in tooth grow thicker than initial state⁵⁶. In dentin, simultaneous grow of crystallites makes overall particle morphology into spheroidal and these spheroids later become seams of the intertubular dentin⁵³.

The general constituents of enamel and dentin in human tooth are mineral, organic matter and water. Mineral comprise 93.6~98.5% and 66~88% of enamel and dentin, respectively¹. Organic materials in human tooth enamel and dentin are known to be proteins, mucopolysaccharides, lipids and citrates¹. The major and minor inorganic constituents of human enamel and dentin are shown in below Table 2.1¹.

Constituent	Enamel		Dentin	
	Concentration	Average	Concentration	Average
	range (wt%)	concentration (wt%)	range (wt%)	concentration (wt%)
Ca	34.6~38.2	36.6	24.7~31.5	26.9
P	16.3~19.2	17.7	12.3~14.0	13.2
CO ₃	2.4~4.2	3.2	4~5	4.6
Na	0.17~1.16	0.67	0.2~0.8	0.6
Mg	0.04~0.68	0.35	0.6~1.33	0.8
Cl	0.16~0.7	0.35	0.04~0.4	0.06
K	0.018~0.1	0.04	0.01~0.04	0.02

Table 2.1 Concentration of main components in human tooth
(dry weight %)¹

Besides these main elements, there are also various trace elements detected in enamel part of the human tooth, such as Zn (9~1200 µg/g), Sr (13~1400 µg/g), Si (3~1400 µg/g), F (8~1000 µg/g), S (0~530 µg/g), Al (1.5~353 µg/g), Fe (0.8~759 µg/g), Pb (<0.1~1000 µg/g), Ba (0.8~190 µg/g), B (0.5~190 µg/g), Br (0.32~33 µg/g), Cd (0.03~74 µg/g), I (0.01~9.9 µg/g), Rb (0.15~30 µg/g), Cu (0.1~81 µg/g), Ag (0.005~37 µg/g), Mo (0.6~39 µg/g), Ti (<0.1~66 µg/g), Cr (0.003~18 µg/g), Sn (0.03~93 µg/g), Be (<0.01~15.9 µg/g), Ni (0.1~13 µg/g), Se (0.012~18 µg/g), Li (0.05~13.2 µg/g), Co (0.0002~45 µg/g), Mn (0.08~63 µg/g), Zr (<0.02~12 µg/g), W (<0.08~0.40 µg/g), Nb (<0.1~0.76 µg/g), Sb (<0.001~3.0 µg/g), Ce (0.02~0.19 µg/g), Au (<0.02~0.30 µg/g), Nd (<0.02~0.09 µg/g), Cs

(<0.02~0.10 $\mu\text{g/g}$), Pr (<0.01~0.07 $\mu\text{g/g}$), V (<0.01~0.28 $\mu\text{g/g}$), Y (<0.01~0.17 $\mu\text{g/g}$), As (<0.001~0.008 $\mu\text{g/g}$), Hg (0.005~16 $\mu\text{g/g}$) and Bi (<0.02~0.07 $\mu\text{g/g}$)¹. These elements are arranged in descending manner and their units are shown in concentration range. For the dentin part of the human tooth, trace elements such as B, F (2~1000 $\mu\text{g/g}$), Al (65~150 $\mu\text{g/g}$), Si, S (706 $\mu\text{g/g}$), Ti, V, Cr (0.005~2 $\mu\text{g/g}$), Mn (0.04~6 $\mu\text{g/g}$), Fe (2~110 $\mu\text{g/g}$), Co (0.0003~32 $\mu\text{g/g}$), Ni (5~30 $\mu\text{g/g}$), Cu (0.2~50 $\mu\text{g/g}$), Zn (100~700 $\mu\text{g/g}$), As, Se (0.1~0.3 $\mu\text{g/g}$), Br (4~115 $\mu\text{g/g}$), Rb (5.6 ± 1.9 $\mu\text{g/g}$), Sr (70~250 $\mu\text{g/g}$), Mo, Ag (0.005~3 $\mu\text{g/g}$), Sn, Sb (0.69 ± 0.41 $\mu\text{g/g}$), I (3.7 ± 0.4 $\mu\text{g/g}$), Ba (129 ± 55 $\mu\text{g/g}$), W (2.6 ± 1.1 $\mu\text{g/g}$), Au (0.03~0.07 $\mu\text{g/g}$) and Pb (2~44 $\mu\text{g/g}$) are detected¹. However, the amount of constituent varies depending on difference in experimental conditions, individuals and ages. Moreover, it is difficult to measure accurate amount of constituent, because extracting or preparing components in intact state is almost impossible and analyzing itself might give damage to the sample. Original phase can be transformed or remineralize during extracting process. In addition, it is known that element distribution gradually changes from enamel surface to dentino-enamel junction and also to pulp. It is reported that concentrations of Na, CO₃, Mg increase depending on the distance from the enamel surface toward dentino-enamel junction, while concentration of Cl is known to be continuously decreased^{57,58}. However, despite various kinds of trace elements exist in tooth, it is known that most of trace elements are related to proteins with less considerable amount. In this regard, our further discussion will be focused on the major inorganic components of human tooth which are calcium and phosphate.

In 1926, Gross firstly reported that crystallography analysis from X-

ray diffraction showed the major phase of tooth as apatite⁵⁹. On the basis of a hexagonal unit cell, a- and c-axis dimension for human tooth enamel were analyzed to be approximately 0.9448 nm and 0.6888 nm, while that of synthetic HAP were known to be 0.9418 nm and 0.6880 nm^{60,61}. Structure of dentin is less dense than that of enamel and shows 0.9434 nm and 0.6868 nm, respectively, for a- and c- axis on the basis of a hexagonal apatite unit cell⁶². From the observation of electron microscopy, general shape of well-organized crystallites in human enamel is long elongated crystals with high aspect ratio. In addition, using high resolution transmission electron microscopy, hexagonal shape of crystallites in enamel were measured and their width and thickness were reported as 68.3 ± 13.4 nm and 26.3 ± 2.2 nm⁶³, respectively. The total length of the enamel crystallites were reported as up to between 100 and 1000 nm⁶⁴. Dentin is constituted of HAP crystallites with its width of 25.37 ± 1.4 nm, thickness of 9.8 ± 0.7 nm and length of 36.0 ± 1.9 nm in three dimensional scaffold matrix of type I collagen fibrils⁶⁵.

These crystallites in enamel and dentin are three dimensionally well-arranged at different hierarchical levels from micrometer to nanometer scales. Due to the benefits from recently achieved image technologies such as atomic force microscope, scanning electron microscope and transmission electron microscope, many reports clearly showed self-assembled structure of apatite crystallites in enamel, directly³. As shown in Figure 2.1, on the micrometer and nanometer scales, the enamel structure has regularly repeated units known as enamel prisms and nanorods shape of apatite crystallites, respectively. Dentin structure has more direct reflection of its initial formation from the odontoblastic cells that its architecture consist of

dentinal tubules with $\sim 1 \mu\text{m}$ diameter, surrounded by peritubular dentin made of randomly oriented apatite crystallites in cylindrical form with thickness of $0.5\sim 1 \mu\text{m}$ ⁶⁶. Tubular units in dentin are embedded in a hybrid composite of apatite reinforced collagen matrix.

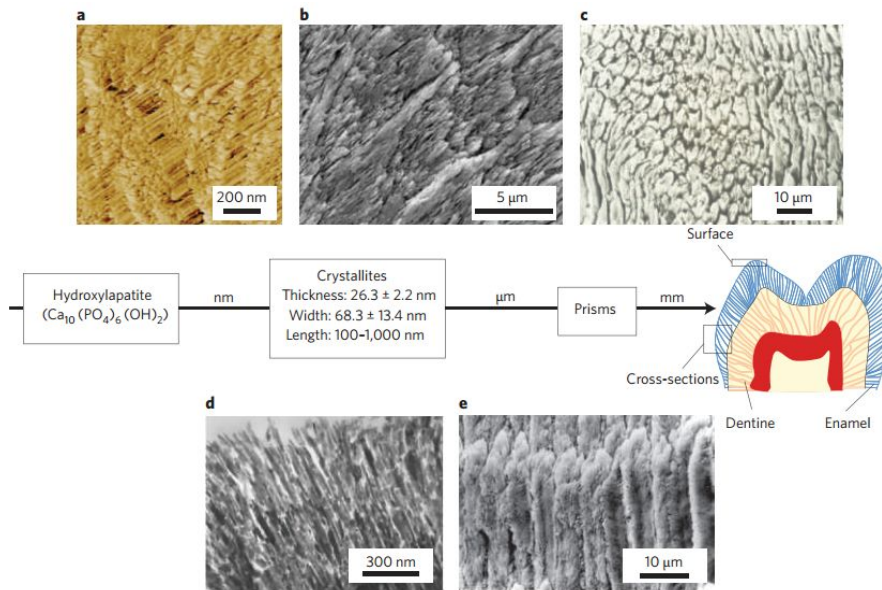


Figure 2.1 Dental enamel composed of different levels of hierarchical structures from nanometer to micrometer scales based on calcium phosphate crystallites³. **a-c**, Surface of enamel was observed by atomic force microscope and FESEM. **d-e**, Cross-sectional images of the enamel were obtained by TEM and FESEM.

Even though the major inorganic component of enamel crystallites has roughly similar X-ray diffraction pattern with HAP, presence of many vacancies and various ions make the natural biomineral in tooth different

from synthetic HAP^{1,67-72}. From the infrared spectroscopic and nuclear magnetic resonance studies, fluoride and chloride ions exist in lattice of tooth from substitution of hydroxyl part of apatite in 1 to 1 exchange and randomly distributed along the c-axis. Similarly, compare to the results from neutron diffraction, laser-Raman spectrometry and electron spin resonance spectrometry of synthetic HAP, that of powdered tooth showed perturbed hydroxyl ions from the presence of chloride, fluoride and also due to the effect of water and carbonate^{1,73-75}. Especially, crystallinity of the outer layer of the tooth, with a depth of 500 μm , increases with age⁷⁶ while permeability decreases^{77,78}, which probably reflects the formation of fluoridated hydroxyapatite near surface¹. Enamel is also reported to have generally excess of hydrogen from the neutron diffraction analysis⁷⁴ which can be reflection of existence of water, proteins and hydrogen involved phosphate group (HPO_4^{2-}). Therefore, major apatite-like phase of inorganic crystallites in tooth are different from synthetic HAP and have various substitutions with following vacancies in order to maintain the balance of total charge.

In addition, abundant amount of magnesium ion is an important evidence of reflecting the existence of other multiphase than apatite, while its contribution and mechanism of formation is still under debate. Magnesium is reported to be associated in inorganic part than organic matter and, notably, it is known that apatite hardly incorporate magnesium in its structure^{1,26}. In this regard, the amount of secondary phase such as WH can be estimated from the amount of the magnesium. However, using conventional tools such as X-ray diffraction, it was hard to detect WH as it existed in short range order in amorphous form. Instead, TEM and FT-IR analysis had been used to confirm the existence of WH in our hard tissue.

The infrared adsorption result of the tooth showed that the absorption peak at 2340 cm^{-1} resembles with the WH⁷⁹. Analysis of the intensity of the peak suggested that the amount of WH in the human enamel can be approximately 20 wt%. Although, the presence of WH in human tooth is certain, the exact amount of WH is still on debate, and additionally, some of magnesium might also be incorporated in other phase than WH, like dolomite ($\text{CaMg}(\text{CO}_3)_2$). From the scanning electron microscopy and electron probe microanalysis, WH crystal was observed in some crevices of tufts and lamellae of caries-free human enamel⁸⁰. However, despite several occurrence of WH in human enamel has been reported, it is known that WH consist more of dentin rather than enamel. In electron microscopic observation, electron diffraction and selected area electron diffraction studies of dentin confirmed the existence of WH in addition to apatite^{1,81}. Based on the premise that the amount of magnesium reflects the ratio of WH phase, the amount of WH is supposed to be 26 to 58% from the concentration range (0.6~1.33 by dry weight %) of magnesium in normal human dentin¹. Initial molar ratio between Mg and Ca is 0.18 in predentin and this ratio (Mg/Ca) gradually decreases during transition to dentin, which indicates that WH is deposited first²⁰. Therefore, along with the apatite-like phase, WH also composes our tooth and contributes in mineralization as a second major phase.

Differences in mechanical property are also shown between enamel and dentin⁸². For example, compressive strength are 95~140 MPa and 230~370 MPa whereas Young's modulus are 9~90 GPa and 11~20 GPa for enamel and dentin, respectively. Tensile strength was measured as 8~35 MPa for enamel and 31~104 MPa for dentin. Shear strength was reported as 90.2 MPa for enamel and 36~138 MPa for dentin. Micro-hardness was known as

3.2~4.4 GPa for enamel and 0.25~0.8 GPa for dentin. Considering all these mechanical factors, tooth enamel seems to be relatively harder and more brittle than dentin. On the contrary, dentin is tougher than enamel. In fact, degree of crystallinity in enamel and dentin are reported as 98% and 68%, respectively, by IR studies¹.

In summary, tooth enamel and dentin contains mineral about 96 wt% and 70 wt%, respectively. Most of mineral phase is generally assumed to comprise apatite-like and WH phase. These inorganic crystallites are self-assembled into three dimensionally hierarchical structures from nanometer to micrometer scales. Still, enamel and dentin has different components, architectures, chemical and physical properties. Especially, dentin consists of higher WH compare to enamel. Our thesis will be helpful in figuring out the role of WH in the human tooth and understanding the effect of WH which might have induced different properties between enamel and dentin.

2.1.2 The mineral in human bone

Similar to tooth, bone is composed of small mineral crystallites in a gel-like organic matter with some water. One of the most distinct differences of bone with hard tooth tissue is its initial mineralization mechanism. Bone formation initiates from the osteoblast cell, which is one of the final differentiated form derived from mesenchymal stem cells and name originated from the Greek words for “bone” and “germinate”. Osteon, the group of osteoblasts, is responsible for producing a matrix of osteoid, collagen and mineralization related proteins such as osteocalcin or

osteopontin. Also, osteoblast become trapped and isolated in the bone matrix or lacunae, which eventually become in the form of osteocyte. This osteocyte ceases to synthesize osteoid and matrix, but instead becomes a part of bone tissue or otherwise undergoes apoptosis. After the secretion activity of osteoblast, bone mineralization is known to start as the bone matrix vesicles break up which then simultaneously induce deposition of minerals^{83,84}.

The main components of compact bone in mammalian are mineral (~70 wt%), organic matter (~24 wt%) and water (~6 wt%)¹. Isolation of the mineral part of bone showed its main components Ca, P, CO₃, Na and Mg and their amounts are shown in Table 2.2¹. Based on this table, molar ratio between Ca and P was reported as 1.61~1.87 wt%. Also, besides these main components, K, Sr, F, Cl and Pb are also known to exist. However, like tooth, measuring amount of component in bone tissue is very complex and reported amount varies depending on the position of bone, individuals, species, ages, diet and from the pathological conditions. The organic part of compact bone is mostly consisted of collagen (~89%), mucopolysaccharides (~8%), sialoprotein and lipids with phosphate^{1,85}.

Component	Range (wt%)
Ca	32.6~39.5
P	13.1~18.0
CO ₃	3.2~13
Na	0.26~0.82
Mg	0.32~0.78
Citrate	0.04~2.67

Table 2.2 Concentration range of main constituents in bone mineral (dry weight %)¹

The exact mechanism of bone mineralization is still controversial and many previous researchers thought that maybe amorphous calcium phosphate, brushite or octacalcium phosphate can be candidate intermediate phases for final apatite-like phase based on the classical nucleation and growth theory. These claims may think that before postcritical nucleus was formed, atoms or ions were in reversible state to accumulating into cluster. Then once after crystalline postcritical nucleus was formed, by serial addition of ions to the stabilized nucleus, they grow into final crystal. Recently, based on the analysis using cryo-TEM, new approach of cluster agglomeration for bone mineralization was suggested, which thinks that previously stabilized prenucleation clusters might act as a precursor and aggregation of these clusters will lead into the formation of amorphous state⁸⁶⁻⁸⁸. Later amorphous calcium phosphate might gradually transform into final crystal state. The fundamental difference between classical nucleation theory and non-classical nucleation theory is that while classical nucleation

process needs to overcome certain energy critical point to become postcritical nucleus state, non-classical nucleation theory tends to gradually reduce their free energy state toward the final crystal. Still, classical nucleation theory can be sufficiently explained by newly claimed non-classical nucleation theory. Even though this debate is still going on, this notable result not only contributes to revealing the mechanism of bone mineralization, but also gives new insight to the general nucleation theory of material.

While the mechanism of bone formation is unclear, general crystallography analysis of bone was shown to be similar with apatite which was firstly reported in 1926, by De Jong⁸⁹. Later, researchers not only confirmed this fact, but also found that there are several series of apatite-like multi-phases in bone^{90,91}. For example, existence of defective apatite and partially substituted apatite by other various ions were claimed while these several similar apatite-like phases with slight difference of lattice parameters were difficult to be distinguished⁹². Moreover, crystalline phase other than apatite was also reported, such as octacalcium phosphate (OCP), brushite (DCPD) or calcite, despite the fact these claims are based on the specific samples and do not represent for the general state of the bone⁹³⁻⁹⁵. Still, the existence of multi-phase in bone is true from the fact that reported molar ratio between calcium and phosphate in bone is certainly less than stoichiometry apatite (<1.67). In addition, when bone is heat treated above 900 °C, loss of various ions occurs and X-ray diffraction shows mixture of apatite and β -tricalcium phosphate (TCP). During heat treatment, change in X-ray pattern resembled with the aspects of changes in the mixtures of HAP and calcium deficient apatite. Therefore, our bone is constituted of multi-

phases whereas apatite-like phase is the main component.

Similar with the estimation method of the amount of WH in tooth, because it is known that Mg^{2+} is hard to be incorporated in apatite structure and the existence of WH in our osseous tissue was also severally reported, we can estimate the amount of WH in bone from the correlation between the Mg content and amount of the WH. Composition of Mg in inorganic part of bovine bone is reported as 0.436 ± 0.009 wt% which leads to estimation of the content of WH as 20 wt% in bone¹. Similarly, Na and CO_3 in bone structure are known to be related with Na and CO_3 containing apatite ($Ca_7Na_2(PO_4)_3(CO_3)_3(OH)$) and take about 15% of inorganic part of bone tissue. In this premise, rest of the phase is supposed as heavily carbonated defective hydroxyapatite ($Ca_9(PO_4)_{4.5}(CO_3)_{1.5}(OH)_{1.5}$) and its amount is approximately 60%. However, this calculation is still based on atomic weight percentage of component of bone while variations exist in sample to sample, and further research is required for more accurate analysis.

From the observation by electron microscopy, bone crystallites had various shapes such as rod-like and plate-like morphologies⁹⁶⁻⁹⁸. Plate-like crystallites had thickness between 4~6 nm, width between 20~40 nm and length between 30~40 nm. However, some crystallites were much smaller while others were longer. Using X-ray diffraction, average particle size can be derived. From low-angle X-ray scattering, mineral particles of intact human bone had diameter and length approximately 7.5 nm and 21 nm, respectively, on the premise of their shape is rod-like⁹⁹. Then, from the line-broadening measurements, rod-like shape of bone crystals were observed to have diameter and length as 4~4.5 nm and 60~70 nm¹⁰⁰.

Like tooth structure, crystallites in bone are also self-assembled into

hierarchical structure, as shown in Figure 2.2⁸. In the nanometer scale, fibres are hybrid composite consist of the apatite-like mineral and the protein. These fibres compose a fibril which then gathers into lamellae structure. In micrometer scale, osteons and haversian canals are composed with regular pattern of lamellae and pores. Excellent mechanical properties of self-assembled hierarchical structure in natural bone which can sustain our moving body with exceptional levels of damage tolerance inspired many engineers to mimic their synthetic structures. Overall mechanical properties of mammalian compact bone show different strengths according to their direction¹. For compressive strength, longitudinal direction shows 90~150 MPa while tangential direction shows 80~130 MPa. For tensile strength, longitudinally and tangentially measured value showed 50~110 MPa and 5~25 MPa, respectively. Then, the flexural strength in longitudinal direction of bone showed about 120~220 MPa.

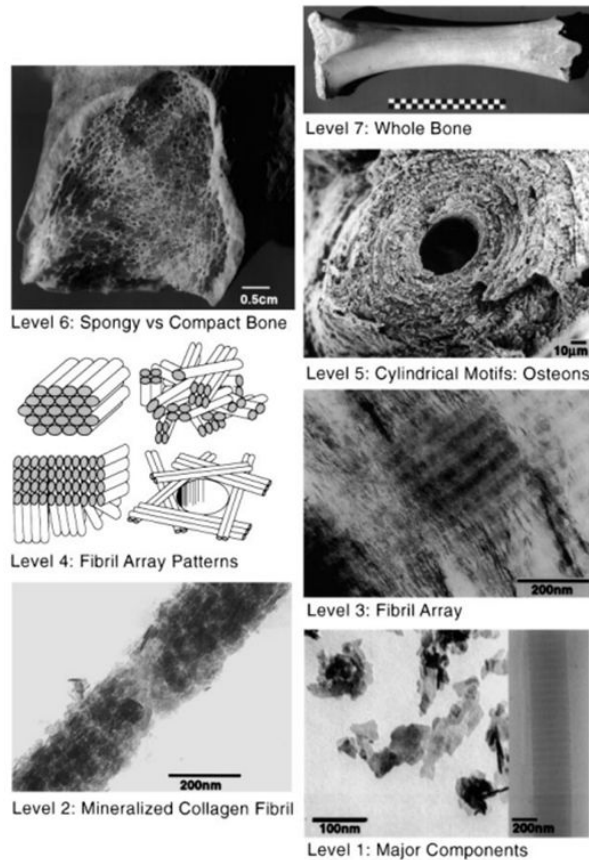


Figure 2.2 The seven hierarchical levels of bone structure⁸. As shown in level 1, calcium phosphate nanocrystals (left) and collagen fibril (right) are the basic components of bone tissue. Level 2: Calcium phosphate nanoparticles self-assembled around collagen fibril. Level 3-Level 4: These mineralized collagen fibrils form array and patterns. Level 5: Osteons and Haversian canals are built based on the fibril patterns. Level 6-7: Based on the distribution of porosity, there are spongy and compact bones, which together make up the whole bone.

In summary, bone is composed of about 70 wt% of mineral, 24 wt% of organic matter and 6 wt% of water. Its major phase is known to be apatite-like compound while the amount of Mg shows that WH might exist up to 20 wt% in inorganic part of the bone tissue. Bone also has self-assembled hierarchical structure which gives exceptional mechanical property.

2.2 General chemistry of calcium phosphate compounds

The calcium phosphate compounds are major constituent of mineral in our bone and tooth, and mainly composed of calcium and tribasic phosphoric acid. From the Le Chatelier's principle, tribasic phosphoric acid has different forms from PO_4^{3-} to H_3PO_4 , based on pH condition. For biomineral in our body, most forms of phosphoric acid are HPO_4^{2-} and PO_4^{3-} while H_2PO_4^- and H_3PO_4 are rarely observed in general situation. As shown in Table 2.3, there are various kinds of calcium phosphate compounds according to their molar ratios between calcium and phosphate. Generally, most of calcium phosphate compounds are in white solid state and have low solubility. However, various ion substitutions can occur with basic forms of calcium phosphate compounds and thus their properties can be modified. In this chapter, we tried to inform several calcium phosphate phases relevant to this thesis with their basic crystallographic information, synthesis method in $\text{Ca}(\text{OH})_2\text{-H}_3\text{PO}_4$ aqueous system and influence of Mg^{2+} during their precipitation.

Ca/P ratio	Mineral name (abbreviation)	Formula
0.5	Monocalcium phosphate monohydrate (MCPM)	$\text{Ca}(\text{H}_2\text{PO}_4)_2 \cdot \text{H}_2\text{O}$
0.5	Monocalcium phosphate anhydrate (MCPA)	$\text{Ca}(\text{H}_2\text{PO}_4)_2$
1	Dicalcium phosphate dehydrate (DCPD)	$\text{CaHPO}_4 \cdot 2\text{H}_2\text{O}$
1	Dicalcium phosphate anhydrate (DCPA)	CaHPO_4
1.33	Octacalcium phosphate (OCP)	$\text{Ca}_8(\text{HPO}_4)_2(\text{PO}_4)_4 \cdot 5\text{H}_2\text{O}$
1.5	α -tricalcium phosphate (α -TCP)	$\alpha\text{-Ca}_3(\text{PO}_4)_2$
1.5	β -tricalcium phosphate (β -TCP)	$\beta\text{-Ca}_3(\text{PO}_4)_2$
1.2-2.2	Amorphous calcium phosphate (ACP)	$\text{Ca}_x(\text{PO}_4)_y \cdot n\text{H}_2\text{O}$
1.5-1.67	Defective hydroxyapatite (DHA)	$\text{Ca}_{10-x}(\text{HPO}_4)_x(\text{PO}_4)_{6-x}(\text{OH})_{2-x}$ ($0 < x < 1$)
1.67	Hydroxyapatite (HAP)	$\text{Ca}_{10}(\text{PO}_4)_6(\text{OH})_2$
2	Tetracalcium phosphate (TTCP)	$\text{Ca}_4(\text{PO}_4)_2\text{O}$

Table 2.3 Various calcium phosphates with their molar ratios of Ca/P, mineral names and chemical formulae.

2.2.1 Kinetically favored intermediate phases; brushite and monetite

Since the stabilities of calcium phosphate compounds are different with each other, most of calcium phosphate intermediate phases can transform into more thermodynamically stable phase according to precipitation condition. For example, as shown in Figure 2.3, hydroxyapatite (HAP) is known to be the most thermodynamically stable compound in neutral and basic region. Therefore, intermediate phases such as amorphous calcium phosphate (ACP), octacalcium phosphate (OCP: $\text{Ca}_8(\text{HPO}_4)_2(\text{PO}_4)_4 \cdot 5\text{H}_2\text{O}$), dicalcium phosphate dehydrate (DCPD: $\text{CaHPO}_4 \cdot 2\text{H}_2\text{O}$) or dicalcium phosphate anhydrous (DCPA: CaHPO_4) are known to eventually turn into HAP in neutral and basic pH region. On the other hand, HAP becomes unstable in acidic pH region. Still, the actual phase of compound earned from the experimental condition depend on kinetic considerations, more willingly than thermodynamic factor, because the growth rate of phase with lower solubility is much slower than kinetically favored ones unless there is supportive effect of temperature or catalyst. In this regard, brushite (DCPD) and monetite (DCPA) are frequently observed intermediate phases of HAP in $\text{Ca}(\text{OH})_2\text{-H}_3\text{PO}_4$ aqueous system, while they both have better stability than HAP in acidic pH region.

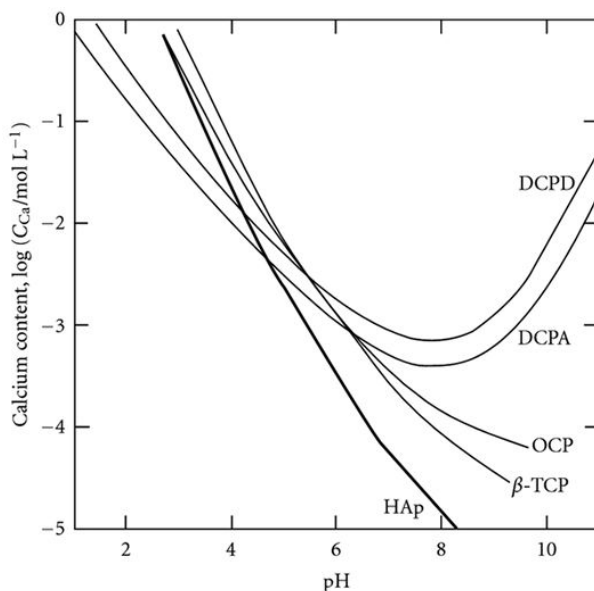


Figure 2.3 Stability curves of calcium phosphate compounds in $\text{Ca}(\text{OH})_2\text{-H}_3\text{PO}_4$ aqueous system at $37\text{ }^\circ\text{C}$, based on the solubility².

DCPD was firstly found in 1865 in phosphatic guano, Avis Island, Caribbean by Moore¹⁰¹. Later, occurrence of DCPD was reported in component of rock-phosphates, ancient bones, dental calculus and pathological calcifications¹⁰²⁻¹⁰⁴. For basic crystal information, DCPD has monoclinic structure with lattice parameters $a = 5.812 \pm 0.002\text{ \AA}$, $b = 15.180 \pm 0.003\text{ \AA}$, $c = 6.239 \pm 0.002\text{ \AA}$ and $\beta = 116^\circ 25' \pm 2'$ ¹⁰⁵. In addition, DCPD is a well-known intermediate phase of HAP under the $60\sim 90\text{ }^\circ\text{C}$ of aqueous condition and below the DCPD/HAP singular point of pH condition. This mineral is known to be more stable in acidic region and thus DCPD can be observed during dissolution of enamel in acid¹⁰⁶. In $\text{Ca}(\text{OH})_2\text{-H}_3\text{PO}_4\text{-H}_2\text{O}$ system, DCPD can be easily synthesized by mixing aqueous suspension of

$\text{Ca}(\text{OH})_2$ with H_3PO_4 in same molar ratio and volume, at $25\text{ }^\circ\text{C}$ ¹⁰⁷ Under the presence of Mg^{2+} in experimental condition, DCPD crystals are disturbed by Mg^{2+} ions and showed unusual phase transformation behavior. From the study of Perez L *et al.* and Zhang *et al.* showed that in the experimental condition of singular point above DCPD/OCP, the transformation of DCPD toward OCP is inhibited by Mg^{2+} ions, even though OCP had lower solubility^{108,109}. Similarly, Nancollas *et al.* reported that the growth of DCPD was retarded under presence of Mg^{2+} in pH 5.6 of supersaturated calcium phosphate solutions. When the concentration of Mg^{2+} was 10^{-3} mole/L, growth of DCPD was completely inhibited. In addition, Rowles' study also reported that WH phase can be partially formed with OCP and HAP, after addition of Mg ($>10^{-4}$ mole/L) with 0.2 g of DCPD in 100 mL solution while stirring at $37\text{ }^\circ\text{C}$ for 24 days¹¹⁰. When the amount of Mg exceeded 10^{-3} mole/L, the conversion of DCPD into OCP was completely inhibited.

The first report of DCPA was in 1882 from the rock-phosphate in Twin islands, Mona and Moneta, in the West Indies¹¹¹. DCPA does not occur in usual circumstances of biological condition and seldom reported in fracture callus¹¹². DCPA has triclinic structure with its lattice parameters; $a = 6.910\text{ \AA}$, $b = 6.627\text{ \AA}$, $c = 6.998\text{ \AA}$, $\alpha = 96.34^\circ$, $\beta = 103.82^\circ$, $\gamma = 88.32^\circ$ ¹¹³. Like in Figure 2.3, DCPA is more stable than DCPD in all pH range, but DCPD is known to have a faster growth rate than DCPA at below $70\text{ }^\circ\text{C}$ ¹¹⁴. When DCPD is heated up to above $80\text{ }^\circ\text{C}$, DCPA is formed^{114,115}. Then, DCPA also transforms into HAP above neutral pH. DCPA can be also precipitated from the reaction between $\text{Ca}(\text{OH})_2$ and H_3PO_4 after 16 hours aging at $85\text{ }^\circ\text{C}$, although this process is supposed to pass through first formation of DCPD¹¹⁶. Similar to DCPD, it is reported that DCPA transforms into other phase under

the presence of Mg^{2+} . For example, when DCPA was aged in 0.05~1 mole/L of magnesium containing aqueous solution at boiling temperature, DCPA transformed into ACP¹, and, when the concentration of magnesium in the aqueous solution was lower, DCPA turned into calcium deficient apatite. WH can also be produced from hydrolysis of DCPA under the presence of magnesium at 95~100 °C for 10 hours, although this method is known to suffer from the variation in crystallinity and formation of other heterogeneous phases such as apatite or amorphous products^{2,117}.

There are also other various intermediate calcium phosphate compounds as mentioned in Table 2.3, but we focused on the description about kinetically favored calcium phosphate phases relevant to this thesis.

2.2.2 Hydroxyapatite and nonstoichiometric apatites

As aforementioned, hydroxyapatite (HAP: $Ca_{10}(PO_4)_6(OH)_2$) is the most frequently observed inorganic phase in living organism and it is one of the most stable form of calcium phosphate compounds. HAP is also found in igneous rocks, metamorphic rocks, phosphate rocks and even in meteorite. Stoichiometric HAP has monoclinic structure and its lattice parameters are $a = 9.4214 \text{ \AA}$, $b = 2a$, $c = 6.8814 \text{ \AA}$ and $\gamma = 120^\circ$ ^{118,119}. However, most of naturally existing HAP or crystallites with apatite structure contain various ions and vacancies which lead them to be highly defective or poorly crystallized. These apatites are known to have hexagonal structure with its lattice parameter approximately $a = b = 9.432 \text{ \AA}$, $c = 6.881 \text{ \AA}$ and $\gamma = 120^\circ$ ¹²⁰, whereas different parameters with some variations are reported depending on

the level of modification in crystal structure^{61,121}. The main difference between apatites with monoclinic structure and hexagonal structure is the direction of OH⁻ arrangement in a given column. In apatite with monoclinic structure, all of OH⁻ ions in a given column are oriented toward same direction and all of OH⁻ ions in the next column have opposite direction. On the other hand, adjacent OH⁻ in the apatite with hexagonal structure points opposite direction with each other and thus, to reduce steric interferences between adjacent OH⁻, some of OH⁻ sites favor to be substituted with other various ions such as F⁻ or left in vacancies to provide a point for column to be reversal¹²⁰. Monoclinic phase of apatite can be transformed into hexagonal phase above the transition temperature of about 200 °C, where reorientation of OH⁻ occurs^{122,123}.

HAP can be easily synthesized by mixing 1 mole of Ca(OH)₂ with 0.6 mole H₃PO₄ in aqueous system. Drop-wise addition of H₃PO₄ into vigorously stirring state of Ca(OH)₂ aqueous solution can be effective to minimize formation of other heterogeneous phases, because addition of large amount of H₃PO₄ at a time can induce temporally strong acidic environment in local region of the Ca(OH)₂-H₃PO₄ system which rapidly grow platelet of DCPD or DCPA in several micrometer scale. However, even when intermediate phases are formed, aging crystallites above neutral pH range or placing them in high temperature environment can make phase transition toward HAP to occur fast. In Figure 2.4, scheme of observed pathway and theoretical pathway of calcium phosphates headed for the final HAP phase are shown.

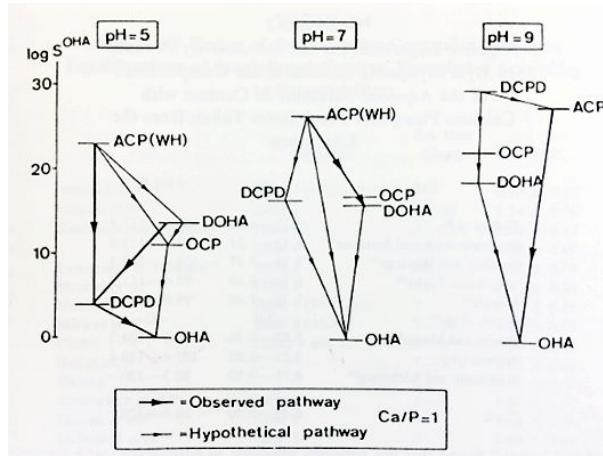


Figure 2.4 Scheme of kinetic pathways of calcium phosphates at various pH conditions.

Generally, apatite structure is very tolerable with partial or sometimes even total substitutions of various types of ions in its Ca^{2+} , PO_4^{3-} or OH^- positions. For example, various cations such as Sr^{2+} , Ba^{2+} , Cd^{2+} , Pb^{2+} are possible substitutes for Ca^{2+} position¹²⁴⁻¹²⁷. In addition, various anions F^- , Cl^- , CO_3^{2-} can substitute OH^- part of apatite¹²⁸⁻¹³⁰, while VO_4^{3-} and AsO_4^{3-} can substitute PO_4^{3-} site of apatite^{131,132}. These are only selected examples of substitutes and various ions can be involved in apatite structure¹³³. When substitution of one kind of ion disturbs overall charge balance of the apatite structure, coupled substitutions with dissimilar charges or vacancies commonly happens to maintain total neutrality. In this respect, nonstoichiometric apatite or defective apatite can precipitate in rather wide range of experimental conditions. Nonstoichiometric apatites have been reported their range of Ca/P molar ratio approximately from 1.40 to 1.75¹³⁴⁻¹³⁶, and also occasionally found to be precipitated out of this range. However,

despite tolerance of HAP structure with various ionic substitution and vacancies, Mg^{2+} can hardly incorporate in HAP. In the presence of Mg^{2+} , structure of HAP prenuclei is distorted and transformation of ACP into HAP is inhibited¹³⁷. Mg^{2+} ions were supposed to be absorbed at the active growth sites of the surface of HAP in terms of Langmuir-isotherm, rather than inside of the crystal structure^{138,139}.

2.2.3 β -Tricalcium phosphate

β -Tricalcium phosphate (β -TCP: $\text{Ca}_3(\text{PO}_4)_2$) has rhombohedral structure with its unit cell parameter as $a = 10.439 \text{ \AA}$ and $c = 37.375 \text{ \AA}$ ¹⁴⁰. β -TCP is a low temperature polymorph of $\text{Ca}_3(\text{PO}_4)_2$ and its transition into α - $\text{Ca}_3(\text{PO}_4)_2$ occurs at $1125 \text{ }^\circ\text{C}$ ¹⁴¹. Because β -TCP and WH have very similar X-ray diffraction pattern from analogous rhombohedral crystal structure, these two phases have been interchangeably recognized. However, while WH certainly has Mg^{2+} and HPO_4^{2-} in its chemical structure, β -TCP does not contain HPO_4^{2-} in its structure. Moreover, while WH can be synthesized under boiling temperature of water due to its stabilized structure from the incorporation of Mg^{2+} and HPO_4^{2-} , β -TCP hardly precipitates in normal aqueous system at low temperature, atmospheric pressure level.

Generally, β -TCP is synthesized by solid state method using starting sources of Ca and P in the ratio of 1.5:1^{142,143}. This synthesis method has been commonly used to produce pure β -TCP or magnesium substituted TCP (TCMP). It is reported that the possible amount of Mg substitution without disrupting β -TCP structure is approximately 15%². However, as the heat

treatment at high temperature is essential to produce β -TCP phase, the resulted particles have micrometer scale and show heterogeneous distribution in their shape. Considering that the process of this synthesis technique is far from the natural precipitation of biomineral, unlike WH, β -TCP cannot be produced in our body circumstance.

Regardless of several limitations, β -TCP has been widely used as commercial material along with HAP in various fields including medical area and there have been many scientific investigations with β -TCP based on its facile synthesis. Therefore, many new findings related to WH in our thesis will be discussed related to previous findings of β -TCP.

2.2.4 Whitlockite

Whitlockite (WH: $\text{Ca}_{18}\text{Mg}_2(\text{HPO}_4)_2(\text{PO}_4)_{12}$) is named after Herbert Percy Whitlock (1868~1948), who was curator of minerals in American Museum of Natural History in New York¹⁴⁴. This mineral has rhombohedral crystal structure (R3c) with its lattice parameter $a = 10.350 \text{ \AA}$, $c = 37.085 \text{ \AA}$ ¹⁴⁵. The unit cell volume is $3,428.79 \text{ \AA}^3$ and molecular weight is 2101.6290 g/mole . Measured and calculated density of this mineral is reported as 3.12 g/cm^3 and 3.102 g/cm^3 , respectively¹⁴⁴. Apparent color of WH powder is white but colorless, grey-white, light pink, light yellow states were also reported¹⁴⁴. In some cases, WH was observed to be transparent or translucent. Hardness of WH is known as 5^{12} . From the observation of optical microscopy, individual particle has rhombohedral morphology¹¹⁷. This information can be changed according to the modification of chemical

structure of WH.

In the presence of Mg^{2+} in calcium phosphate solution, partial formation of WH phase is reported. To precipitate WH, LeGerous et al. added 250 mL of solution containing total 10 mM/L of calcium and magnesium ions into 10 mM/L, 750 mL of phosphate solution by dropwise method¹¹⁷. Authors reported WH produced when Mg/Ca was 0.25 and where the initial pH was 5. WH can also be precipitated by slowly adding mixed solution of calcium chloride plus magnesium chloride and disodium hydrogen phosphate solution into large amount of water, at the same time¹¹⁰. pH was maintained between 5~6 by addition of ethylenediamine solution. Hydrolysis method to synthesize WH from other intermediate calcium phosphate phase was also tried. For example, DCPA was hydrolyzed in solution containing calcium and magnesium at 95 °C for 10 hours and showed WH like X-ray pattern¹¹⁷. DCPD was also partially transformed into WH in 10^{-3} M/L magnesium chloride solutions at 37 °C after 24 day aging¹¹⁰.

However, these methods suffered from the formation of other heterogeneous phases such as apatite or amorphous products². As a result, crystallinity of the precipitants was inconstant. In addition, variations in shapes of WH particles were observed from the SEM image¹¹⁷. Moreover, until now, synthesis method related to physiological environment has not been reported. All of aforementioned methods involved effect of buffers or secondary ions such as NO_3^- or Cl^- , which can remain after precipitation and require several washing processes. We will discuss about precipitating WH in physiologically relevant condition in following chapters of this thesis.

When Mg^{2+} is incorporated, unit cell is contracted and the structure becomes stabilized. As a result, it becomes possible to synthesize WH under

the boiling temperature of water. Another evidence of stability can be increment of the transition temperature of β phase to α phase depending on the incorporation amount of magnesium¹⁴⁶. Other small portions of cations with small radii such as sodium, manganous or ferrous ions can be also supportive to stabilize structure of WH¹⁴⁵, whereas magnesium is mostly found to act as a major role to induce stabilization in biomineral.

In addition, the ion activity product value $-\log I_p^{\text{HA}}$ of WH was estimated between 98 and 102^{1,147}, based on the previous data of compositional analysis of the magnesium containing calcium phosphate related precipitates. In other words, WH was expected to be more stable than DCPD and calcium deficient apatite in neutral pH region, while more soluble than HAP. When this prediction is expressed in the activity diagram of system $\text{Ca}(\text{OH})_2\text{-Mg}(\text{OH})_2\text{-H}_3\text{PO}_4$, probable location of WH can be represented as Figure 2.5. In this thesis, former prediction of stability of WH was modified based on the actual experimental data.

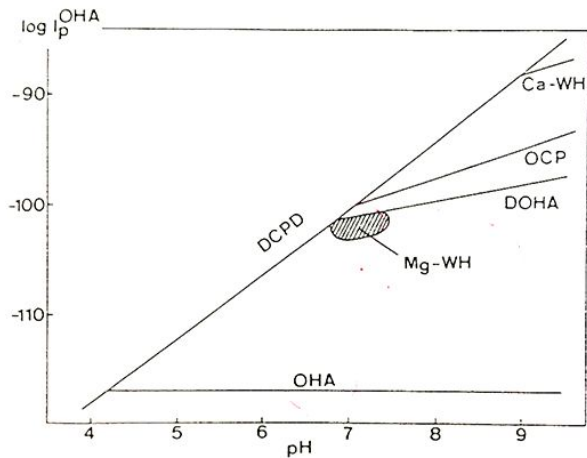


Figure 2.5 Previously predicted probable location of whitlockite, under physiologically relevant condition of $\text{Ca}(\text{OH})_2\text{-Mg}(\text{OH})_2\text{-H}_3\text{PO}_4$ aqueous system

Because other calcium phosphate compounds are investigated more profoundly, we can refer well-known properties of other calcium phosphate compounds to comprehend characteristics of WH. Interestingly, WH and HAP frequently occur together. For example, HAP was found as decomposed product of WH and quartz in the Palermo quarry¹². In addition, WH and HAP are the most abundant mineral in our body. Moreover, hexagonal structure of HAP looks as if it is closely related to rhombohedral structure of WH. However, from the theoretical prediction based on the analysis of their chemical structure, HAP cannot transform into WH with only few atomic rearrangements and considerable reformation of inner structure is needed for phase transition¹⁴⁸. In this respect, WH and HAP are not closely relevant as expected but maybe frequently observed together due to their high stability in kinetic path.

In structural aspect, WH has more close relationship with TCP than HAP. The ratio between cation and anion of WH and TCP are 1.43 and 1.5, respectively, while HAP is 1.67. In addition, both WH and TCP have similar rhombohedral crystal structure. However, TCP phase is usually produced from high temperature heat treatment and thus it is not formed in our body system. On the other hand, WH mineral exists in osseous tissue and can be precipitated under the boiling temperature. FT-IR analysis can be useful to confirm HPO_4^{2-} part of WH, whereas TCP does not show P-O-H bond. Another way to distinguish WH from TCP is comparing their thermal dehydration curves from TGA analysis. While TCP does not show any decrease in its weight depending on the increase of temperature, WH lose HPO_4^{2-} part in its structure and dehydration phenomena occurs. Initial decrement in weight around 100 °C is water evaporation. Then, at around 400 °C and 780 °C, HPO_4^{2-} decomposes into $\text{P}_2\text{O}_7^{4-}$ and PO_4^{3-} , respectively^{117,149}. Decrement of weight around 1035 °C is also known as unique dehydration phenomena of WH¹⁴⁵. After finishing dehydration process, WH transforms into TCP structure which is very obvious evidence of correlation between two phases¹⁵⁰.

2.3 Previous approaches for the fabrication of macroporous bioceramics

There have been many attempts to build porous bioceramics in order to achieve enhanced mechanical property, permeability and capillarity. Most of previous pore forming processes can be classified into four

categories; partial sintering, replica, sacrificial templates and direct foaming^{151,152}. In fact, these are general methods to produce porous structure of various kinds of ceramic. Although previous techniques are limited in fabricating pores with their dimensions larger than micrometer, porous ceramics made from these methods are not only successfully used in medical field but also vigorously applied in various other industrial fields for water purification, thermal insulation, catalytic reaction and filtration. In this chapter, general previous methods of making macroporous calcium phosphate scaffold will be briefly introduced (Figure 2.6).

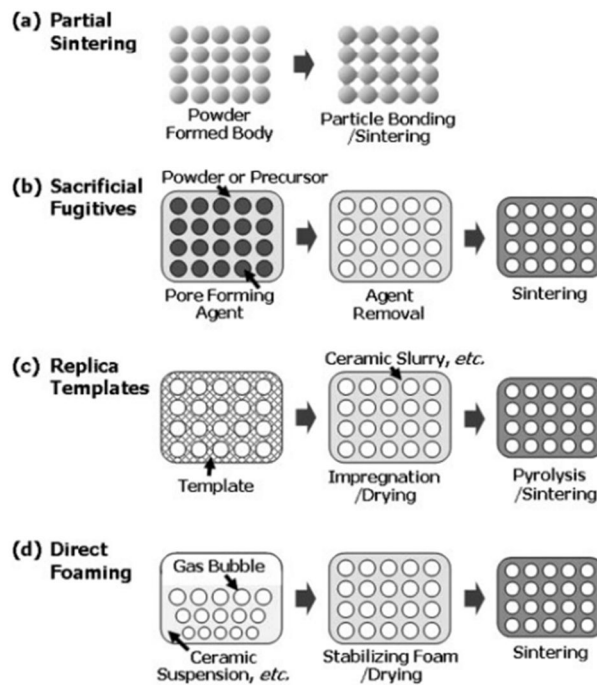


Figure 2.6 Current methods to fabricate porous bioceramics in micrometer scale¹⁵²

Partial sintering method intentionally maintains pores by terminating the sintering process before the sample becomes fully densified while simultaneously utilize strong bridging formation between grains made from surface diffusion during sintering process. For example, HAP granule consists of agglomeration of particles with diameter of 10 nm can be prepared in approximate size of 3~30 μm by spray drying method¹⁵³. After HAP granules were sintered up to desired temperature, particle or grain size increased about from 28 nm to 297 nm while pore volume decreased approximately from 0.073 cm^3/g to 0.003 cm^3/g , respectively, when sintering temperature were 750 $^\circ\text{C}$ and 1000 $^\circ\text{C}$. It is known that the porosity decreases depending on the sintering temperature, time and pressure level¹⁵⁴. Usually, the porosities of ceramics made by partial sintering method are under 50%¹⁵².

Replica method was invented by Schwartzwalder and Somers in early 1960s. This is also known as the first technique to produce porous ceramic. Since then, replica method has been used as one of the most popular methods to make porous ceramic structure in industrial fields due to its simple process. To make porous bioceramic using the replica method, viscous ceramic suspension or precursor solution is infused in a cellular structure which acts as a template. Then the internal pores of the template is filled and coated with ceramic material. After removal of polymer template by pyrolysis, the final ceramic product becomes same morphology with the original cellular structure and can be densified by sintering at appropriate temperature. Synthetic polymer (such as polyurethane), carbon foam, coral and wood can be used as a template. For example, macroporous HAP scaffolds with pore size of 200~400 μm was prepared by impregnating HAP

slurry in the polyurethane sponge¹⁵⁵. HAP was initially mixed with monomers (acrylamide, methylenebisacrylamde), dispersant and surfactant. Before soaking the polymer template into HAP slurry, catalyst (ammonium persulphate) and initiator (tetramethylethylenediamine) was added to start polymerization of the monomers. After polyurethane sponge was soaked with HAP slurry, polymerization proceeded. The dried samples were heated up to 600 °C to burn out the polymer sponge and then sintered at 1350 °C for 2 hours. The resulted porous HAP scaffold showed similar compressive modulus, yield strength and elastic modulus with that of cortical bone.

Macroporous HAP and WH can also be produced based on natural template such as hard tissue of the coral¹⁵⁶. Using hydrothermal method, $(\text{NH}_4)_2\text{HPO}_4$ can react with CaCO_3 , which is the major phase of the coral, and form HAP or WH while preserving original architecture of the coral. Most of porous ceramics made from this synthetic template have open porosity within the range of 40%~95% and sizes of pores are between 200 μm and 3 mm. However, it is hard to produce pores less than 200 μm from the difficulty of impregnating pores of template with ceramic suspensions. In the case of natural template such as wood, pore size can be obtained approximately 10~300 μm and porosity can vary within the range 25~95%. In addition, because tree template has oriented porous structure, resulted macroporous ceramic also has anisotropic mechanical properties, similar with natural structure. Still, using natural template is much more complex than synthetic template. Moreover, it is stated that removal of template during pyrolysis process, cracks often occur in the reticulated structure made from both synthetic and natural template and degrade the mechanical strength. This problem is known to be possible to overcome by enhancing

integrity of the material using additives, reactive compounds or fibers. It is also reported that using preceramic polymers instead of ceramic suspension can be effective at avoiding cracks.

The sacrificial template method use fugitives which eventually become pore structure and thus act as negative replica for the macroporous ceramic. For the sacrificial template, organic materials are frequently used but liquids salts and even metal or ceramics can also be employed. Later, sacrificial fugitives can be eliminated by chemical treatment or heat treatment as they burn out. Salts are extracted by several washing process while metal or ceramic fugitives are removed by chemical agents such as acidic leaching. Templates like naphthalene, which easily sublimate, can be eliminated in mild condition, while most of organic fugitives can be burned out after high temperature heat treatment. One general example can be a porous HAP fabricated with poly vinyl butyral as a sacrificial fugitive¹⁵⁷. Various sizes of PVB agents (0.093 mm, 0.188 mm, 0.42 mm) induced different sizes of macropores in HAP and the porosity volume (33%~78%) showed high correlation with the compressive strength (correlation factor > 0.96). HAP granules with its diameter about 100 μm was mixed with PVB in volume of about 24~61% and uniaxially pressed in rectangular form. The HAP-PVB blocks were heated up to 500 °C to burn out PVB particles and void part was created in similar morphology with initial PVB templates. Finally HAP block was sintered up to 1200 °C for complete densification.

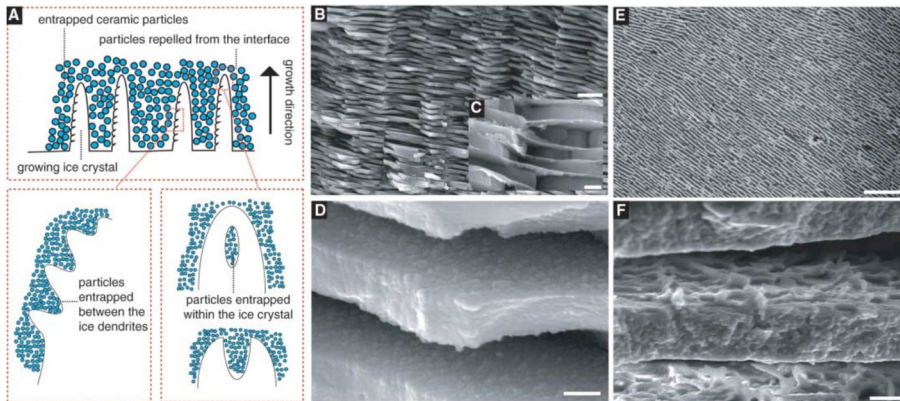


Figure 2.7 Fabrication mechanism of freeze casting method and similar natural structure. **a**, Ice grows in lamellar structure parallel to the freezing direction, while expelling inorganic particles. Nacre structure (**b-d**) and inorganic material fabricated by ice template (**e, f**) shows similar lamellar structure. Scale bars in figure b, c, d, e and f show 5 μm , 0.5 μm , 0.3 μm , 300 μm and 10 μm , respectively¹⁵⁸.

Another notable example of sacrificial template method is freeze casting technique which uses water or camphene as fugitives. As shown in Figure 2.7, while ceramic suspension is freezing unidirectionally, ice is formed in lamellar microstructure parallel to the freezing direction while repelling ceramic particles. Then, after sublimation of ice, final porous ceramic can be made with morphology of negative replica to initial structure of ice. In this way, Sylvain Deville *et al.* unidirectionally froze HAP slurry to fabricate ice-templated (IT) layered material showing its compressive strength four times stronger than that of conventional porous HAP¹⁵⁸. General pore dimension and porosity of macroporous ceramic fabricated by

the sacrificial template method is reported approximately in the range of 1~700 μm and 20~90%, respectively. Problem of sacrificial template method is that cracks can be occasionally occurred when there is mismatch between fugitives and ceramics during thermal expansion. In order to reduce crack formation, slow and careful removal of sacrificial template is needed, although this might extend overall process time too long. In addition, excessive amount of gases can be generated during burn out process of fugitives.

Direct foaming method is another simple technique to produce macroporous ceramic which directly utilize stabilized state of air bubbles in ceramic suspension and thus no more additional step of eliminating fugitives is required. Still, in most of case, sintering is proceeded in order to increase mechanical property by densification. For instance, initially, HAP powder can be mixed with water and surfactant to foam into slip¹⁵⁹. By stirring the slip in high speed of 1200 rpm, air bubbles were homogeneously introduced. After drying in a box made of filter paper, HAP green body was sintered at 1000~1350 $^{\circ}\text{C}$. As a result, HAP with open cell structure with density higher than 15% was made. Surface agents such as lipids or proteins with long amphiphilic chains can be used to reduce interfacial energy between air and liquid. General ranges of porosities and pore sizes of macroporous ceramic fabricated from direct foaming method are 40~97% and 35 μm ~1.2 mm. However, by modifying surface of the particles, colloidal particles adsorb at the interface of air and liquid which results long term stability. In this way, pore size can be decreased to 10 μm . Reaction speed is also important criteria to consider. Otherwise, due to thermodynamic instability, small bubbles eventually coalescence with each other and grow into large bubbles

in spontaneous movement by mechanism of Ostwald ripening. Toxicity of additives and atmosphere sensitivity should also be considered during utilization of direct foaming method.

While these four methods are actively applied in commercial fields, more advanced techniques to develop hierarchical porous structure and interconnected pores in nanometer scale are still under investigation in order to mimic structure of the naturally existing hard tissue. Hierarchical structure has advantage that various sizes of pores can provide synergy effects for efficient supply, which is essential in maintaining living organism. In fact, random hierarchical structure can be easily fabricated by mixing various sizes of fugitives or grafting porous ceramics with different pore scales while unidirectional porous structure can be achieved by freeze casting. Despite, fabrication technique of hierarchically interconnected nanoscale porous structure with directionality in bioceramic is still under investigation. As a result, the effects of nanochannels in mechanical property or maintenance of life are not fully understood. The finding in this thesis to fabricate hierarchical nanochannel in bioceramic will be helpful to investigate its contribution in living organism and can also be applied in various industrial fields including areas related to previous macroporous ceramics.

Chapter 3. Experimental Procedures

3.1 Sample preparation of whitlockite

Synthesis of whitlockite nanoparticle

In order to synthesize whitlockite (WH: $\text{Ca}_{18}\text{Mg}_2(\text{HPO}_4)_2(\text{PO}_4)_{12}$), we used precipitation method with calcium hydroxide ($\text{Ca}(\text{OH})_2$, 99.0%, High Purity Chemical, Japan), magnesium hydroxide ($\text{Mg}(\text{OH})_2$, 95.0%, Junsei Chemical Co., Japan) and phosphoric acid (H_3PO_4 , 85.0%, Junsei Chemical Co., Japan) in an aqueous system. First, 500 mL of $\text{Ca}(\text{OH})_2$ and $\text{Mg}(\text{OH})_2$ were mixed with the suggested ratios in Table 3.1, and heat was applied between 60-90 °C to achieve a fast kinetic reaction. Then, according to Table 3.1, 500 mL of an appropriate concentration of H_3PO_4 was added dropwise at a speed of 12.5 mL/min into the $\text{Ca}(\text{OH})_2$ and $\text{Mg}(\text{OH})_2$ mixed solution using a digital burette (Metrohm 876, Dosimat Plus) while vigorously stirring. The precipitates were aged for more than 9 hours and then collected by filter-press method and dried using a lyophilizer.

Sample	Cation		Anion
	Ca(OH) ₂	Mg(OH) ₂	H ₃ PO ₄
WH1	0.86 M	0.14 M	0.85 M
WH2	0.81 M	0.19 M	0.9 M
WH3	0.77 M	0.23 M	0.95 M
WH4	0.74 M	0.26 M	1 M
WH5	0.71 M	0.29 M	1.05 M
WH6	0.69 M	0.31 M	1.1 M

Table 3.1 Synthesis condition for whitlockite in Ca(OH)₂-Mg(OH)₂-H₃PO₄ aqueous system

Synthesis of hydroxyapatite, tricalcium phosphate, magnesium substituted tricalcium phosphate

Hydroxyapatite (HAP: Ca₁₀(PO₄)₆(OH)₂) was also synthesized using a similar precipitation method with identical starting materials of Ca(OH)₂ and H₃PO₄. Initially, 500 mL of a 0.5 M Ca(OH)₂ aqueous solution and 500 mL of a 0.3 M H₃PO₄ aqueous solution were prepared. Then, the H₃PO₄ solution was added dropwise at a speed of 12.5 mL/min using a digital burette to the Ca(OH)₂ aqueous solution while continuously stirring. After 24 hours of aging process for sufficient reaction, the precipitants were filter-pressed to be collected and freeze-dried.

Tricalcium phosphate (TCP: Ca₃(PO₄)₂) and magnesium-substituted tricalcium phosphate (TCMP: Ca_{2.86}Mg_{0.14}(PO₄)₂) were synthesized from a general solid-state method using calcium carbonate (CaCO₃, 99.99%, High

Purity Chemical, Japan), magnesium carbonate (MgCO_3 , 99.9%, High Purity Chemical, Japan) and diammonium hydrogen phosphate ($(\text{NH}_4)_2\text{HPO}_4$, 99.0%, Junsei Chemical Co., Japan). Each sample was prepared according to its molar ratios and mixed with 1% dispersant in a 50 mL of ethanol solution. The weight ratio between ethanol and the whole powders was 1 to 1. After all the samples were ball milled for 48 hours, green powders were collected by evaporating ethanol by heat. Then the green powders were sintered at 1100 °C for 2 hours. All the samples were finely grounded into powders for further use.

3.2 Analysis methods of synthesized whitlockite

Basic property of whitlockite

X-ray diffraction (XRD, M18XHF-SRA, MAC Science Co.) was used to analyze the crystal structures of WH, TCP and TCMP with monochromatic Cu $K\alpha$ radiation ($\lambda = 1.5405 \text{ \AA}$), at a scan rate of $1^\circ/\text{min}$. To examine the overall morphologies of the WH nanoparticles, Field emission scanning electron microscopy (FESEM, JSM-6330F, JEOL) was used. Before observation, all samples were coated with thin layer of platinum by Pt sputter (Coater Pt, MSC-101, JEOL) for optimal electron conductivity to prevent charge-up phenomena. To examine more detailed individual morphologies of the WH nanoparticles, the WH nanoparticles were dispersed in ethanol and loaded on a TEM copper grid. Then, the shapes of

WH nanoparticles were observed using high-resolution transmission electron microscopy (HRTEM, JEM-3000F, JEOL), and their d-spacing values were also measured.

HPO₄²⁻ group evaluation

The atomic structures of WH, TCP and TCMP were built using the software CrystalMaker[®] (CrystalMaker Software Ltd, Oxford, England (www.crystallmaker.com)) based on previously reported crystallographic databases of WH¹¹, TCP¹⁶⁰ and TCMP¹⁶¹. Fourier transform infrared (FT-IR, Nicolet 6700, Thermo Scientific) analysis was performed to confirm HPO₄²⁻ group existence in the chemical structure of the synthesized WH. Each sample was homogeneously grounded with potassium bromide (KBr) in approximate ratio of 1 to 99 and pelletized to be analyzed in transmission mode. Thermogravimetric analysis (TGA, Simultaneous DTA/TGA analyzer, TA instruments) was conducted from room temperature to the temperature as high as 1100 °C with a 10 °C/min heating rate in a nitrogen atmosphere to study the dehydration phenomenon of WH. In addition, the ratios of Ca, Mg and P in the WH samples synthesized from various experimental conditions shown in Table 3.1 were analyzed using an inductively coupled plasma optical emission spectrometer (ICP-OES, Varian 720-ES). All the samples were washed for three times in distilled water to avoid ions absorbed on the surface of the particles.

Stability test

To examine the stability of WH in various pH conditions, 1 g of WH was dispersed in 100 mL of distilled neutral water for 1 month. WH was also dispersed in a pH 12 sodium hydrogen phosphate/sodium hydroxide buffer for 15 days at 90 °C, while kept in continuously stirring state. In addition, to compare stability between WH and HAP, 1 g of WH and HAP were dispersed in 100 mL of H₃PO₄ aqueous solutions, which were titrated from pH 2.5 to pH 5.0 at room temperature. After 24 hours of aging, each remaining powder was carefully collected by centrifuge (13000 rpm, 10 minutes) and freeze-dried. Then, the remaining amount of the powder from each pH condition was measured accurately by weight to compare its solubility. Each sample was analyzed in triplicate.

Component analysis of intermediate phases of whitlockite

In addition, to comprehend kinetic mechanism of WH, we collected precipitant from different experiment time. XRD analysis was done to examine crystallographic information of the intermediate phases and FESEM was used to directly observe their morphological change. Inductively Coupled Plasma (ICP) was performed to analyze component ratio between Ca²⁺ and Mg²⁺ in the precipitant of different experiment time. Ion chromatographic analysis (Ion Chromatograph 1, ICP-3000, Dionex) was conducted to observe the change of the amount of Ca²⁺ and Mg²⁺ free ions in the system. Filtrates were obtained from the slurries of different experiment time by filter-pressed method.

Mechanical test

In order to evaluate the mechanical properties of the whitlockite, micro-indentation test was carried out. Micro-indentation tests were performed using a Nanovea micro-indentation system in load control at a constant loading rate of 4 N/min. A Berkovich-type indenter was used to measure micro-hardness of the whitlockite. Maximum load and dwell time were 2 N and 5 seconds, respectively. Five points on the specimen were tested and the statistical processing was conducted.

Fabrication of whitlockite into various types of bone implant

To make porous WH implant, we gently mixed bead type of polymethyl methacrylate (PMMA, Bead & Micro) with diameter of 330 μm into WH nanoparticles in 1:2 weight ratio which was optimized condition we found for the proper porosity. Then, using a cylindrical mold, PMMA-WH mixture was fabricated into cylindrical pellet by giving pressure of 2 ton for 3 seconds. During heat treatment up to 700 $^{\circ}\text{C}$, PMMA beads were burned out and porous structure was formed. Similarly produced PMMA-HAP pellets and PMMA-TCP pellets were heat treated up to 945 $^{\circ}\text{C}$ and 1050 $^{\circ}\text{C}$, respectively, to achieve similar hardness value with each other. Then, to make samples with size about 1 mm, we crushed WH porous scaffold and selected the pieces which were placed between the sieve with 1.18 mm pore size and the sieve with 890 μm pore size. Sample morphology was confirmed by optical microscope.

To make cylindrical WH implant, we homogeneously mixed WH

powder with PVA binder in 10000:1 weight ratio and pelletized by using cylindrical mold with diameter of 4 mm. 0.125 g of WH was used to fabricate each cylindrical pellet with height of 4 mm, by applying 1 ton of pressure for 3 seconds. For both HAP and TCP pellets, 0.15 g of powder was used to fabricate each cylindrical pellet. Then WH pellets were heat treated up to 700 °C. For the *in vivo* test samples, to observe recovery level of bone, we made channels with dimension of about 300 µm in every cylindrical pellet by laser fabrication. Overall sample morphology was observed by optical microscope.

Analysis of uptake level of fluoride ions

To observe chemical stability of WH with F⁻ free ions, 500 ppm of sodium fluoride (NaF, 99.0%, Sigma Aldrich) was ionized in distilled water at room temperature. Then 5 g of HAP, TCP, TCMP and WH were added into NaF aqueous solution and aged for 24 hours while maintaining stirring. Each sample was centrifuged by 12000 rpm for 10 minutes and its supernatant was carefully separated by pipette. Then the residual free F⁻ ion was measured by ion chromatography analysis (Ion Chromatograph 1, ICP-3000, Dionex).

3.3 Design and fabrication of AMCD-HAP

HAP was synthesized by a precipitation method with calcium

hydroxide ($\text{Ca}(\text{OH})_2$, 99.0%, High Purity Chemical, Japan) and phosphoric acid (H_3PO_4 , 85.0%, Junsei Chemical Co., Ltd) in water-base solution. Similar with aforementioned synthesis method of HAP in section 3.1, 0.5 M $\text{Ca}(\text{OH})_2$ solution was prepared in 500 mL of distilled water. After stirring vigorously with an overhead mechanical stirrer (overhead stirrer, MSM-1 Jeio Tech) for more than an hour, 500 mL of 0.5 M H_3PO_4 was added drop-by-drop using a digital burette (Metrohm 876, Dosimat Plus). The final molar ratio of $\text{Ca}(\text{OH})_2$ and H_3PO_4 was 10:6, which was same with the compositional ratio of HAP, and the precipitates were aged for 24 hours to complete the reaction while stirring at room temperature. Then, the HAP slurry was filter-pressed and freeze-dried. Dried HAP powder was homogeneously mixed with polyethylene glycol (PEG: $\text{HO}-\text{CH}_2-(\text{CH}_2-\text{O}-\text{CH}_2)_n-\text{CH}_2-\text{OH}$) with various molecular weights of MW 400 ($M = 380\sim 420$ g/mole, Sigma Aldrich), MW 2,000 ($M = 1,800$ g/mole, Merck), MW 10,000 ($M = 9,000$ g/mole, Merck) and MW 600,000 ($M = 600,000$ g/mole, Sigma Aldrich). In standard sample, we mixed HAP and PEG with the weight ratio of 10:1. PEG was dissolved in small amount of distilled water and mixed until uniformly distributed with HAP nanoparticles by grinding. To make nonporous HAP pellets for reference, PEG binder amounting to only 0.0001% by weight was homogeneously mixed with HAP powder.

Various ratios of HAP-PEG mixture (PEG:HAP = 1:1, 1:5, 1:10) were made into rectangular pellets in a 37 mm \times 7 mm \times 2 mm aspect shape, using pressing mold, by applying a pressure of 2 tons for 3 seconds. Then, the HAP-PEG pellet was sintered at 1,100 °C for 2 hours with a 5 °C/min heating rate. During sintering, a right-triangular prism-shaped metal wedge with its width, thickness and height as 190 mm \times 5 mm \times

40 mm, made from stainless steel (SUS310S) or super alloy (HAYNES 230), was placed atop the HAP-PEG pellet to provide pressure energy that gradually increased with the slope of the wedge. To prevent contamination, an alumina ceramic (Al_2O_3) plate was placed between the metal wedge and the HAP-PEG pellet. Nonporous HAP pellets or random porous HAP pellets were made using identical experimental procedure but without applying additional pressure energy during the sintering process. AMCD-WH pellets were also fabricated from similar preparation process with AMCD-HAP pellets.

3.4 Analysis methods of AMCD-HAP structure

Porosity analysis

The basic surface morphology of the AMCD-HAP was observed by field emission scanning electron microscope (JSM-6330F, JEOL) after coating thin layer of platinum by Pt-sputter (Coater Pt, MSC-101, JEOL). To analyze porosities in different part of AMCD-HAP pellet, the AMCD-HAP sample was cut into three regions (HP: high pressurized region, MP: medium pressurize region, LP: low pressurized region) and gas adsorption-desorption was measured in each region. N_2 adsorption was measured at 77 K using a BELSORP-mini II (BEL Japan Inc., Japan) after degassing under vacuum condition at 150 °C for 24 hours. Specific surface area was calculated using the BET (Brunauer-Emmett-Teller) equation with a 0.01~0.20 relative pressure range.

Mechanical test

In order to determine the overall compressive strength and modulus of the graded HAP with porosity, uniaxial compression tests for rectangular specimens were performed at a constant strain rate of $1.5 \times 10^{-2} \text{ sec}^{-1}$. In order to examine the mechanical properties of each region of the AMCD-HAP (H: the highest pressure energy applied area, LH: little high pressure energy applied area, LL: little low pressure energy applied area, L: the lowest pressure energy applied area), micro-Vickers hardness was conducted. Maximum load and dwell time were set to 4.9 N and 5 seconds, respectively. Ten points for every cross-section were tested and averaged.

FIB-FESEM 3D reconstruction and HRTEM analysis

To reconstruct 3D images and movies of the interconnected pore structures inside AMCD-HAP pellets, we conducted FIB-FESEM tomography (Auriga, Carl Zeiss). Two different regions of LH and LL pressure gradient sections from the identical AMCD-HAP sample were sectioned by FIB with magnification of $\times 32,000$. Every interval between slices was 15 nm and the total number of slices used for each 3D image was 200. During FIB operating, the milling current was 120 pA and the tilting angle was approximately 54° . We used 3D image processing program Amira (Carl Zeiss, version 5.3.3) to define regions of interest (ROI) and to construct 3D images with dimensions $4.0 \times 3.7 \times 3.0 \mu\text{m}^3$. In addition, to prepare samples for the TEM observation, Nano-CT scanning and synchrotron nano-imaging analysis, a focused ion beam (FESEM-FIB, FEI NOVA Nanolab 200 dual beam system) was used to take samples. A

platinum gas injection system was applied to attach grids and form deposit for protecting the microstructure of the samples. A high-energy Ga ion beam (30 kV, 7 nA ~ 20 nA) was used to analyze the microstructure of the pellets. A low-energy Ga ion beam was used for cross-sectioning (30 kV, 50 pA ~ 5 nA) and cleaning (5 kV, 70 pA) during the TEM sampling and Nano-CT sampling process. Higher emissions were needed to make larger cylindrical samples for 3D reconstruction using synchrotron radiation (PLS, Pohang Light Source). Samples were lifted out using an Omniprobe system (Tungsten needle, Omniprobe) with a sharp tip. TEM samples were adhered to a 3-post Cu grid (Ted Pella, Inc.), Nano-CT samples were placed on top of a needle (Korea Vaccine CO., LTD) and PLS samples were loaded on the copper mesh grid (Ted Pella, Inc). Nano-size pores and channels of HAP were observed by high-resolution transmission electron microscopy (FEI, Tecnai F20) and confirmed by energy dispersive spectrometry (EDAX) techniques.

Cyclotron 7C XNI Imaging

Synchrotron nano-imaging analyses were carried out at the 7C (XNI) beamline of a Pohang Light Source. High flux monochromatic 6.7 keV X-rays were focused using beryllium compound refractive lenses ($f = 3.5$ m). The sample was located at the focal point of the lenses. The beam size at the sample position was about 50 μm and the photon flux was estimated to be approximately 10^{12} photons/sec. In order to minimize spatial coherency and homogenize the illumination, a diffuser was installed in front of the sample. The sample was loaded on a three-axis piezo-driven scanning

stage on top of an air-bearing rotation stage. Tungsten zone plate with diameter of 140 μm , thickness of 1 μm and width of the outermost zone of 50 nm was used to magnify the X-ray image with resolution of about 40 nm. In order to achieve phase contrast, a holed aluminum-film phase plate with thickness of 3.87 $\mu\text{m} \pm < 1\%$ and diameter of hole with 5 μm was located in the back focal plane of the zone plate. The thickness was optimized so as to phase shift the diffracted beam by $\pi/2$ and thereby make the sample image darker in the bright field. The detector, consisting of a thin Tb:LSO scintillator crystal with thickness of 10 μm and an optical microscope with magnification of $\times 20$, was positioned 2.46 m downstream from the sample. The CCD of the optical microscope had 2048 \times 2048 pixels that are 18 μm . The total magnification of the system was $\times 1230$ and the corresponding effective pixel size was 15 nm. 3D tomographic images were constructed from 181 images that were collected over an angular range of 180° with 10 seconds of exposure time for each.

Capillary rise test

The capillary rise test was conducted in a double walled vessel to keep constant temperature. Cooled isopropanol was circulated between the double walls of the vessel to maintain the inside container at a consistent temperature of 25 °C. To fix the humidity level at a constant value, the bottom of the inside container was covered with silicagel blue (DaeJung) and Drierite (Hammond company). AMCD-HAP, non-porous HAP, and randomly porous HAP pellets were partially immersed vertically in distilled water. A 1 mm calibrated scale was used to measure the rise of fluid using a

red ink dye. The number of samples used for each condition was $n = 3$ and the results were presented by average.

¹⁸F-fluoro-deoxyglucose positron emission tomography (FDG-PET)

To compare fluid migration of the AMCD-HAP and the non-porous HAP pellets *in situ*, ¹⁸F-fluoro-deoxyglucose (FDG) positron emission tomographic (PET) and computed tomography (CT) scanning were conducted (NanoPET/CT, Mediso, Medical Imaging Systems, Budapest, Hungary). Each pellet was oriented vertically in a sterile container filled with 3 ml of distilled water containing ¹⁸F-FDG (100 μ Ci). The PET image was acquired by scanning in list mode for 60 minutes. CT and PET images were reconstructed as maximal intensity projection images. All images were compared using the same image window settings.

3.5 Biological evaluation of whitlockite and AMCD-HAP

Fabrication of whitlockite scaffold

To compare basic biocompatibility of the WH with HAP and TCP, all samples were fabricated into scaffolds for cell tests. Powders were made into cylindrical pellet form with diameter of 1 cm using pressing mold by applying a pressure of about 2 tons for 3 seconds. Then these pellets were heat treated up to 700 °C for 2 hours with a heating rate of 5 °C/min. After

sterilization process by using autoclave at 130 °C for 20 minutes, each pellet was dried under UV irradiation and placed in the 24 well plates.

Cell proliferation test on whitlockite scaffold

Lonza Clonetics human osteoblasts were seeded on the surface of each pellet at a density of 1×10^5 cells/mL (day 0) with Lonza osteoblast basal medium containing fetal bovine serum (FBS), ascorbic acid and GA-1000. Then, cell seeded samples were carefully kept in a water-jacketed incubator maintained at 37 °C and 5% CO₂. After 1 day, 4 day, 7 day and 10 day, pellets with cell grown on its surfaces were taken out in forward direction and moved into new 24 well plates. Each surface of the pellet was gently washed with phosphate-buffered saline (PBS, Cellgro, Mediatech. Inc). Then 20 µl of 5 mg/mL MTT (Thiazolyl Blue Tetrazolium Bromide, Sigma) solution diluted with media (MTT:media = 1:9) was added on the top surface of each pellet. MTT solutions were severally pipetted to sufficiently cover the whole surface of the pellets. All the samples were kept in the CO₂ incubator for 2 hours. After gentle PBS washing, 200 µl of Dimethyl sulfoxide (DMSO, Sigma) was added on each surface of the pellet to break cell membrane. Solution from the each sample was collected in 96 well plates and the absorbance was measured immediately by the multiple plate reader (victor 3, Perkin Elmer) at 544 nm.

To directly observe cell growth state on each surface of the pellet, we obtained cell stained images. After 4 day and 7 day from the seeding point, cells grown on the surface of each sample were fixed with 3.7% formaldehyde (Sigma) diluted in PBS for 10 minutes. Then, the cells were

permeabilized with 0.2% triton X-100 (Sigma) diluted in PBS for 10 minutes. The actin cytoskeleton networks of the cells were stained with phalloidin (Phalloidin, fluorescein isothiocyanate labeled, Sigma) for 90 minutes and then, nuclei of the cells were stained with DAPI (4',6-Diamidino-2-phenylindole dihydrochloride, Sigma) for 10 minutes. After every step, the samples were gently washed with PBS to remove remaining chemicals. Finally, cell proliferation state on the surface of the pellet was directly observed by fluorescence microscopy (Axio Observer Inverted Microscope, Carl Zeiss).

RNA level of cellular activity test on whitlockite scaffold

To study RNA activity levels of cells grown on each surface of the pellet, Real time PCR was performed by Rotor gene Q (Qiagen, Santa Clarita, CA) using the Rotor gene SYBR green PCR kit. After 2 days from the seeding point of the cells on the pellet, RNA of cells grown on each sample was extracted by a RNA extraction reagent (RNAios Plus, Takara). First strand cDNA was synthesized from collected RNA with a QuantiTech reverse transcription kit (Qiagen). We used primers from QuantiTect Primer Assay (Qiagen) as shown in Table 3.2.

Gene	Symbol	Description
18S ribosomal RNA	<i>RRN18S</i>	QT00199367
Alkaline phosphatase	<i>ALP</i>	QT00012957
Bone gamma-carboxyglutamate (<i>Gla</i>) protein	<i>BGLAP</i>	QT00232771
Bone morphogenetic protein 2	<i>BMP2</i>	QT00012544
Collagen type I	<i>COL1</i>	QT00037793
Integrin-binding sialoprotein	<i>BSP</i>	QT00093709
Runt-related transcription factor 2	<i>RUNX2</i>	QT00020517
Secreted phosphoprotein 1	<i>SPPI</i>	QT01008798
Secreted protein acidic cysteine-rich	<i>SPARC</i>	QT00018620

Table 3.2 List of primers used for real time PCR (purchased from QuantiTect Primer Assay, Qiagen)

To amplify cDNA, the initial activation step was proceeded for 3 minutes at 95 °C. Then denaturation and annealing extension cycle were conducted at 3 seconds at 95 °C and 10 seconds at 60 °C, respectively. Differences of relative gene expression between samples were calculated using the $\Delta\Delta C_t$ method. The numbers of samples used for WH and for the control HAP were both $n = 5$ and each sample was subjected to analysis in triplicate.

The statistical analyses were calculated using SPSS version 21.0. The statistical significances between two groups were compared using Student's t-test after their normal distribution was confirmed by Shapiro-Wilk test ($\dagger p < 0.1$, $\dagger\dagger p < 0.05$, $*p < 0.01$, $**p < 0.005$, $***p < 0.001$).

Protein level of cellular activity test on whitlockite scaffold

To investigate protein activity level of cells grown on the WH scaffold, we conducted Western blot after 48 hours of human osteoblast culture on scaffolds. Initially, cell grown pellets were gently washed with PBS and moved into new 24 well plates. Then cells were quickly isolated by Trypsin-EDTA (Cellgro, Mediatech. Inc) and washed with PBS. Proteins from the isolated cells were extracted by using RIPA (Radioimmunoprecipitation assay buffer, Sigma-aldrich) buffer. To prevent proteins from denaturing, protease inhibitor cocktail solution (Sigma) was simultaneously used with RIPA buffer in ratio of 9:1. After vortexing for 1 minute, the sample was cooled on the ice and this procedure was repeated for three cycles. Then samples were centrifuged at 3000 rpm for 5 minutes and supernatants including proteins were gently separated. To examine the amount of the protein, Bradford assay was done using nanodrop (NanoDrop2000c Spectrophotometer, Thermo Scientific). Each protein was reacted with Bradford coomassie dye (Protein Assay Dye Reagent Concentrate, Bio-rad) for 10 minutes and absorbance level was compared with BSA standard curve.

Protein solutions were mixed with β -mercaptoethanol ($\text{HSCH}_2\text{CH}_2\text{OH}$, 98%, Aldrich) and loading buffer (Laemmli Sample Buffer, Bio-rad) to linearize proteins and to impart a negative charge on them, respectively. We used PBS to control the concentration of the protein and the ratio between protein solution: β -mercaptoethanol:loading buffer was 1:0.05:0.95. The mixtures were heat treated at 95 °C for 10 minutes and immediately cooled on the ice.

To conduct electrophoresis, the samples were loaded in the 10% polyacrylamide gel with the reference marker (ProSieve Color Protein Markers, Lonza). Proteins were separated in the condition of 100 V for 90 minutes. Then, we transferred protein from the polyacrylamide gel to the nitrocellulose transfer membrane (Protran, Whatman) by transfer procedure with condition of 80 V for 50 minutes. The device was kept in ice water to cool down the generated heat during electrophoresis procedure. We used Ponceau S (Sigma) to confirm protein separation on the membrane.

Blocking process was proceed in the 5% skim milk (Difco, Becton, Dkckinson and Company) diluted in TBST buffer (TBS with Tween 20, Biosesang) for overnight at 4 °C. Each of 1st antibody diluted with optimized concentration in 1% BSA solution (Bovine Serum Albumin, BovaStar, Bovagen) as shown in Table 3.3 was attached on the protein by shaking at 20 rpm for 4 hours at 4 °C. Then, 2 µg of 2nd antibody (Anti-Rabbit IgG (whole molecule)–Peroxidase antibody produced in goat, Sigma) diluted in 20 mL of 5% skim milk was linked with 1st antibody by shaking at 20 rpm for 1 hour at 4 °C. Between steps, membranes were washed with TBST by shaking at 80 rpm for 10 minutes, for 3 times.

1 st antibody	Symbol	Dilution ratio	Reported Band position
Glyceraldehyde 3-phosphate dehydrogenase (Sigma G9545)	<i>GAPDH</i>	1 µg/mL	36 kDa
Alkaline Phosphatase (Sigma A5968)	<i>AP</i>	5 µg/mL	39 kDa
Bone morphogenetic protein (Sigma SAB1411278)	<i>BMP</i>	1 µg/mL	44 kDa
Osteopontin (Sigma O7264)	<i>OPN</i>	1 µg/mL	50 kDa
Runt-related transcription factor 2 (Sigma R6282)	<i>RUNX</i>	2 µg/mL	55 kDa
Secreted protein acidic and rich in cysteine (Sigma HPA002989)	<i>SPARC</i>	1 µg/mL	32~49 kDa

Table 3.3 List of 1st antibodies used for western blot

To develop membrane into film, membranes were soaked in ECL (Enhanced chemiluminescence, Amersham ECL Prime Western Blotting Detection Reagent, GE Healthaare) for about 1 minute. Then membranes were placed between transparent films. The light was turned off to build darkroom condition, and X-ray sensitive films (Medical X-ray film blue,

AGFA HealthCare) were overlapped with the membranes. After sufficient time, X-ray sensitive films were soaked into developer and fixer. When the films were completely dry, protein bands were scanned into image file.

Osteoclast resorption on whitlockite scaffold

Human osteoclast cells (Lonza) were seeded on the surface of the WH, HAP and TCP scaffold with osteoclast precursor basal medium (Lonza) with FBS, L-glutamine, penicillin, streptomycin, M-CSF and soluble RANK ligand. Samples were kept in CO₂ incubator for 1 month while each medium were exchanged for every 3 days. Differentiation into mature osteoclasts was confirmed by observation of the cells with multiple nuclei from the transmission mode of optical microscope. After 1 month, each scaffold was gently washed with PBS. Lacunae formed on the surface of each sample by resorption activity of osteoclast were observed by FESEM.

Cell proliferation test on AMCD-HAP

To observe the growth of human osteoblasts on HAP surfaces exposed to air, blocks of HAP were prepared as described above. AMCD-HAP pellets were compared with nonporous HAP pellets as controls. After sintering, the HAP pellets were washed with acetone and distilled water, sterilized at 130 °C for 20 minutes and dried under UV irradiation. A sterilized pellet was placed upright in a plastic tube, forming a reservoir for the Lonza osteoblast basal medium containing fetal bovine serum (FBS), ascorbic acid and GA-1000. Lonza Clonetics human osteoblasts were seeded on the top surface, which measured 7 mm × 2 mm, at a density of 1×10^5

cells/ml. The sample was carefully placed in a water-jacketed incubator maintained at 37 °C and 5% CO₂. After 1 day for seeding, the medium was partially removed to a level approximately 1 cm below the top surface of the pellet. After 1 week, the pellet was fixed for 10 minutes with 3.7% formaldehyde diluted in PBS. The cells were permeabilized with 0.2% triton X-100 diluted in PBS for 10 minutes. After each step, the samples were washed with PBS (Cellgro, Mediatech. Inc). The actin cytoskeleton network was stained with phalloidin (Phalloidin, fluorescein isothiocyanate labeled, Sigma) for 1 hour and nuclei were stained with DAPI (4',6-Diamidino-2-phenylindole dihydrochloride, Sigma) for 5 minutes. The AMCD-HAP pellet was mounted with fluoromount (Aqueous Mounting Medium, Sigma) and observed by fluorescence microscopy with appropriate excitation and barrier filters.

Cell activity test on AMCD-HAP

Real time PCR was performed with Rotor gene Q (Qiagen, Santa Clarita, CA) with the Rotor gene SYBR green PCR kit. RNA was extracted from cells using a RNA extraction reagent (RNAiso Plus, Takara), and first strand cDNA was synthesized by using a QuantiTect reverse transcription kit (Qiagen). The initial activation step for PCR was 3 minutes at 95 °C. Denaturation and combined annealing extension cycling proceeded at 95 °C for 3 seconds and 60 °C for 10 seconds, respectively. Each sample was subjected to analysis in triplicate. The numbers of samples used for AMCD-HAP and for the control nonporous HAP were both n = 7. The relative quantities of cDNA were calculated using the ΔC_T method. Primers used for

PCR were purchased from QuantiTect Primer Assay (Qiagen), as shown in Table 3.2.

Bacteria proliferation test on AMCD-HAP

Synechococcus elongatus Nägeli (ATCC 33912), were grown on top of AMCD-HAP surface for 10 days where the bacteria are dependent on only nanochannel capillarity for exchange of nutrients. For this experiment, cyanobacteria cultures at the log phase of growth ($OD_{730} = 0.7$) were collected and seeded on the top surface of the AMCD-HAP pellet. The container was sealed tightly to retain humidity, and maintained in an incubator at 30 °C under 2000 lux light. During the culture period of 10 days, the pellets were partially immersed in BG-11, supplemented with 10 mM of HEPES medium, yet the top of the pellet was > 1 cm above the meniscus of the media. After 10 days of culture, survived bacteria were observed by optical microscopy.

Part I. Compositional control at nanoscale for bone implant

Chapter 4. Synthesis of whitlockite nanoparticles in physiologically relevant condition of ternary Ca(OH)₂-Mg(OH)₂-H₃PO₄ system

4.1 Introduction

Whitlockite (WH: Ca₁₈Mg₂(HPO₄)₂(PO₄)₁₂) is one of the main components of hard tissue in living creatures;^{1,2,15-18} however, currently, very little is known about WH in terms of its mechanism of formation or contribution in our body. The basic reason for this mystery is that detecting WH in our body is difficult because it exists locally only over a short range. Another reason is that synthesizing a pure phase of WH in an aqueous-based physiological system is also difficult. Thus, despite the significant amount of WH in our body, the related field has encountered difficulties in investigations. For example, the biologically existing WH has never been implemented in a clinical trial, whereas the synthetic analog tricalcium phosphate (TCP, Ca₃(PO₄)₂) has been widely used in implants and cell-culturing scaffolds.

WH is a biologically important phase in bone but is difficult to synthesize, most likely because it is thermodynamically stable over a narrow region. It has been long hypothesized that WH can be formed in slight preference to the well-known intermediate dicalcium phosphate dehydrate (DCPD: $\text{CaHPO}_4 \cdot 2\text{H}_2\text{O}$) or defective hydroxyapatite (DHA: $\text{Ca}_9(\text{HPO}_4)_6(\text{PO}_4)_5(\text{OH})$) only between pH 7 and pH 8 but transforms into HAP, which is the most stable calcium phosphate crystal above pH 4.2.¹⁶² This long-conceived prediction is based on the estimation of the ion activity product from a compositional analysis of the precipitates. However, only a few studies have been conducted to further understand the formation mechanism and to identify the stabilizing conditions of WH. The experimental difficulty is mainly due to the existence of too many intermediate phases, including DCPD, octacalcium phosphate (OCP: $\text{Ca}_8\text{H}_2(\text{PO}_4)_6 \cdot 5\text{H}_2\text{O}$) and dicalcium phosphate anhydrous (DCPA: CaHPO_4), which eventually transform into HAP near pH 7.

Previously, there have been only limited reports about obtaining the WH phase from aqueous solutions.^{1,2,110,117,163} Rowles simultaneously mixed CaCl_2 , MgCl_2 and Na_2HPO_4 in water at 100 °C to prepare WH.¹⁶⁴ WH has also been prepared by the dropwise addition of a solution containing Ca^{2+} and Mg^{2+} ions into a phosphate solution.^{117,165} However, both methods suffered from the formation of other heterogeneous phases, such as HAP and various amorphous secondary phases, which affected the overall crystallinity. WH has also been prepared by Rogez et al. using $\text{Ca}(\text{NO}_3)_2$, $\text{Mg}(\text{NO}_3)_2$ and $(\text{NH}_4)_2\text{HPO}_4$.¹⁶³ In this chapter, we designed and presented a simple synthesis of WH in a ternary $\text{Ca}(\text{OH})_2$ - $\text{Mg}(\text{OH})_2$ - H_3PO_4 system, without any

other secondary ion or buffer effect. The entire process was conducted in an aqueous system and was always maintained below 100 °C.

4.2 Synthesis of whitlockite nanoparticles in ternary $\text{Ca}(\text{OH})_2\text{-Mg}(\text{OH})_2\text{-H}_3\text{PO}_4$ system

To determine the appropriate synthesis conditions for WH, we organized a ternary diagram with the possible precipitants resulting from $\text{Ca}(\text{OH})_2$, $\text{Mg}(\text{OH})_2$ and H_3PO_4 at 80 °C, as illustrated in Figure 4.1. In the $\text{Ca}(\text{OH})_2\text{-H}_3\text{PO}_4$ binary system, HAP, DCPA and MCPM are precipitated based on their composition ratio in the chemical formula. In the $\text{Mg}(\text{OH})_2\text{-H}_3\text{PO}_4$ binary system, MP, MMP and TMP can be synthesized following their chemical formula. However, we observed that WH could not be precipitated under the stoichiometric conditions of its product (★ in Figure 4.1). Instead, the majority product formed under these conditions was HAP, as HAP is the most thermodynamically stable phase near neutral pH¹⁶² and is a non-stoichiometric compound that can adopt a wide range of atomic disorders due to its flexible framework.¹⁶⁶ Therefore, the location of the theoretical composition of WH is in a region with a strong preference for HAP precipitation, and thus, synthesizing WH in the $\text{Ca}(\text{OH})_2\text{-Mg}(\text{OH})_2\text{-H}_3\text{PO}_4$ ternary system appeared difficult.

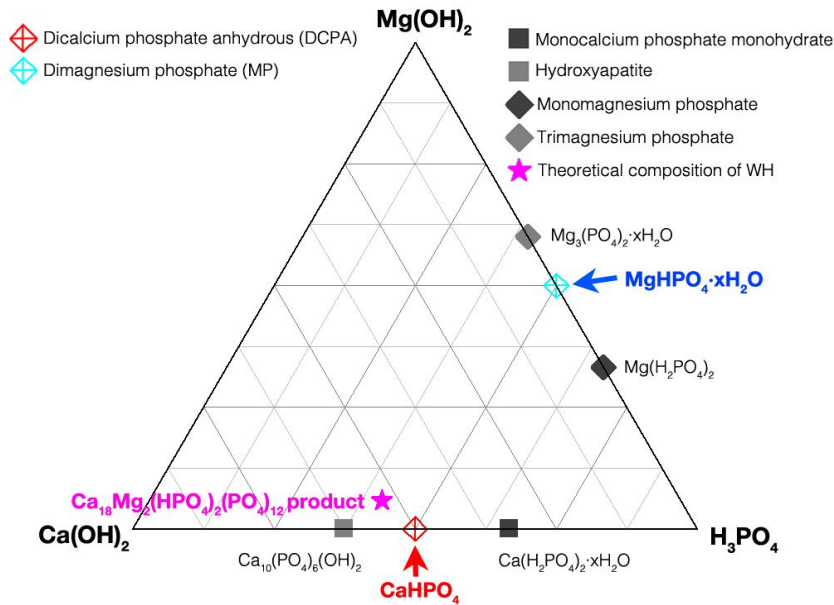


Figure 4.1 Ternary diagram of well-known precipitants in a Ca(OH)_2 - Mg(OH)_2 - H_3PO_4 aqueous system at 80°C .

To determine the precipitation conditions for WH and to learn from the previously made TCP, we first analyzed how the phase stability of TCP changes depending on the Mg content and pH. We learned from many previous studies that Mg substitution in TCP (TCMP) stabilizes the phase at low pH compared with pure TCP.^{1,167} A detailed example of the activity diagram for the Ca(OH)_2 - Mg(OH)_2 - H_3PO_4 system at 25°C indicated that TCMP drastically decreased its solubility compared with TCP and even more than HAP. However, Mg^{2+} is known to inhibit HAP^{1,164,168} and other kinetically favored intermediate phases of calcium phosphate compounds, such as DCPD,^{1,169} DCPA^{1,170} and OCP.^{1,171} This fact could suggest a

hypothesis that WH could be stable under acidic conditions. Because the atomic arrangement in the unit cell is similar for WH and TCP, we hypothesized that the substitution of Mg^{2+} could result in a similar contribution to its stability under acidic conditions.

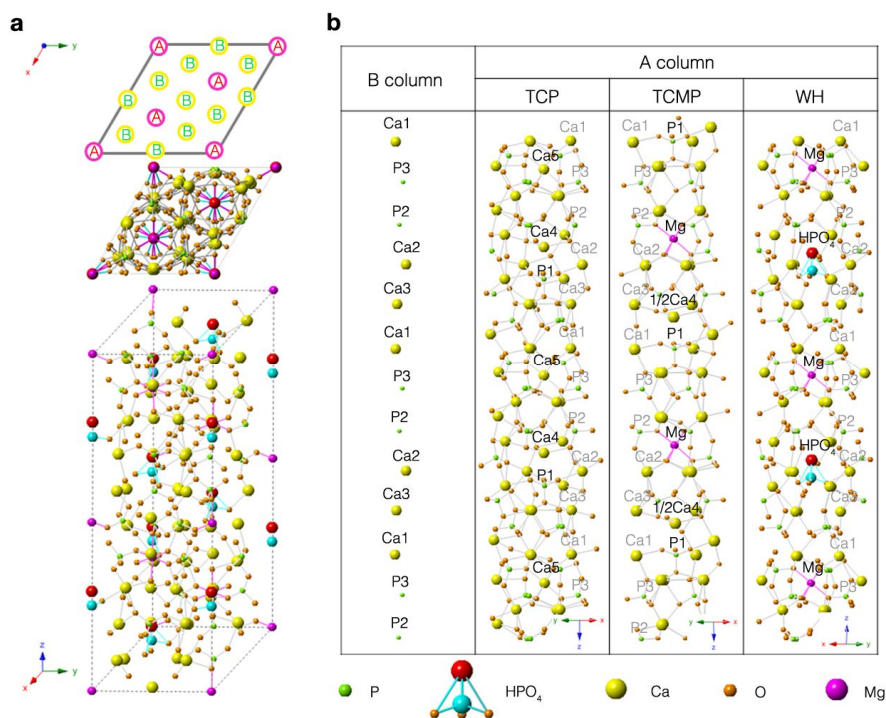


Figure 4.2 Crystal structure of whitlockite (WH) compare to tricalcium phosphate (TCP) and magnesium-substituted tricalcium phosphate (TCMP). **a**, Unit cell of WH and its x-y plane view from the z-axis direction. Looking down from the z-axis, the A and B columns are periodically arranged in the unit cell of WH. **b**, A comparison of the differences in the A column among TCP, TCMP and WH; all three compounds have the same atomic

arrangement in the B column. The variations in the A column were induced by the incorporation of Mg^{2+} and HPO_4^{2-} . The sizes of main atoms have been exaggerated for easier comparison.

As illustrated in Figure 4.2, TCP and TCMP are very closely related to WH. We show the basic unit cell structure of WH with lattice parameters $a = 10.35 \text{ \AA}$ and $c = 37.085 \text{ \AA}$ in Figure 4.2a. In the z-axis direction, we observe that WH is composed of two types of columns that are periodically arrayed. In each column, Ca^{2+} ions and PO_4^{3-} ions are regularly arrayed. The B column remains the same in TCP and WH structure compounds, while the differences usually occur in the A column. For example, when Mg^{2+} is incorporated in the TCP structure and produces the TCMP structure, Mg^{2+} substitutes into the previous Ca5 position, as illustrated in Figure 4.2b. After the Ca5 position is fully substituted with Mg^{2+} , the Ca4 position can be also substituted with Mg^{2+} . For the WH compound, HPO_4^{2-} is also incorporated together with Mg^{2+} into the A column and forms a crystal structure that is stable enough to be precipitated without requiring a high temperature sintering process. In addition, TCP and WH also have similar XRD patterns based on rhombohedral crystal structures, and their ratios between cations and anions are similar. Thus, several researchers have previously been confused in distinguishing TCP and WH, and have used these terms interchangeably.

As further rationale to design the experimental conditions, we paid attention to the fact that WH contains HPO_4^{2-} together with PO_4^{3-} in its unit

cell, which is a notable difference from HAP, which only contains PO_4^{3-} in its theoretical chemical formula. This difference could provide additional evidence that WH can be precipitated at low pH.

Therefore, for our systematic approach, we selected the binary system of CaHPO_4 and MgHPO_4 . Both compounds contain HPO_4^{2-} as an anion and are known to be precipitated more favorably than HAP. Along the compositional line of 50 at% H_3PO_4 , the atomic percentage of Mg in the total cation (Mg+Ca) was varied from 0 to 20, 40, 70 and 100%. The (Mg+Ca): PO_4 ratio was fixed at 1:1, and only the Mg:Ca ratio was varied. $\text{Ca}(\text{OH})_2$ powder and $\text{Mg}(\text{OH})_2$ powder were dissolved at the various ratios in 500 mL aqueous solution at 80 °C. The total mole concentration of the cation was fixed at 0.5 M. Then, 500 mL of 0.5 M H_3PO_4 was added dropwise to the 500 mL of $\text{Ca}(\text{OH})_2$ and $\text{Mg}(\text{OH})_2$ solution at a speed of 12.5 mL/min. Thus, the final ratio of Mg:Ca:P was equal to $x:(0.5-x):0.5$ ($x = 0, 0.1, 0.2, 0.35, 0.5$). After 24 hours of incubation under vigorous stirring, the precipitants were collected with a filter press and dried using a lyophilizer for further characterization.

XRD analysis was performed to identify the crystal structure of the precipitants. At $x = 0$, pure CaHPO_4 was precipitated without any minor phase. Notably, at $x = 0.1$, a minor peak that corresponded to WH started to be observed in addition to the major CaHPO_4 peaks. At $x = 0.2$, the CaHPO_4 peak disappeared and instead the MgHPO_4 peak appeared along with the WH peak. As x increase to 0.3 and 0.4, the intensity of MgHPO_4 increased and that of WH decreased, indicating that the ratio of WH in the precipitants decreased. This result was clearly demonstrated that the WH could

precipitate in an acidic environment with the incorporation of Mg^{2+} , which prevented HAP precipitation.

To better understand the mechanism and to obtain pure WH, we focused on the region between $x = 0.2$ and $x = 0.4$. The results indicated that the pure WH phase precipitated when $x = 0.13$, between the WH+DCPA heterogeneous region ($x < 0.125$) and the WH+MP heterogeneous region ($x > 0.135$). According to inductively coupled plasma (ICP) analysis, well-synthesized WH was a stoichiometric compound with a ratio of Ca:Mg:P = $1.27 \pm 0.06:0.14 \pm 0.02:1$ that match with the theoretical ratio (1.28:0.14:1).

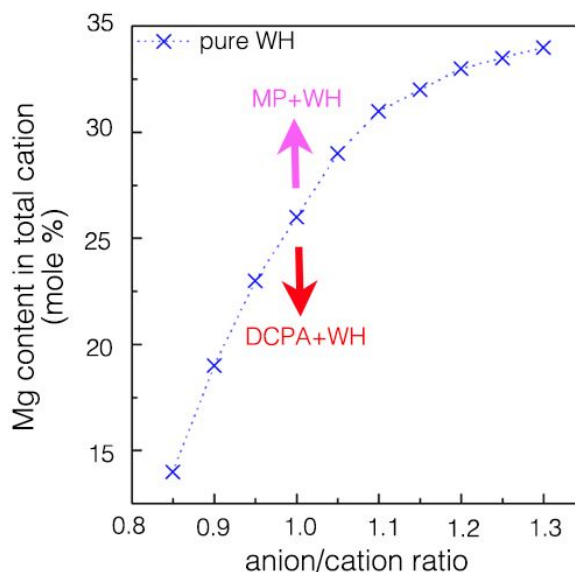


Figure 4.3 Synthetic conditions of pure whitlockite (WH) from $Ca(OH)_2$ -

Mg(OH)₂-H₃PO₄ system, which are plotted as blue cross symbols, with the x-axis being the ratio of the anion (P) to cations (Ca+Mg) in mole% and the y-axis being the content of Mg in the total cation (Ca+Mg), also in mole%.

To locate the overall precipitation region of WH, we investigated an optimized ratio between Ca(OH)₂, Mg(OH)₂ and H₃PO₄, starting from the aforementioned location of Ca(OH)₂:Mg(OH)₂:H₃PO₄ = 37%:13%:50% (in mole%). Based on the experimental results, we marked all the possible synthesis regions of pure WH in Figure 4.3 and also presented in the ternary diagram of Figure 4.4. Other than these conditions, impurities, such as DCPA or MP, can also be precipitated (Figure 4.5). To be more specific, WH was produced in more acidic pH conditions with excess Mg²⁺ ions present in the environment. Because MP ($K'_{\text{MgHPO}_4} = 0.0011 \text{ M}$ at 25 °C) has a lower thermodynamic dissociation constant than DCPA ($K'_{\text{CaHPO}_4} = 0.0020 \text{ M}$ at 25 °C),¹⁷² we hypothesize that Mg²⁺ combines with HPO₄²⁻ more competitively than Ca²⁺ and constructs the A column of WH. Thus, a greater amount of Mg²⁺ may be required to combine with HPO₄²⁻ and inhibit calcium phosphate compound nucleation when the anion-to-cation ratio is higher. When this balance between cations and anions is not maintained, other secondary phases, such as DCPA or MP, are immediately produced and form the heterogeneous region.

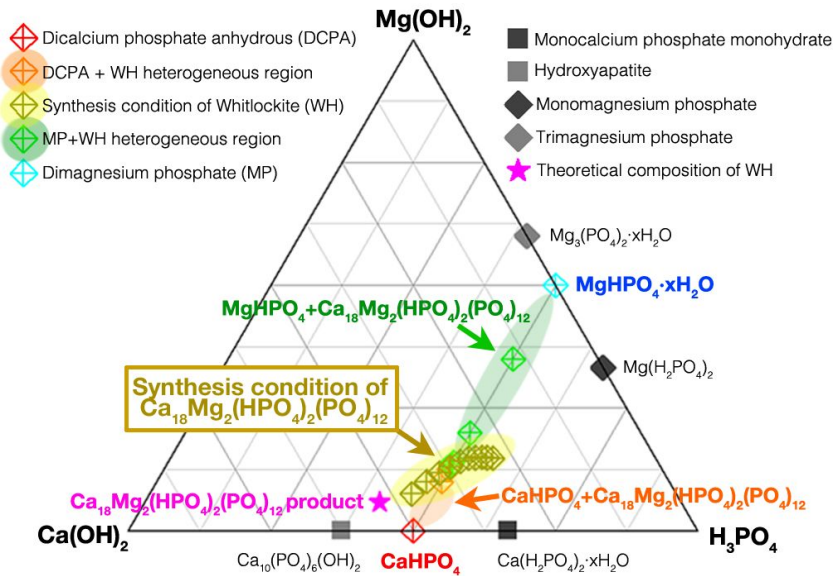


Figure 4.4 Ternary diagram of precipitants in a $\text{Ca(OH)}_2\text{-Mg(OH)}_2\text{-H}_3\text{PO}_4$ aqueous system after 24 hours of aging at 80 °C. The newly discovered synthesis conditions of whitlockite examined in this work (gold diamond: \diamond) and its theoretical composition (magenta star: \star) are indicated. Other closely located calcium phosphate precipitants and magnesium phosphate precipitants are also indicated.

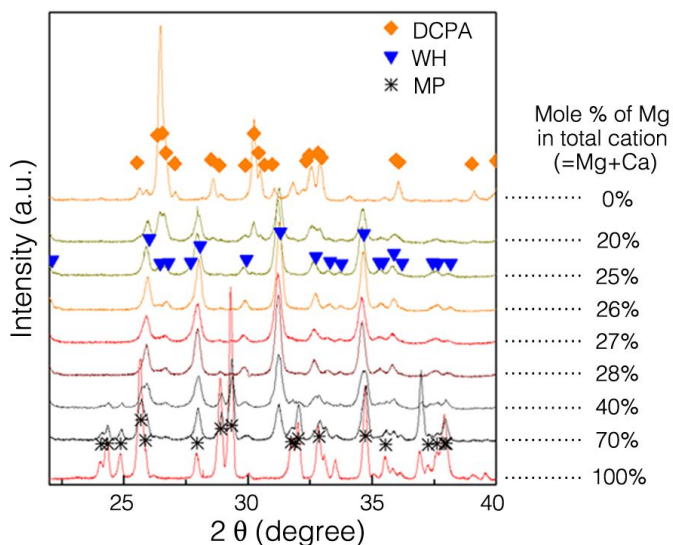


Figure 4.5 XRD analysis of precipitants formed in the binary system of dicalcium phosphate anhydrous (DCPA: CaHPO_4) and dimagnesium phosphate (MP: MgHPO_4), with different Mg contents in total cation (Ca+Mg). The ratio between the anion (P) to total cations was fixed at 1:1. Pure whitlockite (WH) was formed when the ratio of Mg in the total cation was 26%. When the Mg ratio in the total cation exceeded 26%, MP was also precipitated with WH. However, when the Mg ratio in total cation was less than 26%, DCPA was precipitated along with WH. In addition, pure phases of either MP or DCPA were formed only when Mg (Mg = 100%) or Ca (Mg = 0%) existed in the total cation, respectively.

4.3 Characterization of whitlockite nanoparticle

In Figure 4.6, XRD analysis of our synthesized WH demonstrated that a pure WH phase was formed. We heat-treated the WH at temperatures as high as 1450 °C to verify its high purity. If secondary phases exist in the amorphous state, high temperature heat treatment can crystallize these phases and make them detectable by XRD. However, no secondary phase appeared after heat treatment at 1450 °C. Therefore, we confirmed that WH was precipitated in a completely homogeneous phase. There was also no indication of a phase change in XRD pattern during heat treatment until WH transformed into the liquid phase at approximately 1600 °C.

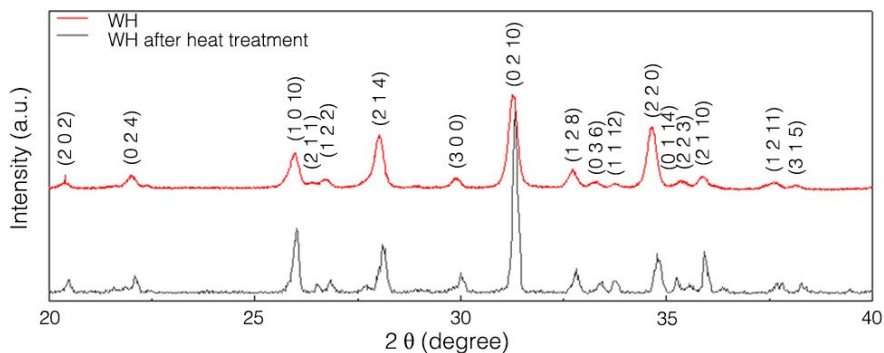


Figure 4.6 XRD patterns showing the pure phase of the synthesized whitlockite (WH: red line). WH maintained its pure phase even after being heat-treated at 1450 °C for 2 hours (gray line).

In addition, as illustrated in Figures 4.7a and 4.7b, our synthesized WH particles were homogeneous, with rhombohedral shapes and sizes of approximately 50 nm. The interplanar distance of the WH nanoparticles was measured to be 8.067 Å by high-resolution transmission electron microscopy (HRTEM) (bottom right inset of Figure 4.7b), which corresponded well to the d-spacing value of the WH (0 1 2) plane (JCDPS No. 70-2064).

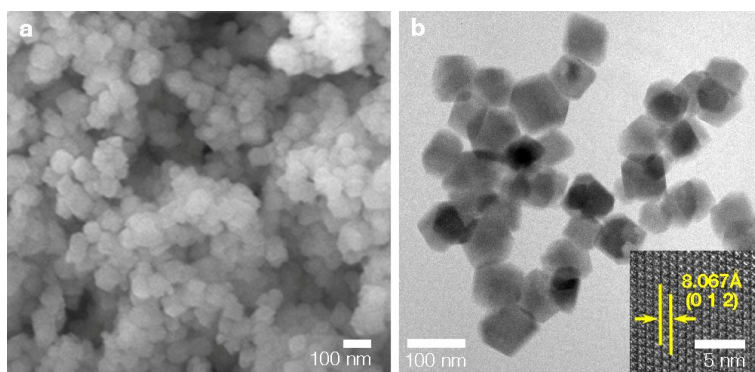


Figure 4.7 Homogeneously synthesized whitlockite (WH) nanoparticles. **a**, FESEM image of homogeneously formed WH nanoparticles. **b**, High-resolution TEM image of rhombohedral shape of WH nanoparticles with approximately 50 nm size. As shown in the bottom right inset, the d-spacing value was measured to be 8.067 Å for the WH nanoparticles, which corresponded to the (0 1 2) plane of WH.

4.4 Distinction between whitlockite and β -tricalcium phosphate

It is true that TCP and WH are closely related; however, we can clearly distinguish them by the stable region of their phases and the existence of HPO_4^{2-} in their structure. TCP is a high-temperature phase that cannot be produced in our 37 °C bodies. In addition, TCP cannot avoid transforming into a heterogeneous bulk state after heat treatment. In contrast, WH exists in biological systems and can also be synthesized as nanoparticles below the boiling temperature of water. In addition, we can easily distinguish WH from TCP by detecting the HPO_4^{2-} bond using FT-IR. During heat treatment, a decrease in the weight of WH can also be observed due to the dehydration of HPO_4^{2-} in its structure. Then, notably, WH can transform into the TCMP structure after losing its HPO_4^{2-} group at high temperature.^{1,145,148,150}

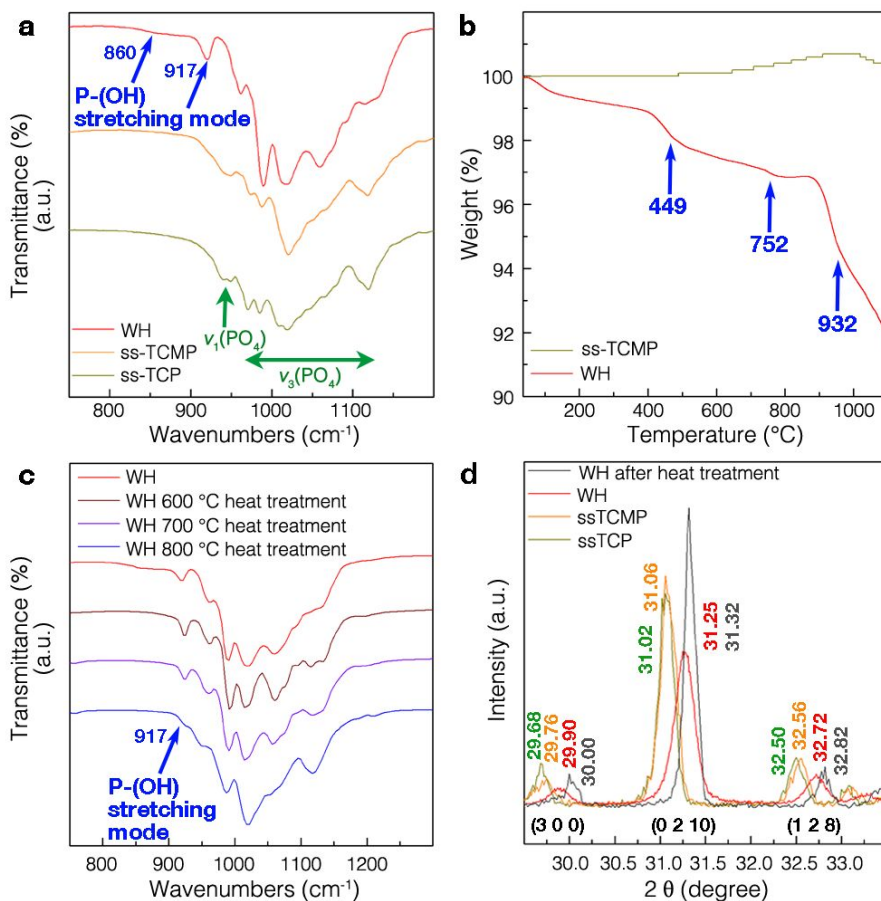


Figure 4.8 Distinction of whitlockite (WH) from tricalcium phosphate (TCP) compounds based on HPO_4^{2-} group in its chemical structure. **a**, FT-IR analysis result of our synthesized WH (red line), revealing the existence of P-O-H bonds from the HPO_4^{2-} group in its structure. However, TCP (ss-TCP: green line) and magnesium substituted tricalcium phosphate (ss-TCMP: yellow line) only contained bonds from PO_4^{3-} without any P-O-H bonds. **b**, TGA analysis of WH (red line) revealing a decrease in weight due to the dehydration of the HPO_4^{2-} group. However, no weight decrease was observed in ss-TCMP (green line). **c**, FT-IR analysis result demonstrating

that the P-O-H bond in WH gradually decreased with increases in the temperature of the heat treatment. **d**, XRD analysis of WH (red line), WH after heat treatment at 1450 °C (gray line), ss-TCMP (yellow line) and ss-TCP (green line), demonstrating that the incorporation of Mg^{2+} and HPO_4^{2-} induced shifts of the (3 0 0), (0 2 10) and (1 2 8) peaks toward higher angular positions.

To distinguish our synthesized WH from the TCP phase, we provided evidence of the existence of HPO_4^{2-} in the WH structure. As shown in Figure 4.8a, Fourier transform infrared spectroscopy (FT-IR) analysis demonstrated that P-O-H bonds were only present in the WH compound formed using the precipitation method, while only P-O related bonds were present in the ss-TCP and ss-WH prepared using the solid-state method. In addition, we observed that this P-O-H group in the WH structure could be lost during heat treatment by thermogravimetric (TGA) analysis, as shown in Figure 4.8b. While the initial decrease in the WH weight is caused by the evaporation of water molecules, the subsequent peaks at approximately 449 °C and 752 °C suggest the transformation of HPO_4^{2-} into $P_2O_7^{4-}$ and PO_4^{3-} .^{2,149} The rapid decrease in the WH weight at approximately 932 °C is also a unique phenomenon of WH during heat treatment.¹⁴⁵ After these dehydration processes, WH loses its HPO_4^{2-} group and transforms into the TCP structure.^{1,145,148,150} In contrast, there was no weight change in ss-TCP during TGA analysis, and a rather slight weight increase occurred due to N_2 gas adsorption on the surface of the particles. In Figure 4.8c, we compare the FT-IR results of the WH compounds after being heat treated at different

temperatures, and we confirmed that the P-O-H peak disappeared above 800 °C but remained until 700 °C. Therefore, WH can maintain its structural properties below this temperature. In Figure 4.8d, we carefully compare the XRD peak positions of various TCP, TCMP and WH samples. As the substitution ratio of Mg^{2+} increased from TCP to TCMP (Ca:Mg \approx 20:1 in mole%) to WH (Ca:Mg \approx 9:1 in mole%), the lattices contracted and the XRD peaks shifted toward higher angular positions according to Bragg's law. Similarly, when HPO_4^{2-} was lost in WH by heat treatment at 1450 °C, the peaks shifted again to higher angular positions. All these analysis results clearly demonstrate that WH could be distinguished from TCP and TCMP.

4.5 Stability of whitlockite

We also observed stability of WH in various pH regions. The precipitated WH was neutral in distilled water and maintained its homogeneous phase even after aging for 15 days in a 90 °C alkaline environment (0.01 g/mL WH in 100 mL of di-sodium hydrogen phosphate/sodium hydroxide buffer, pH 12), as demonstrated in Figure 4.9.

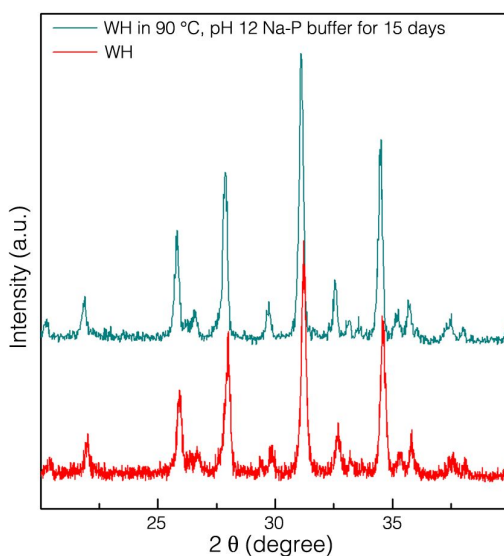


Figure 4.9 Stability test of whitlockite (WH: $\text{Ca}_{18}\text{Mg}_2(\text{HPO}_4)_2(\text{PO}_4)_{12}$); after aging in a pH 12 di-sodium hydrogen phosphate/sodium hydroxide buffer solution at 90 °C of for 15 days, WH maintained its pure state phase.

In addition, we compared the remaining amounts of WH and HAP after aging 24 hours in H_3PO_4 aqueous solutions (0.01 g/mL WH and HAP in 100 mL H_3PO_4 aqueous solution from pH 2.5 to pH 5) at room temperature. Notably, as demonstrated in Figure 4.10, when the pH decreased from 4.2 to 4.0, the remaining amounts of WH and HAP decreased from 0.804 g and 0.89 g to 0.702 g and 0.32 g, respectively. These data suggest that WH has higher stability than HAP below pH 4.2. An interesting future issue would be to investigate the correlation between the formation of WH and the acidic environment in our body.^{3,173-175} Local areas

in vivo are often exposed to acidic environments. For example, old and weak parts of the bone are continuously dissolved by acidic chemicals secreted by osteoclast cells, which are estimated to have pH values of 3~4.5.¹⁷³⁻¹⁷⁵

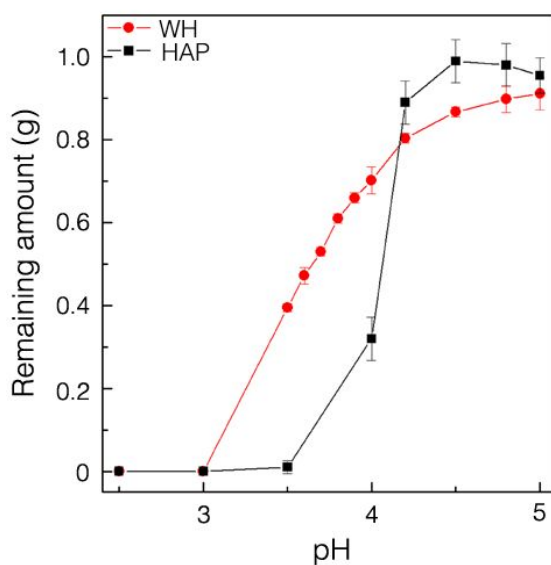


Figure 4.10 Solubility test of whitlockite (WH) and hydroxyapatite (HAP) in the acidic pH region. The remaining amounts of WH and HAP after 24 hours of aging in 100 mL of aqueous solution were compared. The initial amount of each powder was 1 g, and the pH was titrated using H_3PO_4 at room temperature.

4.6 Summary

The approach presented here for the synthesis of pure WH nanoparticles has scientific importance because of the discovery of new precipitation conditions in the ternary $\text{Ca}(\text{OH})_2\text{-Mg}(\text{OH})_2\text{-H}_3\text{PO}_4$ system and offers technological potential for further applications. Our results demonstrated that pure WH can precipitate under acidic pH conditions. Excess Mg^{2+} in the system also impeded the formation of HAP and other kinetically favored calcium phosphate intermediate phases. We expect that this study will contribute to the understanding of the precipitation mechanism of calcium phosphate compounds in physiological systems and become a platform for synthesizing technologically important bio-ceramics.

Chapter 5. Phase transformation from hydroxyapatite to whitlockite: interplay of two major biominerals in bone.

5.1 Introduction

Whitlockite (WH: $\text{Ca}_{18}\text{Mg}_2(\text{HPO}_4)_2(\text{PO}_4)_{12}$) is found in both terrestrial mineral near volcanic region and sediment, and extraterrestrial rocks from meteorite, Luna and Mars, while it is also the second most abundant mineral in our hard tissue. Interestingly, the ratio of WH was reported to be higher in the younger aged body and the earlier stage of mineralization in the *in vivo* system. These characteristic distributions of WH might possibly reflect the origins and the evolutions of mineral and even that of related organism, yet its formation mechanism still remains unclear. Despite our body system maintains pH of 7.4 and temperature of 37 °C which is favored condition for the formation of hydroxyapatite (HAP: $\text{Ca}_{10}(\text{PO}_4)_6(\text{OH})_2$), WH is estimated to exist in our bone and dentin with about 20% and 26 to 58% by weight, respectively¹. The higher stability of WH compare to that of HAP under pH 4.2 implicates that WH might be generated from the different mechanism with HAP inside our body system. Revealing the formation mechanism of WH can lead us to comprehend the meaning of the presence of WH in living system with its derived roles and also the nature of bone *per se*. In this respect, we investigated kinetic mechanism of precipitation of WH in physiologically analogous ternary

$\text{Ca(OH)}_2\text{-Mg(OH)}_2\text{-H}_3\text{PO}_4$ aqueous system, while excluding any other effects of buffer or secondary ions. We analyzed occurrence of intermediate phases during the formation of WH with different experiment time and revealed that WH was generated from the former HAP phase depending on the change of the pH of the microscopic environment. In addition, we compared transition of amounts of ions in the precipitant and the surrounding system to determine whether the formation of WH was induced by the minimized atomic movement in the former phase or by the total dissolution and recrystallization process. Our finding indicates that WH in living system can be generated from the HAP under the proper pH condition of the microenvironment, on the basis of the secondary ions such as Mg^{2+} .

5.2 Formation of whitlockite from serial transition of pH in $\text{Ca(OH)}_2\text{-Mg(OH)}_2\text{-H}_3\text{PO}_4$ aqueous system

In order to precipitate WH, we dropwised 500 mL of 0.95 M H_3PO_4 aqueous solution into 500 mL of Ca(OH)_2 and Mg(OH)_2 mixed solution with dosing rate of 12.5 mL/min. The molar concentrations of Ca and Mg were 0.77 M and 0.23 M, respectively. The solutions were vigorously stirred for the sufficient blending. As shown in Figure 5.1, droplets of H_3PO_4 were continuously added into $\text{Ca(OH)}_2\text{-Mg(OH)}_2$ system and pH condition of the system changed dramatically from 11.1 to 3.3.

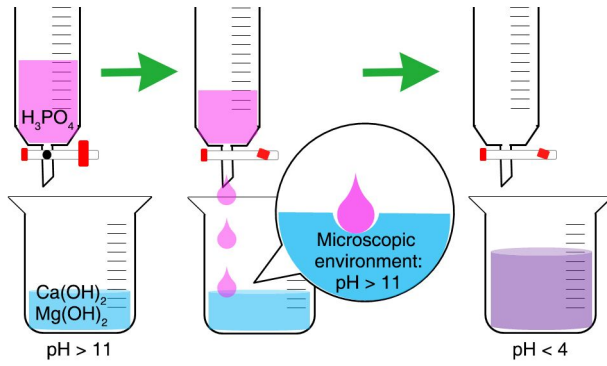


Figure 5.1 Serial pH transition from basic to acidic during formation of whitlockite in Ca(OH)_2 - Mg(OH)_2 - H_3PO_4 system.

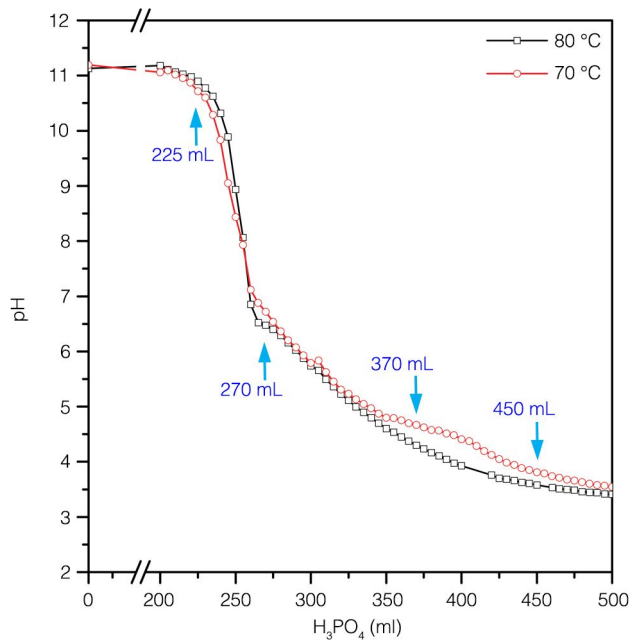


Figure 5.2 pH transition during whitlockite precipitation in Ca(OH)_2 - Mg(OH)_2 - H_3PO_4 system at 70 °C (red circle) and 80 °C (black square).

Interestingly, as shown in Figure 5.2, during the addition of H_3PO_4 droplet into the $\text{Ca}(\text{OH})_2\text{-Mg}(\text{OH})_2$ aqueous solution, pH of the system decreased with different rate of change. Different inclination of decrement of pH during experimental process reflects formation of various intermediate phases. We assumed that, depending on the pH of the surrounding environment, the Ca^{2+} -related phase and Mg^{2+} -related phase alternatively transformed into more stable phase, until both Ca^{2+} and Mg^{2+} incorporated to the final phase of WH. Based on the pH transition region with different rate of change, amount of added H_3PO_4 and experiment time, as shown in Table 5.1, we divided several stages from I to VI. We collected intermediate precipitants from each stage and analyzed their crystal phases to understand the kinetic path of WH.

Stage	pH	Amount of H_3PO_4 (mL)	Aging time (hour)
I	11.1	0	-
II	6.5	270	-
III	4.7	370	-
IV	3.8	450	-
V	3.3	500	5
VI	3.7	500	24

Table 5.1 Stages I~VI classified by pH, amount of H_3PO_4 and experiment time during formation of whitlockite in $\text{Ca}(\text{OH})_2\text{-Mg}(\text{OH})_2\text{-H}_3\text{PO}_4$ aqueous system. Intermediate phases formed at each stage were collected and analyzed.

5.3 Kinetic path of the whitlockite in the ternary $\text{Ca(OH)}_2\text{-Mg(OH)}_2\text{-H}_3\text{PO}_4$ system

After the addition of H_3PO_4 was completed, the pH of the system turned to about 3.3. Because HAP is known to be stable only above 4.2, HAP was dissolved and WH was precipitated in the final acidic environment. After 24 hours of aging time, pH slightly increased to 3.7, which reflected that the ratio of cation to anion in the precipitant became lower and thus the residual HAP transformed into WH. However, depending on the temperature of the synthesis condition, the kinetic paths were differently developed.

In Figure 5.3, XRD patterns of intermediate phases formed during addition of H_3PO_4 in the $\text{Ca(OH)}_2\text{-Mg(OH)}_2$ aqueous solution at 70 °C were shown. At stage I, HAP and Mg(OH)_2 phases were mainly existed in the precipitants. In other words, Ca(OH)_2 reacted with H_3PO_4 and produced HAP while Mg(OH)_2 remained. During stage I and stage II, Ca(OH)_2 was almost consumed and Mg(OH)_2 started to react with H_3PO_4 , because Mg(OH)_2 was less stable than HAP. As a result, at stage III, XRD peak of Mg(OH)_2 disappeared, but instead, XRD peaks of dimagnesium phosphate (MP: $\text{MgHPO}_4 \cdot x\text{H}_2\text{O}$) clearly appeared. Then, as the system became more acidic due to the continuous addition of H_3PO_4 , at stage IV, HAP became unstable and partially turned into dicalcium phosphate dehydrate (DCPD: $\text{CaHPO}_4 \cdot 2\text{H}_2\text{O}$), which is kinetically favored calcium phosphate phase in acidic pH condition.

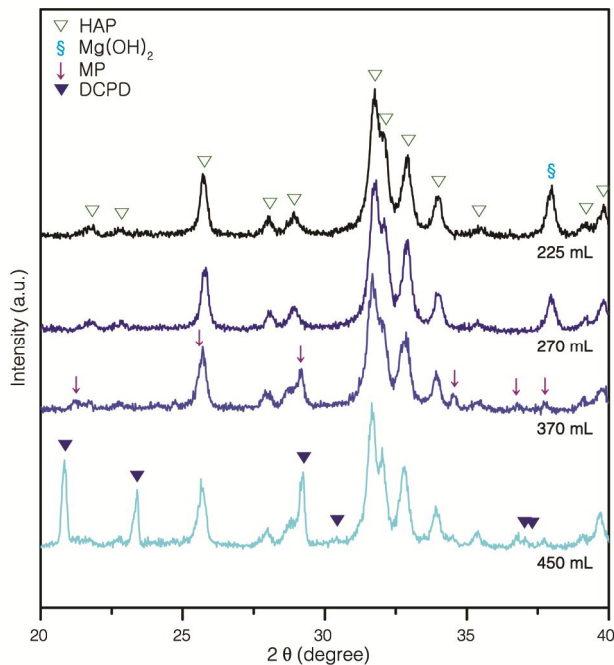


Figure 5.3 XRD analysis of the intermediate phases of whitlockite during addition of H_3PO_4 in the $\text{Ca}(\text{OH})_2$ - $\text{Mg}(\text{OH})_2$ aqueous system at $70\text{ }^\circ\text{C}$.

In Figure 5.4, XRD patterns of the intermediate phases after complete addition of H_3PO_4 in the $\text{Ca}(\text{OH})_2$ - $\text{Mg}(\text{OH})_2$ system were shown according to different aging time at $70\text{ }^\circ\text{C}$. Right after finishing the addition of total amount of H_3PO_4 , the major phases were found to be HAP, DCPD and MP. During aging in the acidic system of pH 3.3, HAP gradually dissolved. In addition, DCPD and MP, which are kinetically favored phases in acidic condition, turned into more stable phase of WH. In Figure 5.4, we can see that at the stage V when aging time was 5 hours, WH phase appeared while peaks of DCPD and MP almost disappeared. Finally, at the stage VI

when aging time was 24 hours, residual HAP was also completely dissolved and only pure phase of WH was observed.

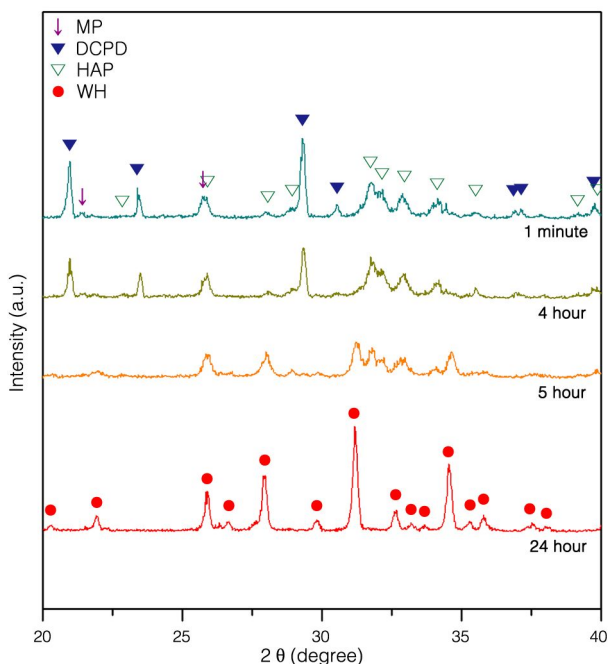


Figure 5.4 XRD analysis of the intermediate phases of whitlockite during aging process in the $\text{Ca}(\text{OH})_2\text{-Mg}(\text{OH})_2\text{-H}_3\text{PO}_4$ system at 70 °C. The aging time was measured from the complete addition of H_3PO_4 in the $\text{Ca}(\text{OH})_2\text{-Mg}(\text{OH})_2$ aqueous solution (0 minute).

When the additional thermal energy was given, the kinetic path of WH became more accelerated with different modality. As shown in Figure 5.2, when the temperature of the synthesis condition increased to 80 °C, there was no discontinuous decrement in pH between stage III and stage IV. When we compare intermediate phases formed during addition of H_3PO_4 and

aging process in Figure 5.5 and Figure 5.6, respectively, we can see that there is no trace of DCPD phase. In acidic condition above 80 °C, dicalcium phosphate anhydrate (DCPA: CaHPO_4) is known to exist as a kinetically favored calcium phosphate phase. However, excess Mg^{2+} in the system might have disturbed the formation of DCPA and thus, almost no DCPA was observed after 1 minute of aging process. Instead, HAP was observed as a dominant phase and even WH was already appearing as a minor phase. After 30 minutes, the peaks belong to the WH became predominant whereas the intensity of the peaks of HAP decreased. Finally, 12 hours later, homogeneous phase of WH was obtained with high crystallinity.

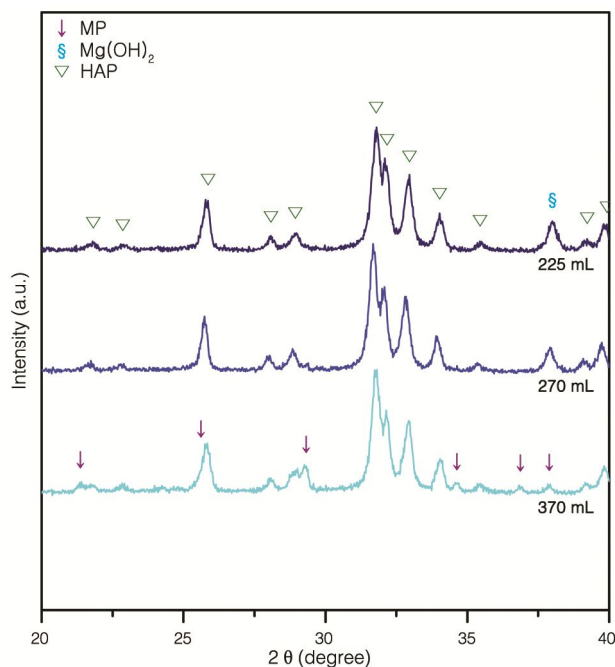


Figure 5.5 XRD analysis of the intermediate phases of whitlockite during addition of H_3PO_4 in the $\text{Ca}(\text{OH})_2$ - $\text{Mg}(\text{OH})_2$ aqueous system at 80 °C.

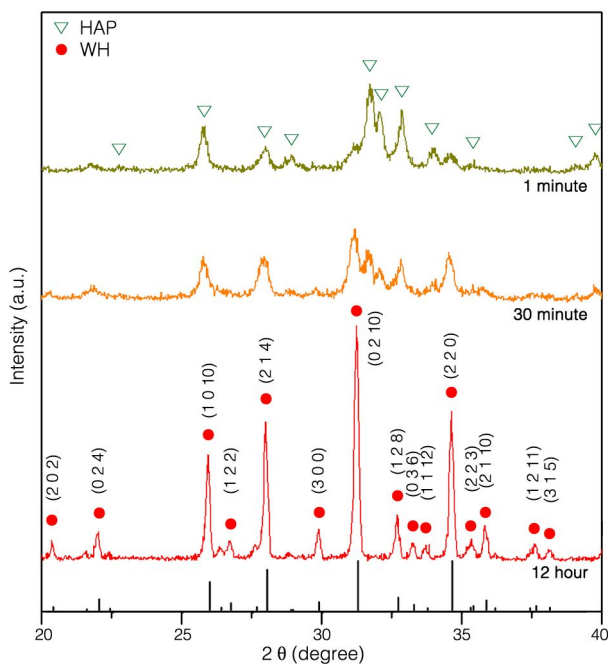


Figure 5.6 XRD analysis of the intermediate phases of whitlockite during aging process in the $\text{Ca(OH)}_2\text{-Mg(OH)}_2\text{-H}_3\text{PO}_4$ system at $80\text{ }^\circ\text{C}$. The aging time was measured after the complete addition of H_3PO_4 in the $\text{Ca(OH)}_2\text{-Mg(OH)}_2$ aqueous solution (0 minute).

The kinetic mechanism during the formation of WH is easily represented in Figure 5.7. At each stage, Ca-related compounds and Mg-related compounds alternatively dissolve and react with newly added phosphoric acid to form more stabilized phase according to surrounding condition. Interestingly, although Ca-related compounds and Mg-related compounds exist separately during the kinetic path, at the final stage, Ca, Mg and P reorganize with each other and form the most stable phase of WH.

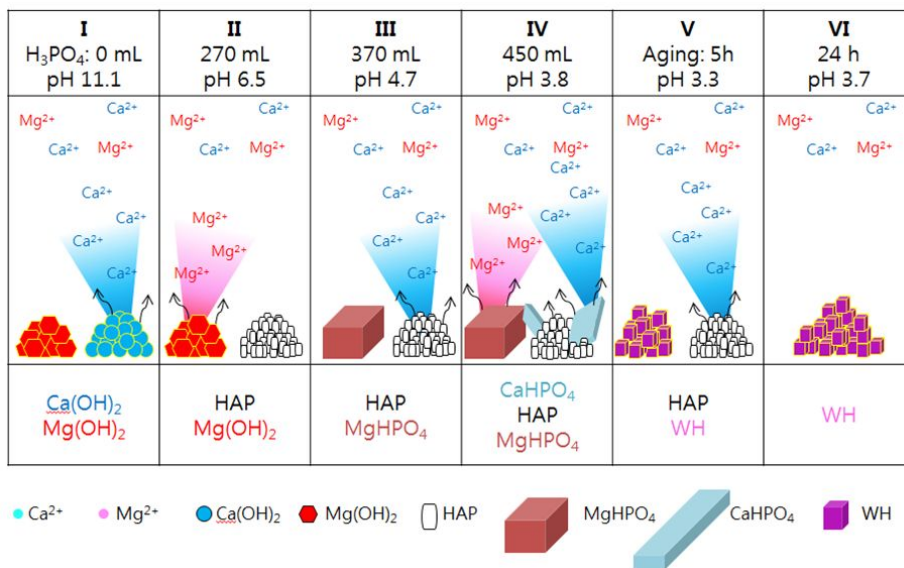


Figure 5.7 Kinetic path of whitlockite at 70 °C in Ca(OH)₂-Mg(OH)₂-H₃PO₄ aqueous system. At each stage, intermediate phase with higher solubility dissolves and releases ions to induce more stabilized phase.

The morphologies of the precipitants collected from the different experiment time also reflect the phase transformation process toward WH. From the FESEM analysis, we observed the precipitants formed in different stages. In Figure 5.8a, at stage II, we can see that Ca(OH)₂ particles transformed into rice shaped HAP nanoparticles with about 80 nm length while Mg(OH)₂ particles were still remaining. These Mg(OH)₂ particles had polygonal platelet morphology in nanometer scale. Then at stage III, in Figure 5.8b, Mg(OH)₂ particles were dissolved and transformed into micrometer scale cuboid form, which was MP. On the surface of MP, we can see the existence of rice shaped HAP nanoparticles (Figure 5.8c). When the pH of the system decreased to acidic state in stage IV, large platelet shape of

DCPD appeared whereas HAP nanoparticles remained (Figure 5.8d-e). When the temperature was higher, most of the particles had rice shape in nanometer scale, which indicates that HAP was the major phase. After total amount of H_3PO_4 was added, during the aging process, HAP gradually dissolved in acidic condition and rhombohedral shape of WH began to appear. In Figure 5.8g, we marked rhombohedral WH nanoparticles with green arrows which exist between remaining HAP nanoparticles. After 24 hours, only rhombohedral particles were found in the precipitant, which confirmed that homogeneous phase of WH was obtained (Figure 5.8h). When this reaction was proceeded at lower temperature, 65 °C, WH precipitated after 2 weeks and had larger size than that formed at higher temperature (Figure 5.8i).

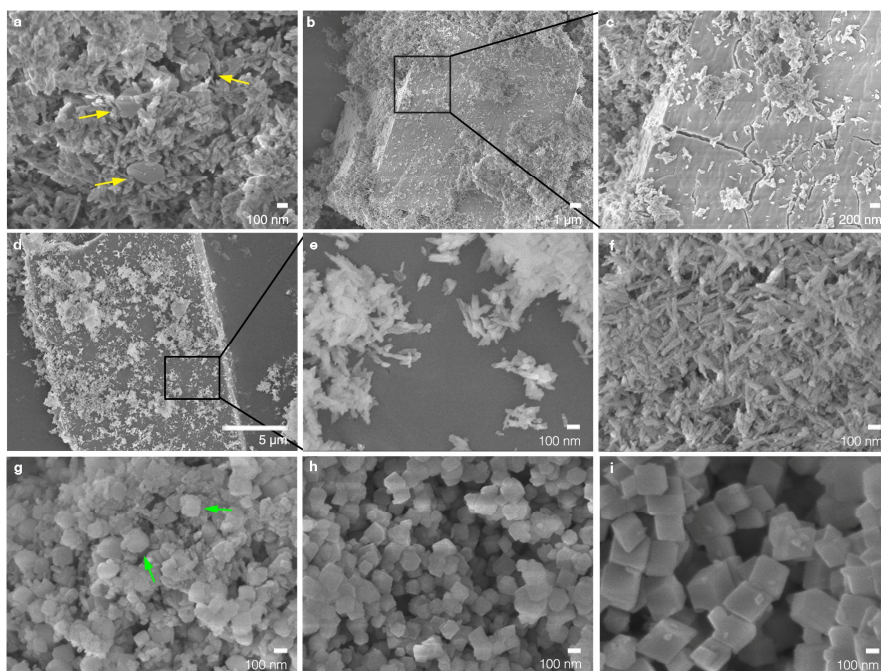


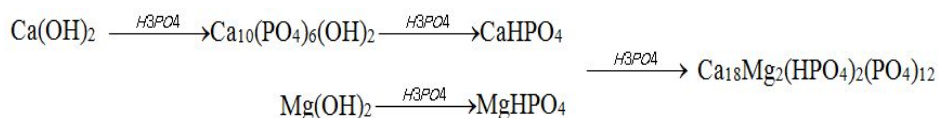
Figure 5.8 Morphologies of the intermediate phases of whitlockite (WH) during precipitation in $\text{Ca}(\text{OH})_2\text{-Mg}(\text{OH})_2\text{-H}_3\text{PO}_4$ system. **a**, During stage II ($70\text{ }^\circ\text{C}$, 225 mL of H_3PO_4 addition), rice shaped HAP nanoparticles and polygonal platelet shaped $\text{Mg}(\text{OH})_2$ were observed together in nanometer scale. $\text{Mg}(\text{OH})_2$ platelets are pointed by yellow arrow. **b**, At stage III ($70\text{ }^\circ\text{C}$, 370 mL of H_3PO_4 addition), cuboid like MP crystals were formed in micrometer scale. **c**, At the surface of huge cuboid like MP crystals, rice shaped HAP nanoparticle were existed (identical sample with b). **d-e**, At stage IV ($70\text{ }^\circ\text{C}$, 1 minute aging), large platelet shape of DCPD was formed and rice-shaped HAP nanoparticles still existed. **f**, When the temperature of the system was at $80\text{ }^\circ\text{C}$, with 1 minute aging process, only HAP particles were observed. **g**, At stage V ($70\text{ }^\circ\text{C}$, 5 hours of aging), rhombohedral morphology of WH particles began to show among rice shaped HAP

particles. WH particles are pointed with green arrows. **h**, At stage VI (70 °C, 24 hours of aging), the general shape of the nanoparticles were rhombohedral which reflected that only WH phase existed. **i**, When the temperature was at 65 °C, after 2 weeks of aging time, WH nanoparticles grew and had larger size.

To comprehend phase transformation mechanism in aspect of atomic movement, contents of Ca^{2+} and Mg^{2+} inside the precipitants and filtrates from different experiment times were compared. We used Inductively Coupled Plasma (ICP) to compare the ratio of components in the precipitants, which were collected before the reaction was started, after 1 minute from the addition of H_3PO_4 was terminated and after the aging process of 24 hours was passed. As shown in Figure 5.9a, before the reaction, the molar ratio between Ca and Mg in the precipitant was 77% and 23%, respectively. Then, after the full addition of H_3PO_4 into the $\text{Ca}(\text{OH})_2$ - $\text{Mg}(\text{OH})_2$ solution, the molar ratio between Ca and Mg in the precipitant changed into about 96% and 4%, respectively. In addition, the ratio of total cation (Ca+Mg) over anion (P) was found to be 1.5991. Based on these ratios, we calculated the molar ratios between initial phases of MP, DCPD and HAP as 1:3:11.7, in the premise that magnesium was hard to incorporate inside of DCPD and HAP. Finally, when only WH phase was existed in the system, the molar ratio between Ca and Mg was 90% and 10%, respectively. Therefore, whereas HAP dissolved in the proton rich environment, WH was precipitated by stabilizing its chemical structure from incorporation of Mg^{2+} .

In Figure 5.9b, ion chromatography analysis was conducted in

order to observe the transition of the residual amount of ion in the system. We quickly collected slurry from the each of the given time and separated transparent filtrate by filter press method. Then, the concentrations of free ion state of Ca^{2+} and Mg^{2+} in the filtrate were measured. 1 minute after the total addition of H_3PO_4 , free ion state of Mg^{2+} and Ca^{2+} existed approximately 2940 ppm and 1076 ppm, respectively. Therefore, excessive Mg^{2+} ions were present at the outside of the precipitants. Then, as the phase transformed into WH, concentration of Mg^{2+} decreased to 808 ppm whereas concentration of Ca^{2+} decreased to 604 ppm. More loss of Mg^{2+} in solution reflects that Mg^{2+} ions have involved in the newly formed WH structure from the outer system. In other words, the previous HAP phase dissolved into Ca^{2+} and PO_4^{3-} ions, and WH phase was rebuilt based on the Mg^{2+} ion. The early precipitants also confirmed that Ca-related precipitants and Mg-related precipitants formed separately and united into WH at final stage, as shown as below equation.



Even though, hexagonal crystal structure of HAP and rhombohedral crystal structure of WH might seem to be somehow related, it was reported that phase transformation between HAP and WH by spontaneous movement of minimum atoms would be difficult to occur¹¹. WH has higher packing density normal to the c axis compare to that of HAP, due to the strong bindings between Ca and P across the edge region. Therefore, it would

require certain bond breakages and reformations to transform WH phase into HAP. In addition, structure of HAP is inappropriate to incorporate Mg^{2+} in its structure. Therefore, it might be reasonable to suppose that HAP was dissolved in acidic condition and then WH was precipitated based on the chemical combination of Mg^{2+} and HPO_4^{2-} along with Ca^{2+} and PO_4^{3-} .

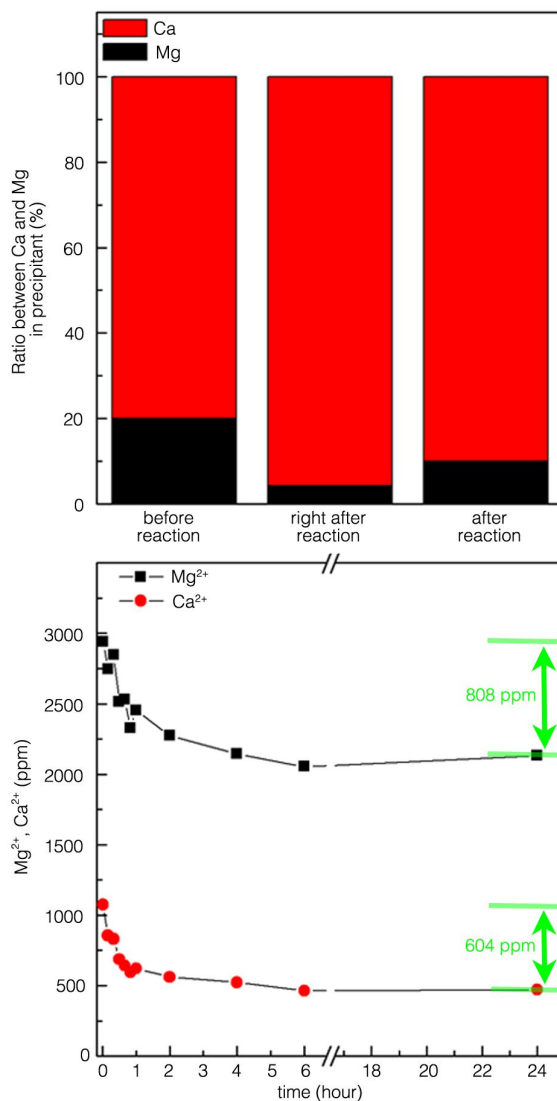


Figure 5.9 Change of the amount of the Ca²⁺ and Mg²⁺ in the precipitant and filtrate during the precipitation process of whitlockite (WH). **a**, Ratios of Ca and Mg in the precipitants from different experiment time analyzed by Inductively Coupled Plasma. **b**, Amount of Ca²⁺ and Mg²⁺ in free ion state during the formation of WH in Ca(OH)₂-Mg(OH)₂-H₃PO₄ system, analyzed by ion chromatography.

Based on the experimental data, we presented kinetic path diagram of WH depending on the temperature in Figure 5.10. As the temperature of the system became higher, kinetic transformation toward WH occurred faster. On the other hand, more detailed intermediate phases can be observed at the lower temperature condition. In this diagram, we can clearly see that calcium phosphate compounds transform into WH in proton-rich and Mg^{2+} -excess condition. In fact, WH can also be obtained by aging HAP particles with additional Mg^{2+} in acidic environment, as shown in Figure 5.11. Likewise, kinetic mechanism of WH in ternary $Ca(OH)_2$ - $Mg(OH)_2$ - H_3PO_4 system can imply actual formation mechanism of WH in the *in vivo* system, even though our body environment is a complex and dynamic system which involves various ions, proteins and even cell functions. For example, our bone continuously remodels itself by bone mineralization process of osteoblast and bone resorption process of osteoclast. Interestingly, it is known that osteoclast makes lacunae on the bone surface by producing acidic substance and, thus, making locally acidic environment of approximately pH 3~4.5. This is unstable pH condition for HAP while exactly preferred pH range for WH. Therefore, in our body, there might be chance to precipitate WH in local acidic regions. In addition, as there are various catalytic reactions occurring in our body system, such as functions of enzymes or biomolecules, WH might have been possibly induced along with effects of these catalytic reactions.

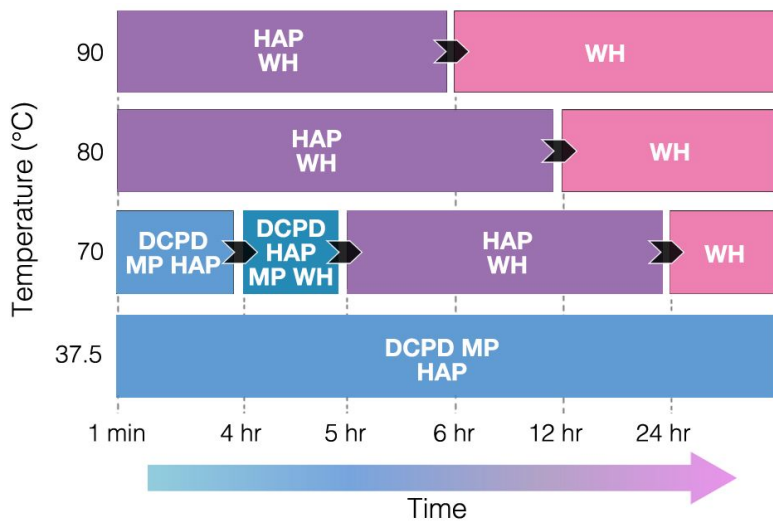


Figure 5.10 Kinetic path of precipitation of whitlockite in $\text{Ca}(\text{OH})_2$ - $\text{Mg}(\text{OH})_2$ - H_3PO_4 system depending on different temperature condition.

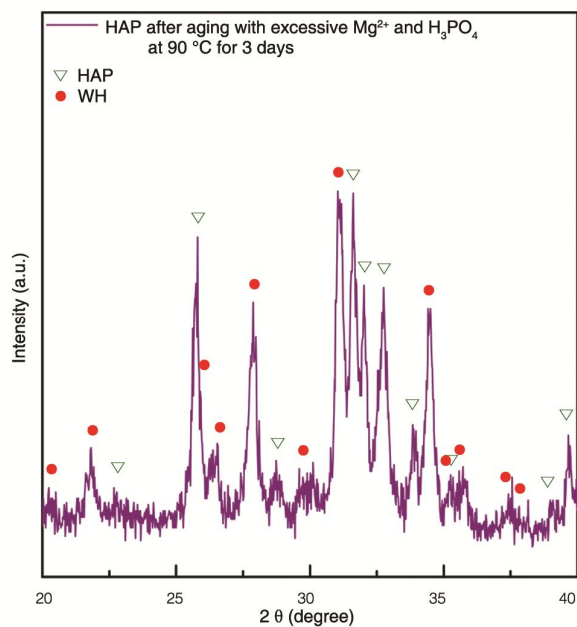


Figure 5.11 Partial transition of hydroxyapatite into whitlockite after aging with excessive Mg²⁺ and H₃PO₄ at 90 °C for 3 days

5.4 Summary

In this study, we investigated the formation mechanism of WH in ternary Ca(OH)₂-Mg(OH)₂-H₃PO₄ system. During the decrease of pH in the system, the intermediate phases transformed into stabilized phases according to the changed condition of the system. Each Ca-related compound and Mg-related compound alternatively released ions to the system to react with the excess P. When all the amount of the P was added to the system, pH of the system dropped to about 3.3 where pre-existing phases such as HAP were no

longer stable. At this point, with Mg^{2+} and HPO_4^{2-} at the center, Ca, Mg and P all together constructed the most stable structural form which was confirmed to be WH. Therefore, while HAP was known to be the most stable form of calcium phosphate compound around neutral region, WH was found to be more stable than HAP in acidic region ($< pH\ 4.2$). From the precipitation mechanism of WH in $Ca(OH)_2$ - $Mg(OH)_2$ - H_3PO_4 aqueous system, we can deduce that the formation mechanism and the role of WH in our bone might be related with the microscopically formed acidic environment.

Chapter 6. Biocompatibility evaluation of whitlockite as a cell scaffold

6.1 Introduction

In this chapter, we tested basic biocompatibility of synthesized whitlockite (WH: $\text{Ca}_{18}\text{Mg}_2(\text{HPO}_4)_2(\text{PO}_4)_{12}$) compare to well-known biomaterials such as hydroxyapatite (HAP: $\text{Ca}_{10}(\text{PO}_4)_6(\text{OH})_2$) and tricalcium phosphate (TCP: $\text{Ca}_3(\text{PO}_4)_2$). Previous studies reported that HAP had better biocompatibility than TCP that general cellular growth rates and activity rates were higher^{176,177}. On the other hand, while synthesized HAP almost did not substituted with natural hard tissue when it is inserted in the *in vivo* system, TCP dissolved and induced recovery of hard tissue¹⁷⁸. In this regard, people have been used both materials separately or together by controlling their mixing ratio to regulate dissolution rate for proper clinical purpose^{179,180}. However, even though TCP is widely applied biomaterial, it is high temperature phase that does not form in our body system. In this respect, we thought that WH, which is the synthetic analogue of TCP can show even higher level of biocompatibility because WH precipitates in our body system. To confirm this, we fabricated WH, HAP and TCP into cylindrical scaffold for cell culture. Then we compared proliferation level of human osteoblasts grown on each scaffold. In addition, we also studied bone mineralization related cellular activities on each scaffold in RNA level and protein level by real time PCR and western blot, respectively.

In addition, possibility of osteoclast resorption is another important factor for implant material, because new bone can be mineralized at the lacunae site formed by osteoclast¹⁸¹. In fact, our natural bone is known to remodel continuously by the resorption process of the osteoclast cells and the mineralization activity of the osteoblast cells. By bone remodeling process, weak and damaged part of the bone can be replaced into healthy state of new bone. It was reported that osteoclast can resorb bone by secretion of HCl by $\text{Cl}^-/\text{HCO}_3^-$ exchange and pH of the underneath microenvironment of the activated osteoclast was measured to be approximately 3~4.5, using pH microelectrode^{174,175}. Notably, bone mesenchymal stem cells are reported to migrate to the resorption sites by transforming growth factor- β 1 signal and then differentiate into osteoblast cells by stimulations of physical conditions of exposed surface of lacunae and various osteotropic factors such as bone morphogenetic proteins or platelet-derived growth factor¹⁸¹. If one implant material can actively participate in this bone remodeling process, it would easily and naturally harmonize with surrounding bone tissue. In this regard, previous TCP material had limitation that it was too rapidly dissolved by its high solubility and induced abnormally high concentration of ions existing state near dissolved material which prevented natural osteoclast resorption process^{177,182}. In this chapter, we examined resorption level of WH from human osteoclast cells and compared with that of HAP and TCP.

6.2 Whitlockite observation in human tooth

Prior to the biocompatibility tests, we tried to confirm the existence of WH in normal human tooth. As shown in Figure 6.1a, human tooth was polished and washed into clean state. From the FESEM observation, we observed that the cross-section of the human tooth was composed of well-organized inorganic nanoparticles (Figure 6.1 b-c). Then, we analyzed the cross-section of the tooth by Secondary Ion Mass Spectroscopy and found that Mg^{2+} existed as clusters among the inorganic nanoparticles. The distribution of the Mg^{2+} was shown to be concentrated in short-range rather than homogeneously scattered. Because WH formation requires secondary ions other than Ca^{2+} , such as Mg^{2+} , the distribution tendency of Mg^{2+} might reflect the localized existence of WH. In this regard, general XRD analysis was not sufficient to detect short-range phases. Therefore, to obtain direct crystallographic information, we separated small part of tooth by FIB and analyzed its lattice distance by HRTEM. Most of the crystallites seemed to be apatite-like phases but some local regions showed their lattice distances corresponding to WH. For example, as shown in Figure 6.1e, we found localized area with the lattice distance of 6.441 Å, which was identical with the d-spacing value of (1 0 4) plane of WH. In addition, selected area diffraction pattern analysis was also conducted with similar tooth sample prepared by FIB. In Figure 6.1f, while most of the diffraction patterns corresponded to HAP, some diffraction spots with d-spacing values of 6.441 Å and 6.181 Å clearly matched with (1 0 4) and (0 0 6) planes of WH phase. Therefore, consistent with previous report, we also proved that WH existed in our

normal hard tissue.

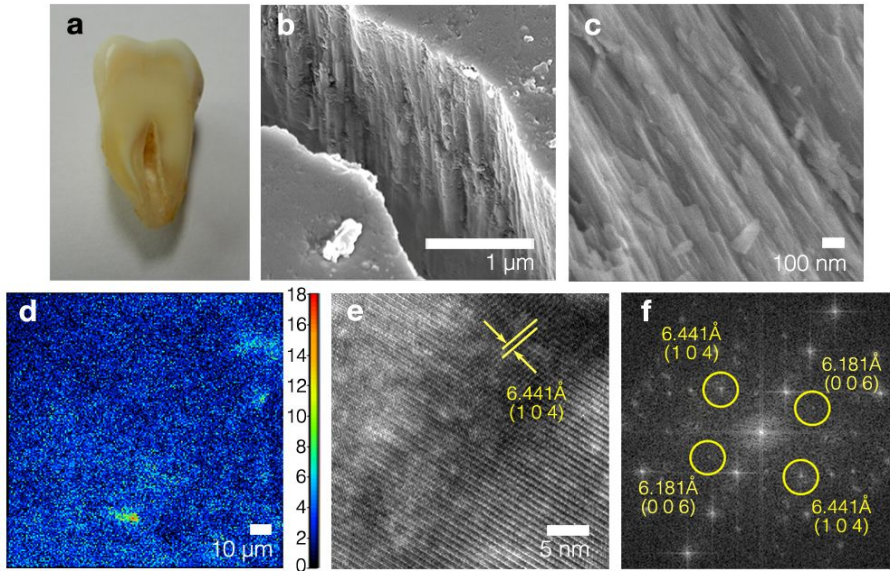


Figure 6.1 Direct observation of whitlockite (WH) in human tooth. **a**, Cross-section of the normal human tooth was analyzed after polishing and cleaning process. **b**, From the FESEM observation, the crack on the polished surface of the tooth showed that inner structure of the tooth was three dimensionally organized by inorganic nanoparticles. **c**, Inorganic nanoparticles with its width smaller than 100 nm were aligned with the directionality. **d**, SIMS analysis showed that Mg^{2+} clusters existed in short ranges at the cross-section of human tooth. Color distribution reflects the intensity of the Mg^{2+} ions according to their amount. **e**, From the HRTEM observation, lattice distance from the local region of the human tooth well matched with the d-spacing value of (1 0 4) plane of WH. **f**, Diffraction spots of human tooth from SAED analysis corresponded to the d-spacing values of (1 0 4) and (0 0 6) planes of WH.

6.3 Cell proliferation level on whitlockite scaffold

To compare biocompatibility, we grew human osteoblast cells (Lonza Clonetics) on the surface of WH, HAP and TCP which were all fabricated into cylindrical pellet form. Cells were seeded on the surface of the pellet with diameter of 1 cm, at a density of 1×10^5 cells/mL. Cell proliferation level on each material (n = 10) was compared by 3-(4,5-dimethylthiazol-2-yl)-2,5-diphenyltetrazolium bromide (MTT) assay at day 1, day 4, day 7 and day 10 after seeding point (day 0). It is already known that HAP has better biocompatibility than TCP for cell growth¹⁷⁶ and our result also showed similar tendency (Figure. 6.2). Interestingly, cells grown on WH pellet showed even better proliferation state than the growth level of cells on HAP pellet. In addition, as shown in Figure 6.3 a-f, cell growth state on the surface of each material was directly observed by staining nucleuses and actin cytoskeleton network in cells by DAPI (green) and phalloidin (red), respectively, at day 4 and day 7. Analogous with the MTT result, cells were grown vigorously on the whole surface of both WH and HAP. On the contrary, only few cells were grown on the surface of TCP pellet.

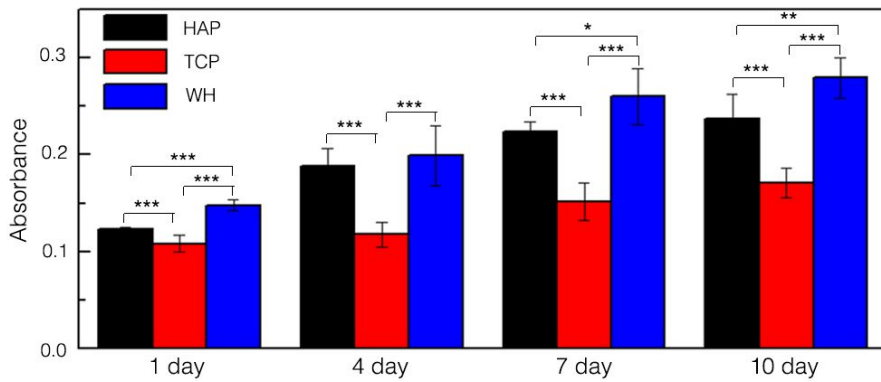


Figure 6.2 MTT cell proliferation test of human osteoblast cells grown on the surface of hydroxyapatite (HAP, black), tricalcium phosphate (TCP, red) and whitlockite (WH, blue) in cylindrical pellet form. From the initial seeding point (0 day), amount of cells on each sample was compared after 1 day, 4 days, 7 days and 10 days (n = 10). The statistical significances between the two groups were determined by the Student's t-test. *p < 0.01, **p < 0.005, ***p < 0.001.

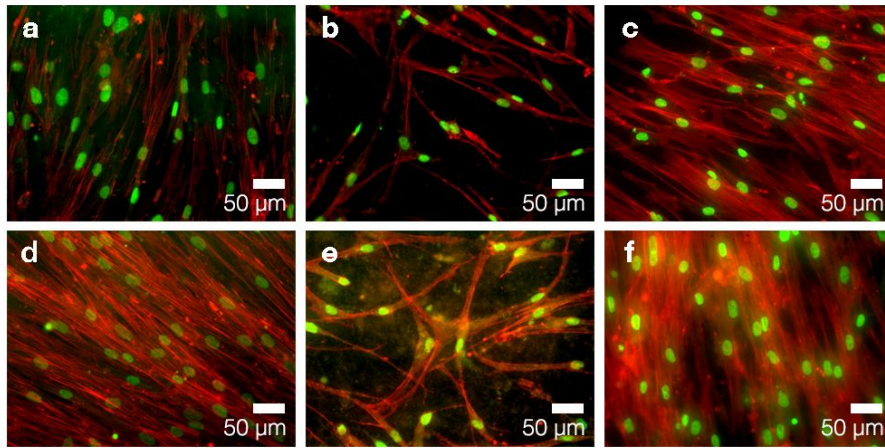


Figure 6.3 Direct observation of cells grown on the surface of scaffold made by hydroxyapatite (HAP), tricalcium phosphate (TCP) and whitlockite (WH). **a-f**, Fluorescence images of cells grown on the surface of cylindrical pellet made by **a**, HAP, **b**, TCP and **c**, WH after 4 day and **d**, HAP, **e**, TCP and **f**, WH after 7 day. Nucleuses and actin cytoskeleton network of cells were stained by DAPI (green) and phalloidin (red), respectively.

6.4 Cellular activity level on whitlockite scaffold

To verify that bone cells were not only proliferating on the surface of the WH pellet, but also active in bone formation process, quantified gene expressions associated to bone-mineralization process were compared relative to HAP, as described in Figure 6.4. After 2 days of osteoblast cells grown on the surface of HAP and WH pellet, RNA was extracted from the cells of each sample. Real time quantitative PCR (RT-qPCR) analysis was

conducted to evaluate messenger RNA (mRNA) level of cells from each sample (n = 5) and $\Delta\Delta C_t$ method was used on the basis of mRNA level of cells grown on HAP surface. The data from the RT-qPCR analysis showed that WH reinforced osteoblast cell function equivalent to the bone cells grown on HAP.

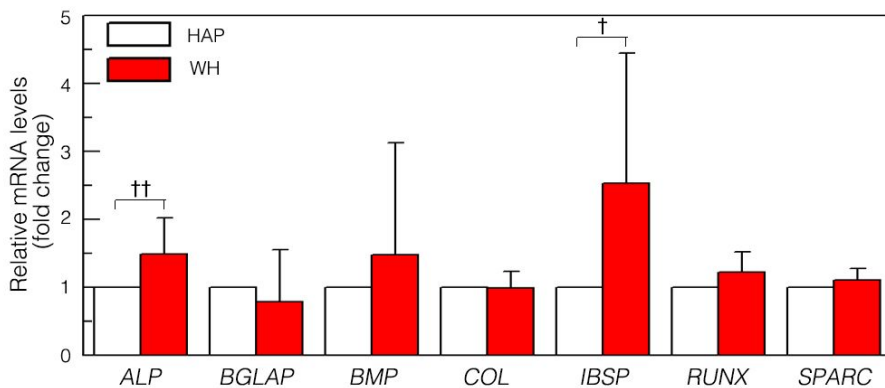


Figure 6.4 Relative gene expression evaluated by quantitative real time PCR indicated that osteoblasts grown on whitlockite expressed equivalent level of bone formation associated genes compared to the cells grown on hydroxyapatite. The statistical significances between the two groups were determined by the Student's t-test. † $p < 0.1$, †† $p < 0.05$

In addition, we also performed western blot to compare activity levels of bone mineralization related to proteins expressed from osteoblasts grown on the surface of WH and HAP scaffolds. Total proteins were extracted from the osteoblasts after 2 days of culturing on the each scaffold. Same concentration of proteins from HAP and WH samples were separated

by electrophoresis. In Figure 6.5, *GAPDH* was used as a control protein and band thicknesses of HAP showed similar or slightly thicker than that of WH. Activity level of *OPN*, *SPARC*, *BMP*, *AP* and *RUNX* all showed comparable state between osteoblasts grown from HAP and WH, respectively. Positions of bands were well matched with the reported size values of the purchasers, within approximate range of ± 15 kDa. In addition, around predicted size region, only single band appeared for each specific antibody. These results indicate that osteoblasts grown on WH were active in bone mineralization process as much as that of HAP.

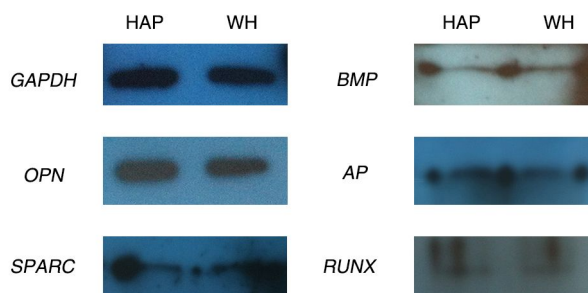


Figure 6.5 Western blot images of proteins extracted from osteoblasts grown on hydroxyapatite and whitlockite scaffolds. *GAPDH* was used as a control and other bone mineralization related proteins; *BMP*, *OPN*, *AP*, *SPARC* and *RUNX* all showed comparable levels in both samples.

6.5 Cellular resorption on whitlockite scaffold

To observe the ability of osteoclast cells resorbing surface of WH

scaffold, we grew human osteoclast precursors on the surface of cylindrical pellet of HAP, WH and TCP for 1 month. The osteoclast precursor basal medium was exchanged for every 3 days. All samples were kept at 37 °C in 5% CO₂ incubator. After 1 week, as shown in Figure 6.6, we found several numbers of matured states of osteoclasts with multinucleate cells grown on the bottom surface of the well plate around WH pellet. Thus, we assumed that pre-osteoclasts might also have been combined with each other on the surface of pellet. We continued to grow osteoclasts for additional 3 weeks and collected the samples.

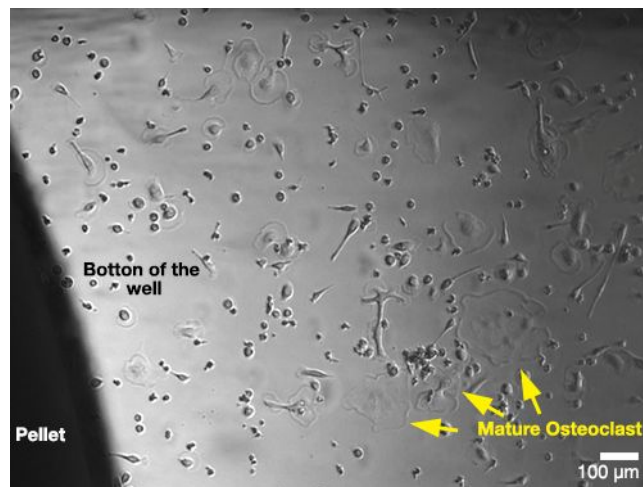


Figure 6.6 Mature states of multinucleated osteoclasts grown on the bottom of the well plate, next to whitlockite pellet.

From the FESEM image of Figure 6.7, the initial state of pellets made from HAP, WH and TCP all had flat surfaces. After osteoclasts were grown on their surfaces, lacunae were formed from the resorption activity.

Most of lacunae formed on the surfaces of HAP and WH pellets had approximate diameter of 5~10 μm . Because TCP was made from solid state method, it showed clear grain formation on the surface with much larger size than other HAP and WH pellets. In addition, dissolved area of TCP was much larger than that of HAP and WH with different morphologies that dissolved regions were formed along the boundary of grains.

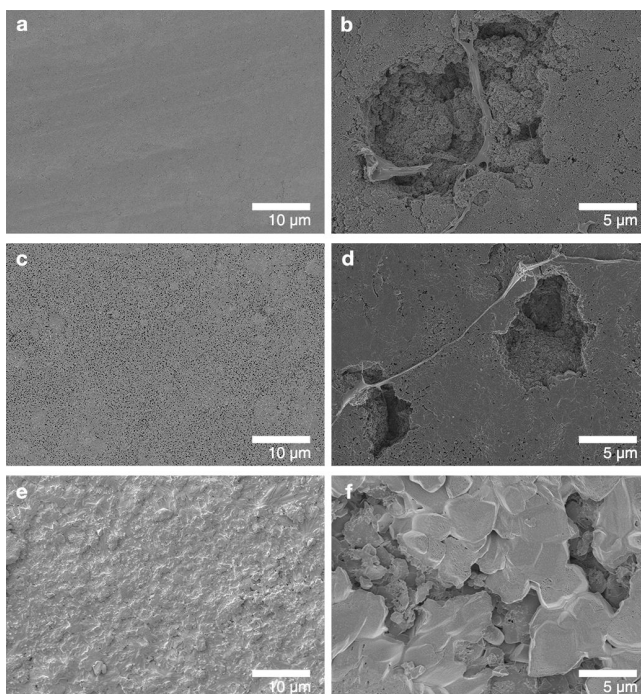


Figure 6.7 Lacunae formation on the surface of hydroxyapatite (HAP), whitlockite (WH) and tricalcium phosphate (TCP) pellets by osteoclast resorption activity. Surface of HAP pellet (a), WH pellet (c) and TCP pellet (e) were initially flat without any significant cracks. After the growth of osteoclast for 1 month, many lacunae were formed on the surface of HAP pellet (b) and WH pellet (d), whereas TCP pellet (f) showed different

morphologies of dissolved regions due to its high solubility.

Previously, it was reported that TCP itself has faster dissolution rate than HAP, whereas osteoclast resorption activity is lower at TCP surface than that of HAP due to high calcium concentration around TCP surface^{177,182}. Our experiment also indicated that the surface of TCP dissolved more than the surfaces of HAP and WH which might have been accelerated by dissolution process. In addition, in earlier chapter, we showed that WH had lower solubility than HAP at acid pH region. The result from osteoclast resorption study indicated that even though WH had better stability than HAP, morphologies of lacunae were similarly formed in both surfaces of WH and HAP. Therefore, WH might also be able to induce new bone formation around its lacunae during bone remodeling process in our body system.

6.6 Summary

The growth rate and the gene expression level of the human bone cells grown on the WH scaffold were similar or slightly higher compared to that of HAP and TCP, in the current experiment model. However, in addition to the intrinsic property of WH, we notice that better biocompatibility of WH might be induced from many factors such as nanostructure, mechanical hardness and roughness. Therefore, careful analysis about the exact mechanism can be the next important issue that should be investigated. For

example, we found that the Vickers hardness value of the scaffold made from WH was approximately 0.9 GPa while that of HAP and TCP were about 0.42 GPa and 0.19 GPa, respectively. Additionally, it is possible that Mg incorporation in WH can be one of the enhancing factors, as previously studied in other Mg-doped calcium phosphate systems. Increment of adhesion, proliferation, gene expression related to bone mineralization and amount of calcium containing mineral deposition of osteoblast grown on the Mg-doped calcium phosphate compounds have been previously reported¹⁸³⁻¹⁸⁶. Although the exact mechanism is still under study, the data presented here suggest a great possibility that can initiate the development and application of WH.

Chapter 7. Other application studies of whitlockite

7.1 Introduction

The purpose of this chapter is to suggest potential applications of whitlockite (WH: $\text{Ca}_{18}\text{Mg}_2(\text{HPO}_4)_2(\text{PO}_4)_{12}$) as a biomineral. Based on the newly discovered property of WH in previous and present chapter, this material can substitute some portion of usages of previous biomaterials such as hydroxyapatite (HAP: $\text{Ca}_{10}(\text{PO}_4)_6(\text{OH})_2$) or tricalcium phosphate (TCP: $\text{Ca}_3(\text{PO}_4)_2$). For example, optimal ratio of WH can be incorporated to the previous implant to enhance biocompatibility or mechanical properties for the proper purpose. For the further advanced *in vivo* study, basic mechanical property of WH scaffold using Vickers hardness method was shown, which is essential for the preparation of small implant. We also presented that WH nanoparticles can co-exist with free fluoride ions and can be effective as a toothpaste material. In the current chapter, methodology of rapid production of WH for the industrial usage was provided. Most of all, we expect that easy employ of WH provided in our study can be supportive to investigate the nature of bone tissue.

7.2 Fabrication of whitlockite into various types of bone implant according to its mechanical property

In this chapter, we showed that WH is fabricable into various implant form for further *in vivo* test. In addition, we included hardness data of WH compare to that of commercially used HAP (reagent grade, Aldrich) and TCP ($\geq 98\%$, Sigma-Aldrich), which might be useful for the further clinical test.

For small rat model, we prepared small implant with size of approximately 1 mm, which can fit into the peritoneum or brain. To observe newly formed bone tissue around the implant and cartilage, we made pores with dimension of about 330 μm . We gently mixed bead shaped polymethyl methacrylate (PMMA) with each of WH, HAP and TCP powder in optimized weight ratio of 1:2 (PMMA:WH) in order to get proper porosity. Each mixture was pelletized into cylindrical shape by giving pressure of 2 ton for 3 seconds, using mold with 1 mm diameter. To achieve similar hardness property, we compared hardness values of WH, HAP and TCP samples after heat treat in different temperature (Figure 7.1). Notably, the hardness of WH was exceptionally higher compare to that of HAP and TCP, after heat treated at identical temperature of 700 $^{\circ}\text{C}$. Hardness of WH, HAP and TCP was approximately 0.9 GPa, 0.42 GPa and 0.19 GPa, respectively. On the other hand, HAP and TCP had to be sintered at about 945 $^{\circ}\text{C}$ and 1050 $^{\circ}\text{C}$, respectively, to achieve similar hardness level with WH sintered at 700 $^{\circ}\text{C}$.

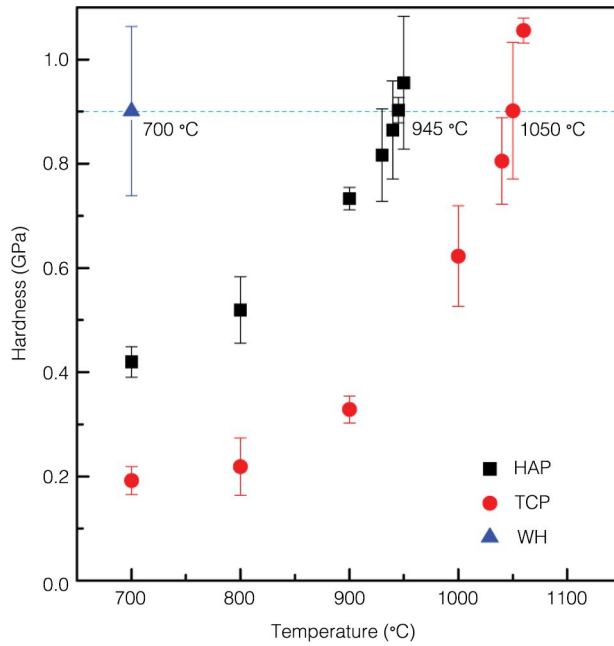


Figure 7.1 Vickers Hardness values of whitlockite, hydroxyapatite and tricalcium phosphate depending on different sintering temperatures.

According to this result, WH-PMMA, HAP-PMMA and TCP-PMMA pellets were heat treated up to 700 °C, 945 °C, and 1050 °C, respectively. During heat treatment process, polymers were burned out and removed. Then we crushed and filtered the pellet using two kinds of sieves with 1.18 mm size pores and 890 μm size pores to get samples with dimension about 1 mm. The resulted implant feature is shown in Figure 7.2.

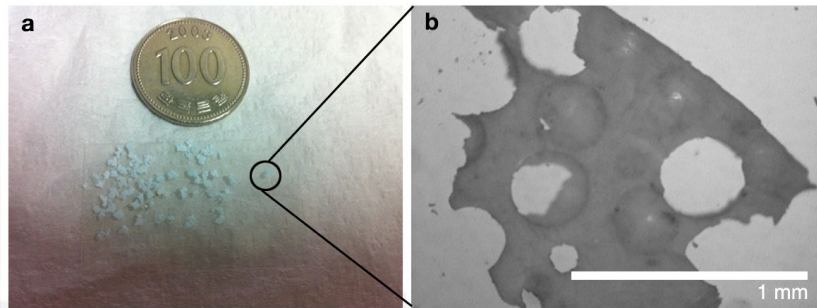


Figure 7.2 Images of porous implants with size of approximately 1 mm with pore dimension of about 330 μm .

In addition, for *in vivo* test in large rabbit model, we prepared cylindrical form of implant with diameter of 4 mm and height of 4 mm from each powder. The purpose of the *in vivo* test was to investigate absorption of the implant and to measure newly generated bone tissue around the implant, which would be inserted to tibia and cervical vertebrae. Like before, we made cylindrical type of pellet from each WH, HAP and TCP powder by giving pressure of 2 ton for 3 seconds. After heat treatment, to observe newly formed osseous tissue, we also built continuous channel with dimension of 300 μm inside the each implant using micro-drill. Final shape of the implant is shown in Figure 7.3.

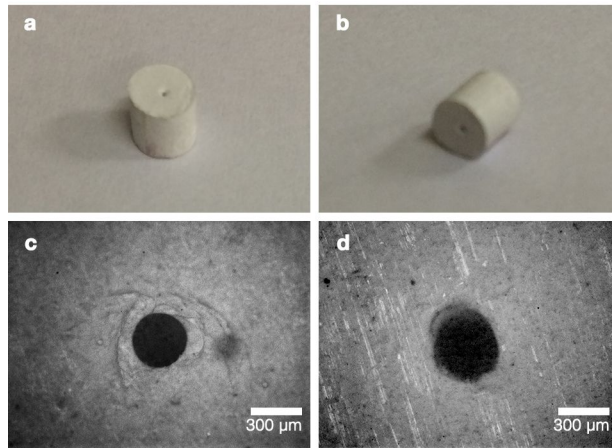


Figure 7.3 Images of cylindrical implant with both diameter and length were designed to be approximately 4 mm. The dimension of channel in the center was about 300 μm . **a-b**, Overall image of cylindrical implant with its pore at the center is shown. **c-d**, Cross-section of the channel from each side of the cylindrical implant is shown.

Therefore, WH can be fabricated into various forms of implants like previous HAP and TCP material. In addition, better mechanical property of WH compare to that of HAP or TCP suggested great potential of using WH as a future biomaterial. We expect that findings in this study can be foundation for the revealing the contribution of WH in mechanical property of our bone.

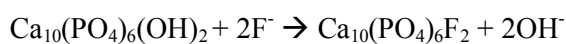
7.3 Whitlockite for toothpaste application

Calcium phosphate nanoparticles have been used in the toothpaste

applications in order to achieve remineralization process. Natural remineralization occurs from the saturation state of fluids and thus increment of calcium and phosphate concentrations are expected to induce accelerate remineralization. HAP nanoparticles are known to be effective in preventing and curing caries^{31,187}. In addition, HAP nanoparticles can reduce mouth odor by adsorbing organic substances such as polysaccharides, proteins and bacteria¹⁸⁸. Brightness and whiteness were reported to be enhanced according to the amount of HAP nanoparticles³².

Fluorides are also favored as a component of toothpaste because it can form fluorapatite (FAP: $\text{Ca}_{10}(\text{PO}_4)_6\text{F}_2$), which is one of the most thermodynamically stable apatite phase, at the surface of tooth and thus preventing demineralization while enhancing remineralization, based on its high stability¹⁸⁹. Moreover, after fluoride cross the cell wall in HF form, it dissociates into H^+ and F^- again and then disturbs enzyme activities inside the bacterium¹⁸⁹. Therefore, fluoride can eventually prevent dental caries and tooth decay.

However, when it comes to combine both effects of HAP and F^- for the purpose of toothpaste, as shown in the following chemical reaction, hydroxyl part of the HAP substitutes with F^- and becomes fluorapatite inside the toothpaste container.



As a result, F^- effect for preventing tooth decay reduces and the solubility of apatite also decreases that both materials become ineffective at remineralization process. In this respect, TCP was also used as a

remineralization source of the commercial toothpaste as it does not contain hydroxyl group in its chemical structure. However, as aforementioned, general particles size of TCP is bigger than micrometer scale and thus it might be less effective at filling small defect site of the surface of the tooth. On the other hand, WH can be synthesized in nanoparticles while it does not include hydroxyl group in its chemical structure. Therefore, we compared F^- ion uptake level of HAP, TCP, TCMP and WH to see whether WH can also coexist with free F^- ion. We mixed 500 ppm of NaF aqueous solution with 5 g of each powder at room temperature. After 24 hours of aging with stirring, filtrate from each sample was collected by filter-press. Then we compared concentration of F^- free ion of each filtrate by ion chromatography analysis. The uptake levels of F^- ion with HAP, TCP, TCMP and WH were 88.6%, 28.6%, 26.4% and 28.0%, respectively (Figure 7.4).

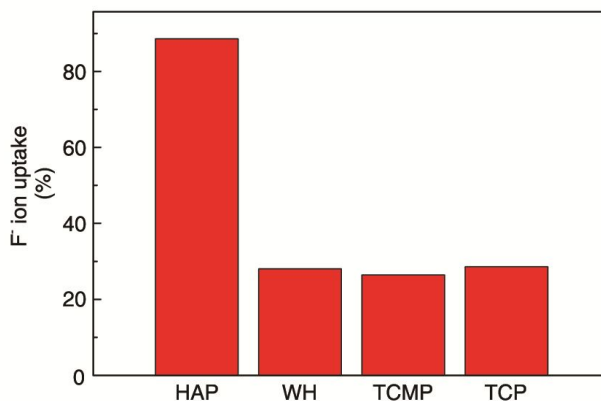


Figure 7.4 Fluoride uptake level (%) of hydroxyapatite (HAP), whitlockite (WH), magnesium-substituted tricalcium phosphate (TCMP) and tricalcium phosphate (TCP) after 24 hours of reaction with NaF in aqueous solution at

room temperature. While WH, TCMP and TCP all had compatibility with free F⁻ ions, only WH particles had nanometer scale size.

Basic uptake amount of F⁻ ion with WH, TCMP and TCP might have been induced from physical trapping of F⁻ ions between particles during filter-press process, which could also have been assisted by weak electrostatic adhesion between F⁻ and Ca²⁺ or Mg²⁺. From the Brunauer-Emmett-Teller (BET) analysis, surface areas of HAP, TCP, TCMP and WH were 84.83 m²/g, 0.29 m²/g, 0.36 m²/g and 29.02 m²/g, respectively. This indicates that much more amount of F⁻ ions might have been physically trapped between WH nanoparticles compare to bulk TCP and TCMP. Therefore, WH can be one of the future materials for toothpaste applications based on its high compatibility with F⁻ free ions and nanometer size, which can fill the small defects on the tooth.

7.4 Utilization of hydrogen peroxide catalyst for rapid production of whitlockite

For the scale-up production, WH can be rapidly precipitated by the support of hydrogen peroxide (H₂O₂), which is the green catalyst that only releases water as by-product and does not involve in the final product. Previously, gold nanoparticles were reported to be reduced in fast rate under the presence of H₂O₂ and produce non-aggregated nanoparticles ($2\text{Au}^{3+} + 3\text{H}_2\text{O}_2 \leftrightarrow 2\text{Au} + 3\text{O}_2 + 6\text{H}^+$)¹⁹⁰. Because H₂O₂ stimulate the nucleation of nanoparticles, as the concentration of H₂O₂ became higher, the size of the

nanoparticles turned out to be smaller with less distribution. For WH synthesis, H_2O_2 is decomposed into oxygen gas and water as heat is applied ($2\text{H}_2\text{O}_2 \leftrightarrow 2\text{H}_2\text{O} + \text{O}_2$). Then excess protons generated from the newly formed water might attack $\text{Ca}(\text{OH})_2$ and $\text{Mg}(\text{OH})_2$ and fast them to be ionized which then would rapidly nucleate into WH. In our experiment, we mixed more than 100 mL of H_2O_2 with $\text{Ca}(\text{OH})_2$ - $\text{Mg}(\text{OH})_2$ aqueous solution which made total volume of 500 mL. Then we added 500 mL of 0.95 M H_3PO_4 aqueous solution into the $\text{Ca}(\text{OH})_2$ - $\text{Mg}(\text{OH})_2$ - H_2O_2 aqueous solution at 80 °C. Notably, as shown in Figure 7.5, under the influence of H_2O_2 , WH was precipitated in 30 minutes. When the amount of H_2O_2 was increased, crystallinity of the WH was decreased maybe because the nucleation rate was too fast. In this respect, the size of the WH nanoparticles was much smaller when precipitated under the influence of H_2O_2 compare to that of WH nanoparticles synthesized without H_2O_2 (Figure 7.6). In addition, when H_2O_2 was added more than 300 mL, WH was able to be produced in $\text{Ca}(\text{OH})_2$ - $\text{Mg}(\text{OH})_2$ - H_3PO_4 aqueous system at 60 °C within 10 minutes. Therefore, we can assume that WH precipitation in the *in vivo* system might occur easily with the support of various matters including catalyst. We also expect that utilization of catalyst such as H_2O_2 will be effective for the mass production of WH in the industrial applications.

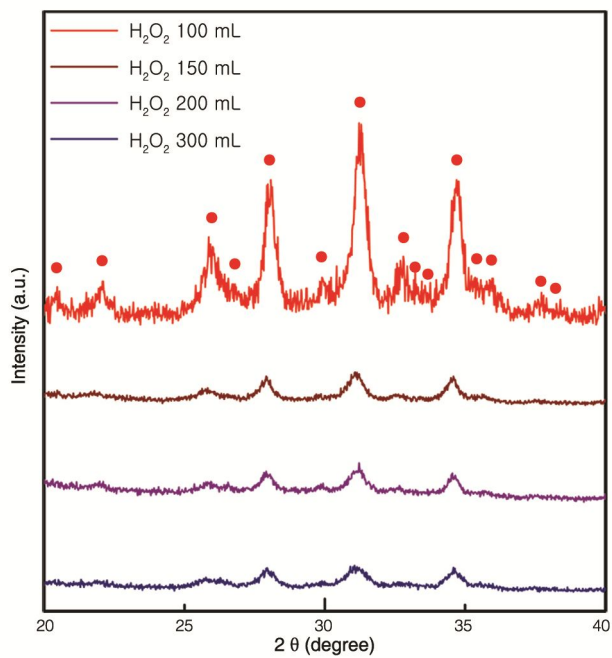


Figure 7.5 Rapid production of whitlockite in $\text{Ca}(\text{OH})_2\text{-Mg}(\text{OH})_2\text{-H}_3\text{PO}_4$ system at 80 °C, with different amount of H_2O_2 addition.

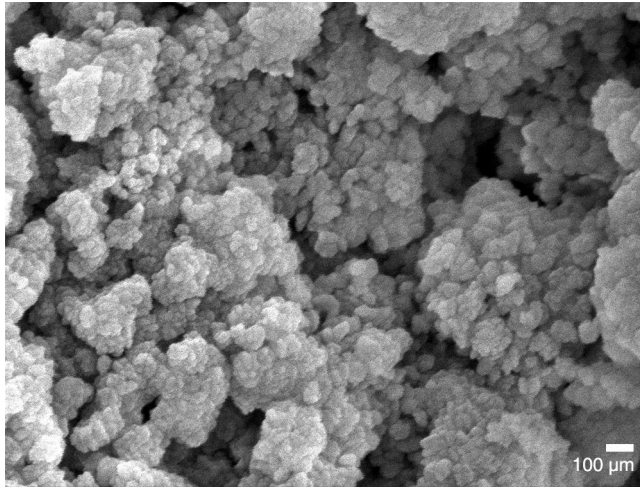


Figure 7.6 Image of rapidly precipitated whitlockite supported by green catalyst. Under the influence of H_2O_2 (100 mL), small size of WH nanoparticles were precipitated after aging for 30 minutes in $\text{Ca}(\text{OH})_2$ - $\text{Mg}(\text{OH})_2$ - H_3PO_4 system at 80 °C.

7.5 Summary

In this chapter, we tried to introduce potential applications of WH with some core data. Based on the mechanical property of WH evaluated from the Vickers hardness method, we fabricated various designs of WH implant for the purpose of further *in vivo* test. We provided detailed method to make porous implant, which can be inserted at the peritoneum and brain of the small rat model. We made WH, HAP and TCP porous implants with similar hardness value of 0.9 GPa by sintering each material at different temperature. In addition, process of fabricating cylindrical implant, which

can be inserted to tibia and cervical vertebrae of the large rabbit model was described. Then, we showed possible application of WH nanoparticles as a component of toothpaste from the co-exist capability with free fluoride ions which might induce remineralization effect. Finally, we also suggested method of rapid production of WH for the purpose of the industrial production using hydrogen peroxide as a green catalyst. Although profound investigation for each topic should be conducted before actual application, the data represented here suggest a great possibility of WH as a candidate material to overcome previous limitations of HAP and TCP. We also expect that our findings of synthesis method of WH nanoparticles and its properties can contribute to the revealing its precipitation mechanism and roles in our body system.

Part II. Structural control at nanoscale for bone implant

Chapter 8. Making bone implant ‘alive’ with built-in self-powered capillary supply of nutrients

8.1 Introduction

In nature, constructal law¹⁹¹ suggests that hierarchically arranged channels efficiently transport fluids and nutrients needed to enable and support biological activities. In addition, gradual surface energy changes are abundant in the structures of natural systems, facilitating the collection of water on spider web silk⁴², the transport of prey through the beaks of shorebirds⁴¹ and the desert beetle using its bumpy back to drink water¹⁹². Plant xylem and vascular capillaries are among the most well-known designs that combine these two principles. Such interconnected channels exist not only within soft tissues, but also within rigid hard tissues, such as bone^{193,194}, egg shell¹⁹⁵, crustacean tergite¹⁹⁶ and nail¹⁹⁷. Gases or fluids are exchanged through channels linking the proximal and distal parts of the plant to maintain pressure and/or to supply nutrients and growth factors.

One clinical challenge to re-create these natural nanoscale transport structures comes from bone implants in a medical setting. To date, conventional porous implant materials can only replace a limited range of the properties of natural bone. This limitation causes regular clinical failures

that can be attributed to the interfacial and structural differences between synthetic implants and the host bone. If the natural nanoscale transport structure of bone can be replicated in the implant material, such failures could be reduced or even eliminated, to the great benefit of patients and physicians. In synthetic systems, the use of millimeter or micro-sized channels to control and facilitate fluidic conduction between interfacial sites has been widely investigated¹⁹⁸⁻²⁰⁰. Here, we implemented a self-powered transport system of interconnected networks of capillaries ranging from micro- to nano-scale diameters in a model ceramic biomaterial made of hydroxyapatite (HAP: $\text{Ca}_{10}(\text{PO}_4)_6(\text{OH})_2$). This fluidic supply mechanism could be explained by the Laplace pressure model, which predicts a negative pressure gradient to arise from a capillary with a gradual narrowing diameter. To build a network of gradually narrowing nanochannels into the ceramic biomaterial, we devised a novel pressurized sintering method to create tapered nanochannels and to align the tapering direction of the nanochannels.

8.2 Bioinspired capillary fluid transport by the change in diameter of the channel

To validate our understanding of the underlying mechanism of gradual surface energy change and apply it to the engineering of the ceramic biomaterial, we demonstrated that a channel with a gradually changing diameter transports fluid more efficiently than a straight channel. When a tapered tube with gradually reducing diameter (2.4 mm to 1.1 mm) and a straight tube with diameter 2.4 mm were placed side by side in a Petri dish, the water in the tapered tube rose to a level that was 3.1 mm higher than in

the straight one, as shown in Figure 8.1a. This differentiation is general, and can be explained by Laplace pressure analysis. As indicated in Fig. 8.1b, the conical and straight tubes had the same radius R at the height to which the fluid rose in the straight tube.

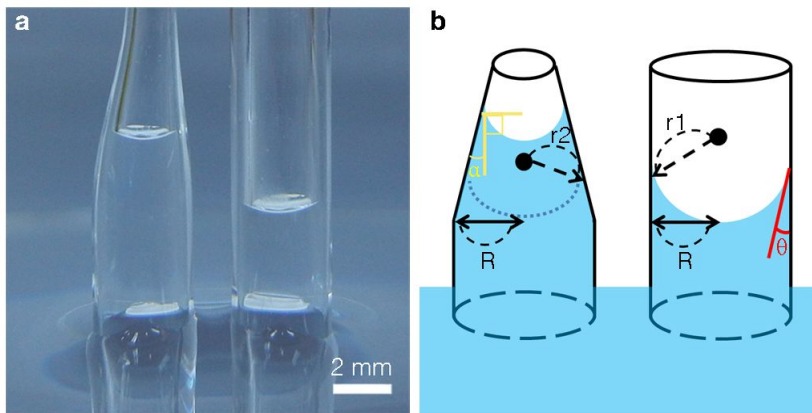


Figure 8.1 Bio-inspired capillary fluid transport in diameter-tapered channels. **a**, A conical tube and a cylindrical tube were both placed upright in pure water. Both glass tubes had an outside diameter of 4 mm, an inside diameter of 2.4 mm and a wall thickness of 0.8 mm, while up-most inside diameter of the conical tube was 1.1 mm. Water rose in the conical tube to 8mm, and in the cylindrical tube to 4.9 mm. **b**, Schematic diagram of the conical and cylindrical tubes. The conical tube is tapered to an angle ' α '. r_1 and r_2 are the radii of the spherical surfaces and ' h ' is the height. ' R ' is the radius of the cylindrical tube and of the conical tube at height ' h ' where the capillary rise of the cylindrical tube stops.

The additional rise in the tapered tube can be accounted for by the additional Laplace pressure associated with the tapering. This is because the

Laplace pressure is inversely proportional to the radius and also depends on the contact angle (interface tension), as defined by the following equation.

$$\frac{2\gamma^{LV}}{r_2} = \frac{2\gamma^{LV} \cos(\theta - \alpha)}{r_1 \cos \theta} = \frac{2\gamma^{LV} \cos(\theta - \alpha)}{R} \quad (1)$$

To deduce this equation, we excluded discontinuities such as bubbles in our capillary model and assumed that water rose as a connected column in the tube. The result in Fig. 8.1a showed that the capillary height in the conical tube reached 8 mm while the cylindrical tube reached only 4.9 mm. As indicated in Fig. 8.1b, α is the sloped angle of the conical shaped tube. r_1 and r_2 are the radii of curvature at height h in cylindrical and conical tubes, respectively. R is the radius of the cylindrical tube, and the conical tube has the same radius R at the height that corresponds to the water rise height within the cylindrical tube. The radii of curvature in both tubes could be expressed in terms of radius R as follows:

$$R = r_1 \cos \theta = r_2 \cos(\theta - \alpha)$$

$$r_2 = r_1 \frac{\cos \theta}{\cos(\theta - \alpha)} \quad (2)$$

In equilibrium, the force of gravity imparting downward pressure should be in balance with the surface tension. This relationship could be stated as:

$$\rho gh = \frac{2\gamma^{LV}}{r} = \frac{2\gamma^{LV}}{R} \cos \theta \quad (3)$$

Therefore, by substituting (2) into (3), we can deduce equation (1).

The expected dependence of the water level rise on the diameter of the tube is plotted in Fig. 8.2a. The capillary force is proportional to $\frac{1}{R}$ and $R = R_0 - x \tan \alpha$, where R_0 is the radius of the conical tube at height h . When 'H' is the total height of the capillary rise measured from the outside water level, $x = H - 4.9mm$, which indicates that x is the height of the capillary rise from height 'h'. In Fig. 8.2a, capillary height in the conical tube and the cylindrical tube were expected to be 7.95 mm and 5.04 mm, respectively. Therefore, the experimental results and theoretically predicted values correlated. Here, the contact angle θ was obtained from Fig. 8.1a as 65° and the surface tension value γ was assumed to be 0.07 N/m, which is the standard value for distilled water. For a straight tube of given diameter and interior surface, the Laplace pressure is a constant but inversely proportional to R. In Fig. 8.2a, the constant surface tension was represented as a horizontal line for ease of comparison. In the case of the tapered tube, the capillary force increased with the gradient angle (i.e., change in tube diameter). Fig. 8.2b compared the capillarity at several intersections between the gravitational force and the surface tension, corresponding to tubes with different gradient angles. As the gradient angle, α , increased, a higher rise of the capillary fluid level is expected.

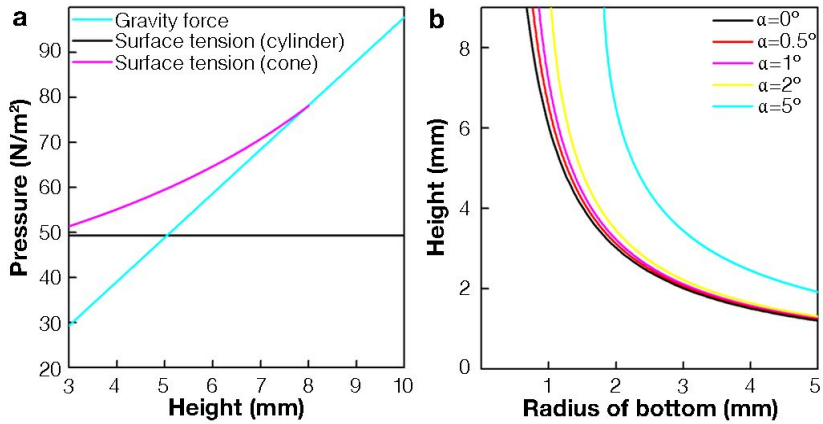


Figure 8.2 Capillary rise height depending on the level of gradient angle of the tube. **a**, The theoretical capillary rise heights of the conical and cylindrical tube are compared by the intersection of the surface tension and the force of gravity. The magenta and the black lines represent the surface tension of the conical tube and the cylindrical tube, respectively. The cyan line denotes increasing gravitational force at the water surface according to its height. **b**, Capillary rise heights from tubes with different gradient angle α were compared in calculation; $\alpha = 0^\circ$ (black line), $\alpha = 0.5^\circ$ (red line), $\alpha = 1^\circ$ (magenta line), $\alpha = 2^\circ$ (yellow line), $\alpha = 5^\circ$ (cyan line). The capillary rise height increased as the tube tapered more aggressively.

The merit of the conical structure can be equivalently represented by an increased flow rate of the transported fluid. This effect on flow-rate can be analytically modeled in the case of viscous, incompressible and laminar flow through a long tube with a small diameter relative to length and no edge effect. The model would show that the flow-rate in a conical tube is similarly increased with the tapering angle.

To derive equations to compare the velocities of the flux transport through different geometry of tubes, we made the assumptions listed below regarding the velocity of the fluid transport through a channel.

- a) We ignore the edge effect.
- b) We suppose the fluid is viscous and incompressible.
- c) We assume this transport occurs in laminar flow.
- d) We assume there is no acceleration during fluid transport in the tube.
- e) The tube is relatively long in relation to its diameter. ($dx \gg R$)

From Poiseuille's law, we can derive the velocity equation of the fluid $v(r)$ and the formula for the maximum velocity of the fluid v_{\max} at the center of the tube ($r = 0$), where the fluid is moving fastest. Here we denote η : viscosity, R : radius of the tube, ΔP : pressure difference between the two ends of the tube and ΔX : distance between the two ends.

$$v(r) = -\frac{1}{4\eta} \frac{\Delta P}{\Delta X} (R^2 - r^2)$$
$$v_{\max} = -\frac{1}{4\eta} \frac{\Delta P}{\Delta X} R^2 \quad (4)$$

In the following figure 8.3, we denote S and ds as the radius and thickness of the laminar fluid, respectively.

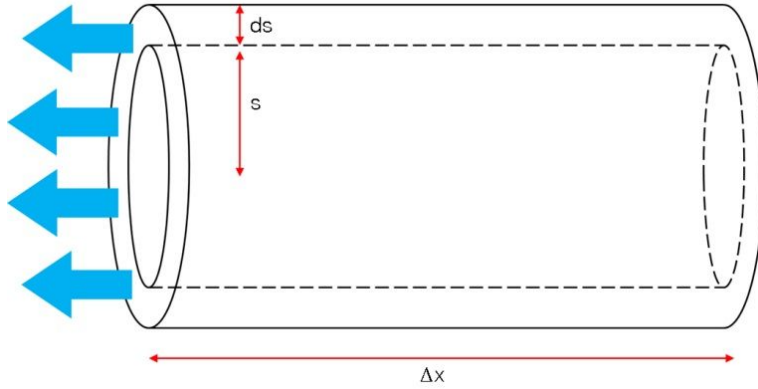


Figure 8.3 Simplified Laminar fluid with radius of S and thickness of the fluid as ds .

By assumption, there is no acceleration of the fluid, so $\Sigma F = 0$. Therefore, by combining the force by pressure, which is $-\Delta P \cdot 2\pi s ds$ and the force by the drag force within fluid layers, which is $-\eta \cdot 2\pi s \Delta x \left. \frac{dv}{dr} \right|_s + \eta \cdot 2\pi(s + ds) \Delta x \left. \frac{dv}{dr} \right|_{s+ds}$, we can deduce $-\Delta P \cdot 2\pi s ds - \eta \cdot 2\pi s \Delta x \left. \frac{dv}{dr} \right|_s + \eta \cdot 2\pi(s + ds) \Delta x \left. \frac{dv}{dr} \right|_{s+ds} = 0$.

This can be arranged as

$$\frac{1}{\eta} \frac{\Delta P}{\Delta x} = \frac{d^2 v}{dr^2} + \frac{1}{r} \frac{dv}{dr} = \frac{1}{r} \frac{d}{dr} \left(r \frac{dv}{dr} \right) \quad (5)$$

Using the boundary conditions of $v(R) = 0$ from the no-slip boundary condition for viscous fluid and $\left. \frac{dv}{dr} \right|_{r=0} = 0$ from the axial symmetry entailing the velocity is fastest at the center, we can deduce

$$v(r) = -\frac{1}{4\eta} \frac{\Delta P}{\Delta x} (R^2 - r^2).$$

Then, we supposed that the diameter at the top of the conical tube and the cylindrical tube was the same. Also, we assumed that the height of the cylindrical tube corresponded to the capillary rise height. Then, when these tubes are placed upright in pure water without additional applied force, they will have the same capillary rise height as determined by equation (3). However, since these tubes had different geometries as shown below in Figure 8.4, capillary pressures were derived differently from the Young-Laplace equation:

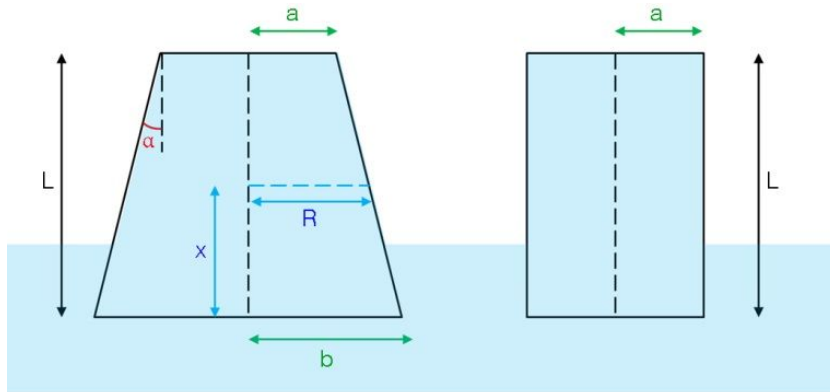


Figure 8.4 Cornical tube and cylindrical tube with different geometry while their radii are same as a at height L .

$$\begin{aligned} |\Delta P_I| &= \frac{2\gamma \cos(\theta - \alpha)}{R} \\ |\Delta P_{II}| &= \frac{2\gamma \cos \theta}{a} \end{aligned} \quad (6)$$

Here, the symbols represent α : the sloped angle of the conical shaped tube, a : the radius of the cylindrical tube and radius of the top of the conical tube, b : the radius at the bottom of the conical tube and R : the radius of the conical tube at arbitrary height x . Then, from equation (4) based on Poiseuille's law, we can derive equations as below:

$$v_i = \frac{1}{4\eta} \frac{b-a}{(b-R)L} \frac{2\gamma \cos(\theta - \alpha)}{R} R^2 = \frac{\gamma}{2\eta L} \frac{b-a}{b-R} R \cdot \cos(\theta - \alpha)$$

$$v_{ii} = \frac{1}{4\eta} \frac{1}{L} \frac{2\gamma \cos \theta}{a} a^2 = \frac{\gamma}{2\eta L} a \cos \theta$$

By combining these equations, we can rearrange the formula into $\frac{V_i}{V_{ii}} = \frac{\cos(\theta - \alpha)}{\cos \theta} \frac{b-a}{b-R} \frac{R}{a}$ and because R is a value between a and b , the velocity of the flux in the conical tube is faster than the velocity of the flux in the cylindrical tube. The detailed integral process is shown below following Figure 8.5.

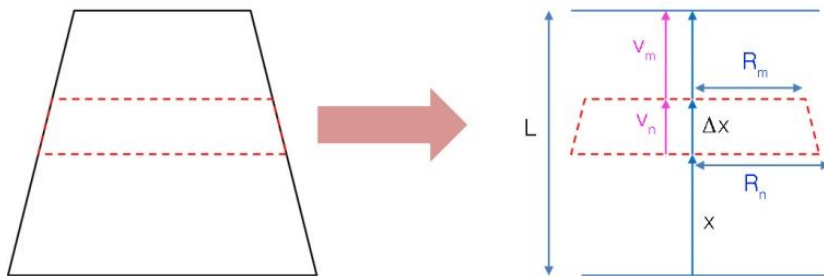


Figure 8.5 Flux in the conical tube

From equation (4) based on Poiseuille's law,

$$\begin{aligned}
 v_m &= \frac{(-1)}{4\eta} \frac{\Delta P_m}{\Delta X_m} R_m^2 \\
 v_n &= \frac{(-1)}{4\eta} \frac{\Delta P_n}{\Delta X_n} R_n^2 \\
 \Delta v &= +v_m - v_n = \frac{1}{4\eta} \cdot 2\gamma \cos(\theta - \alpha) \left[\frac{R_m}{X + \Delta X} - \frac{R_n}{X} \right] \quad (7)
 \end{aligned}$$

Now, from the geometry of the conical tube presented above,

$$\begin{aligned}
 R &= b - \frac{b-a}{L} X \\
 R_m &= b - \frac{b-a}{L} (X + \Delta X) \\
 R_n &= b - \frac{b-a}{L} X \quad (8)
 \end{aligned}$$

If we insert equation (8) into equation (7) and integrate both sides (left: $v(L) \rightarrow v(X)$, right: $L \rightarrow X$)

$$\begin{aligned}
 \Delta v &= +v_m - v_n = \frac{1}{4\eta} \cdot 2\gamma \cos(\theta - \alpha) \left[\frac{b}{X + \Delta X} - \frac{b}{X} \right] \\
 &\approx \frac{1}{4\eta} \cdot 2\gamma \cos(\theta - \alpha) \cdot b \cdot \frac{(-1)\Delta X}{X^2} \\
 v(X) - v(L) &= \frac{1}{4\eta} \cdot 2\gamma \cos(\theta - \alpha) \cdot b \cdot (+1) \cdot \left(\frac{1}{X} - \frac{1}{L} \right) \quad (9)
 \end{aligned}$$

As $v(L) = \frac{1}{4\eta} \cdot \frac{1}{L} \cdot 2\gamma \cos(\theta - \alpha) \cdot a$ from Poiseuille's law,

$$v(X) = \frac{1}{4\eta} \cdot 2\gamma \cos(\theta - \alpha) \left[\frac{a}{L} + \frac{b}{X} - \frac{b}{L} \right] \quad (10)$$

$$\frac{V_i}{V_{ii}} = \frac{\frac{1}{4\eta} \cdot 2\gamma \cos(\theta - \alpha) \left[\frac{a}{L} + \frac{b}{X} - \frac{b}{L} \right]}{\frac{1}{4\eta} \cdot \frac{1}{L} \cdot 2\gamma \cos \theta \cdot a} = \frac{\cos(\theta - \alpha)}{\cos \theta} \left[1 + \frac{Lb}{aX} - \frac{b}{a} \right] \quad (11)$$

By combining equation (8) with equation (11), we can express equation (11) as $\frac{V_i}{V_{ii}} = \frac{\cos(\theta - \alpha)}{\cos \theta} \frac{b - a}{b - R} \frac{R}{a}$ which verifies the statement that the velocity of the flux in the conical tube is faster than the velocity of the flux in the cylindrical tube.

In addition, to derivate the velocity of flux transport in conical and cylindrical tubes with additional applied force, we assumed that the fluid was supplied though the channels at a constant velocity of V_0 in laminar flow state. Therefore, $\vec{v} = v_r \hat{r}$ and $v_{ii} = V_0$. Then, for incompressible flow,

$$\nabla \cdot (v_r \hat{r}) = \frac{1}{r^2} \frac{\partial}{\partial r} (r^2 v_r) = 0$$

$$v_r = \frac{C}{r^2} \quad (\text{where } C \text{ is a constant.}) \quad (12)$$

Therefore, the expression of V_i can be deduced from (12):

$$v_l = v_0 \left(\frac{r_2}{r_1} \right)^2 = v_0 \frac{b^2}{a^2}$$

$$\frac{v_l}{v_{||}} = \frac{b^2}{a^2}$$

As r is a polar coordinate, it refers to the distance from the origin where the radius of the conical tube is R . In the limit condition of $r = 0$, the opening of the tube is a point and the velocity will become infinite. We assume that r cannot be 0 while still maintaining 'tube' geometry.

In conclusion, regardless of the amount of extra applied force, the velocity of the flux is faster in the conical tube than in the cylindrical tube.

8.3 Generation of continuous graded pore structures in bioceramic through the new sintering method with sloped pressurization

We applied the knowledge gained from the conceptual experiments and models described above to engineer a network of tapered nanochannels into ceramic composites. In order to generate gradient and networked capillary nanochannels, we devised a new sintering process that incorporated a polymer of selected molecular weight into a blend with hydroxyapatite (HAP, $\text{Ca}_{10}(\text{PO}_4)_6(\text{OH})_2$) particles and subsequently sintered them with a unidirectional pressure gradient. We chose to work with HAP and polyethylene glycol (PEG, $\text{H}(\text{OCH}_2\text{CH}_2)_n\text{OH}$) because of their biocompatibility, application in bone implants, and phase segregation

tendency. By themselves, HAP powders do not form interconnected nanochannels after a conventional sintering process. However, with the addition of PEG and externally applied pressure gradient, a pressure-regulated process takes place in sintering that generated networked interconnected pore structures, which eventually formed networked channels with tapered geometry. Interestingly, when enough PEG was added to induce polymer aggregation, the size of the channel was dependent on the amount of local pressure, but inversely. As such, channels with gradually changing diameter could be controllably made by applying a pressure gradient during the sintering process.

The process we developed is one of several examples of the phase separation phenomena between polymer and nanocomposite using additional energy such as heat or electricity²⁰¹⁻²⁰³. In the present case, it is the combined mechanical and thermal energy that resulted in the formation of nanochannels and their networks through both the phase-segregation between PEG and HAP and its coupling to the altered liquid-vapor phase transition of the PEG and the also altered solid-liquid phase transitions of both PEG and HAP during the high-temperature sintering of the hybrid composite (Figure 8.6).

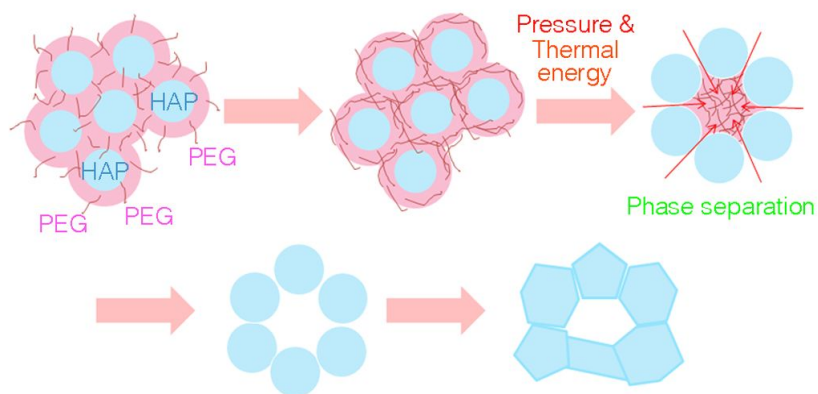


Figure 8.6 Phase segregation of polyethylene glycol polymer and hydroxyapatite during pressurized sintering process, depicting formation of an interconnected pore structure.

The size of the pore generated during the sintering depends not only on the local pressure but also on the amount of PEG. The particularly strong dependencies on the amount and the molecular weight of PEG are telling indicators of the phase segregation of PEG being a key factor in the generation of pores. Previous studies showed that PEG can be segregated, and more efficiently at a higher temperature²⁰⁴ or with a higher concentration of salts²⁰⁵⁻²⁰⁷. During our sintering process, the thermal energy and pressure allowed the PEG to detach, diffuse, and aggregate²⁰⁸⁻²¹¹. Initially, the PEG polymers were homogeneously mixed with the HAP particles. By electrostatic attraction, PEG polymers surrounded the surface of the HAP nanoparticles. When heat was applied, the PEG detached from the HAP surface. When additional energy was applied in the form of pressure, the PEG diffused and the polymers began to aggregate with each other, resulting in phase separation between the polymer and the nanocomposite. When the

temperature was above the boiling temperature of PEG, the polymer was completely burned out during sintering. The HAP nanocomposite precipitated as crystals and grew into larger grains, leaving behind pores in the areas vacated by the now burned-out PEG aggregates. In our system, increase in both melting and boiling temperature of PEG were observed, where higher increase in boiling point resulted at wider liquid region, exhibiting more favorable phase separation by applying the pressure, as shown in Figure 8.7.^{212,213} After sintering that reaches a peak temperature of 1100 °C, the PEG aggregates were completely burned out, leaving behind interconnected pores (or networked tapered channels) that increase in size from one end to the other perhaps counter-intuitively, along the same direction of the applied pressure gradient.

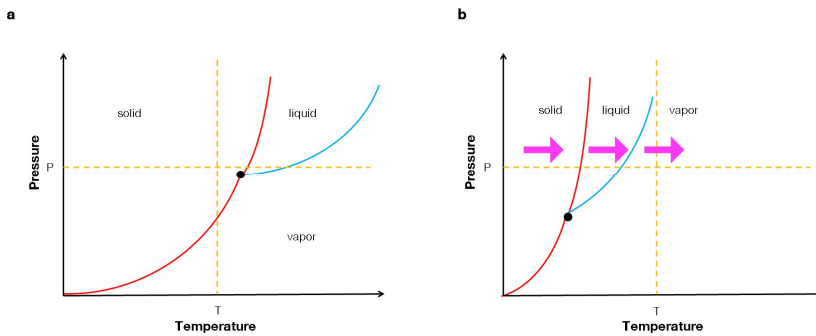


Figure 8.7 Phase diagram of AMCD-HAP components. **a**, HAP and **b**, PEG phase transitions based on temperature and pressure. PEG converts into a liquid and a vapor state as the temperature increases. In addition, as the applied pressure energy becomes greater, there is an increase in the liquid phase zone of the PEG.

In prior work performed in this field, pressurization during sintering was used as an aid to densify ceramic²¹⁴⁻²¹⁶ and a low concentration of

polymer (e.g., 1/10,000 by weight) was added as a binder. However, our results suggested that increasing both the amount and the molecular weight of the polymer to about 1/10 by weight and 10,000 g/mol or more, respectively, would change the role of the polymer into a major determinant of the sintered ceramic structure. This finding, along with that of the counter-intuitive dependence on pressure, was confirmed in all subsequent tests. Both parameters were utilized to make our ceramic sample with its built-in networks of tapered channels, with continuously varying diameter from micrometer to nanometer and shown in biological tests to provide self-powered nutrient supply for cell growth and differentiation.

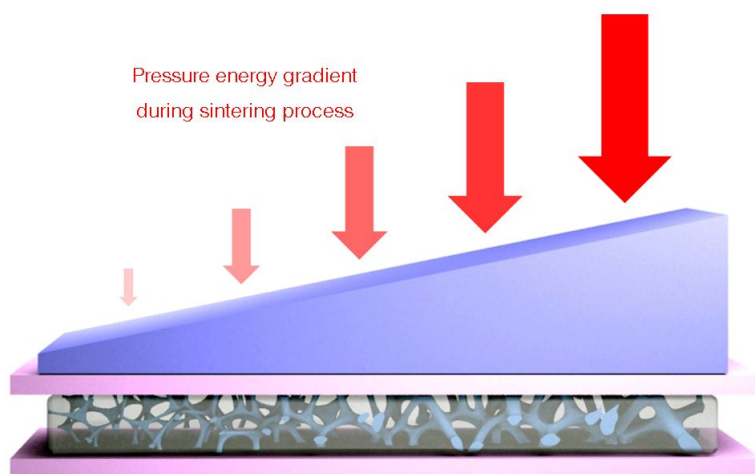


Figure 8.8 Generation of networked and graded capillary structures in bio-ceramic material through the application of unidirectional gradient of pressure during sintering.

For actual implementation of this particular pressurized-sintering concept, we created a pressure gradient by placing a triangular prism

(wedge) made of metal directly on the PEG-HAP sample (Figure. 8.8). In order to calculate the pressure applied by the metal wedge with total mass of 911.1 g, we supposed that each section of the metal wedge applied direct pressure to the area below it. Therefore, the local pressure P can be expressed as the loaded force over the area of the surface in contact. If we set x as the length of an arbitrarily defined section, we can obtain the highest pressure loading by setting $x \rightarrow 0$ near the heaviest end of the metal wedge. This can be written as:

$$\lim_{x \rightarrow 0} \frac{(\text{weight} \times 10^{-3})((l^2 - (l - x)^2)/l^2) \times 9.8}{(w \times 10^{-3})(x \times 10^{-3})},$$

where weight stands for the weight of the metal wedge, l is the length of the metal wedge and w is the width of the metal wedge. Division with this limit yielded a value of 34474.1 Pa for the pressure value at the heavy edge. Therefore, the highest local pressure we applied to the PEG-HAP sample was 34.47 KPa, near the heavier end of the metal wedge, and the loading gradually decreased along the length of the wedge. More sophisticated mechanical stress controls could be deployed, some of which were tried. But the simpler method described here turned out to be also the simplest to quantify the local pressure and its pressure gradient.

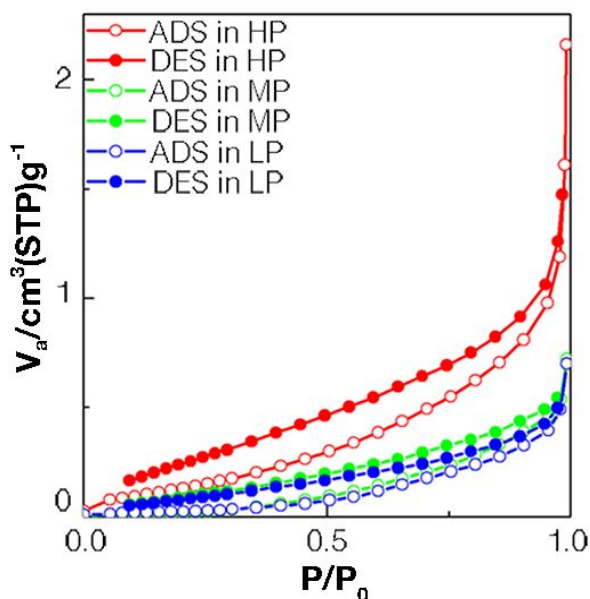


Figure 8.9 N₂ adsorption-desorption isotherm confirmed augmentation of porosity generated by the applied pressure. Three regions were compared; (HP) high pressurized, (MP) medium pressurized and (LP) low pressurized.

N₂ adsorption-desorption isotherm testing, corroborated with electron microscopy imaging findings, showed a gradual increase of internal porosity from one end to the other for the test HAP pellets, with the end that experienced the most pressure becoming more porous (Fig. 8.9). The total pore volume increased from 0.001 cm³/g in the region of lowest pressure to 0.003 cm³/g in the region of highest pressure, while the surface area also increased from 0.067 m²/g to 0.555 m²/g. In order to distinguish PEG-HAP samples generated in this way from nonporous or randomly porous HAP blocks, we refer to the resultant interior structure as Aligned Multiple

Capillary networks with gradually decreasing Diameter-HAP (AMCD-HAP), as presented in Figure 8.10.

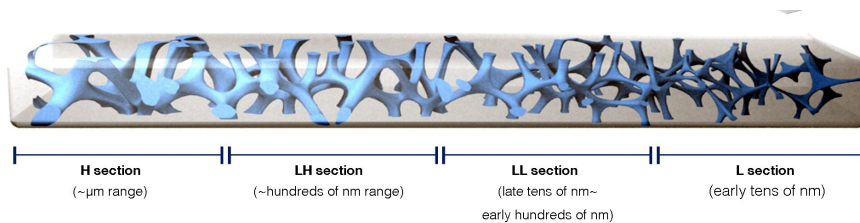


Figure 8.10 Schematic representation of AMCD-HAP with four different porosity sections shown.

This new AMCD-HAP bone implant material turns out to be mechanically as strong as (or even stronger than) natural bone of comparable weight and dimensions. Figure 8.11a shows a representative stress-strain curve obtained by uniaxial compression test of the AMCD-HAP. The ultimate compressive strength was measured as 26.5 ± 1.6 MPa, which is between the ultimate strengths of compact and trabecular human bone²¹⁷. The elastic modulus was obtained as 13.2 ± 2.2 GPa, which is slightly greater than the values obtained for human bone²¹⁸. Figure 8.11b shows the gradual change of the hardness in AMCD-HAP pellet from one end to the other, further confirming the continuously changing porosity. While in a similar range of order, the hardness of AMCD-HAP is greater than natural bone as the Vickers hardness of human natural bone is approximately 50 HV²¹⁹.

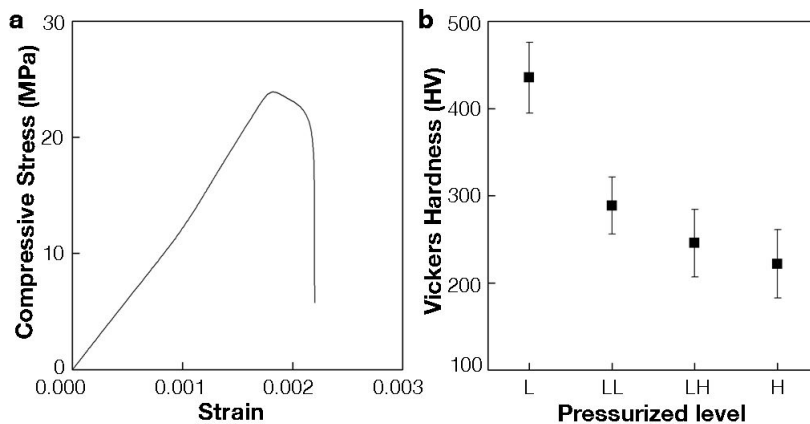


Figure 8.11 Mechanical strength of AMCD-HAP. **a**, True stress-strain curve of the well-aligned multiple channels with gradually decreasing diameter (AMCD) was measured by compression test. **b**, Micro-Vickers hardness was tested from each selected region of the Aligned Multiple Capillary networks with gradually decreasing Diameter-HAP (AMCD-HAP). Four regions were compared, ranging as a gradient from the highest (H) energy applied region to the lowest (L) applied energy (H: the highest, LH: lower than the highest, LL: lower still, and L: the lowest pressure area).

The gradual change in pore size and the connection of pores into networked channels is confirmed by three-dimensional reconstruction using SEM tomography of focused ion beam (FIB) dissected samples. For this analysis, as shown in Figure 8.10, we first divided an AMCD-HAP pellet into four segments corresponding to the pressure gradient during sintering (H: the highest pressure area; LH: lower than the highest; LL: lower still; L: the lowest energy area), then subjected each segment to FIB milling while SEM imaging it in 15 nm increments. Field-Emission SEM (FESEM)

images confirmed that the H section had mostly pores of diameter larger than micrometer scale (Figure 8.12).

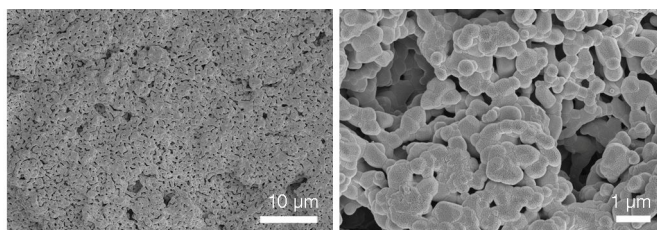


Figure 8.12 FESEM images of pores from the H (highest pressure) section, where pore diameters were approximately in the micrometer range.

Two different representative positions from areas that experienced different amounts of pressure (LH and LL) from the same AMCD-HAP sample were imaged at 15 nm intervals, as FIB milling proceeded along the pressure gradient. With two-dimensional SEM images obtained every 15 nm, a 3D reconstruction of the inner structure for the sample is created with imaging software (Amira). As seen clearly in the 3D reconstructed images in Figure 8.13, both LH and LL regions have nanopores connected by channels. The porosity in these regions was calculated with imaging software (Amira) and showed that there was a decrease in porosity with pressure from approximately 29.3% in the LH section to 10.9% in the LL section. Additionally, in 3D reconstruction, the connectivity of pores also can be identified from x, y and z axis scanning.

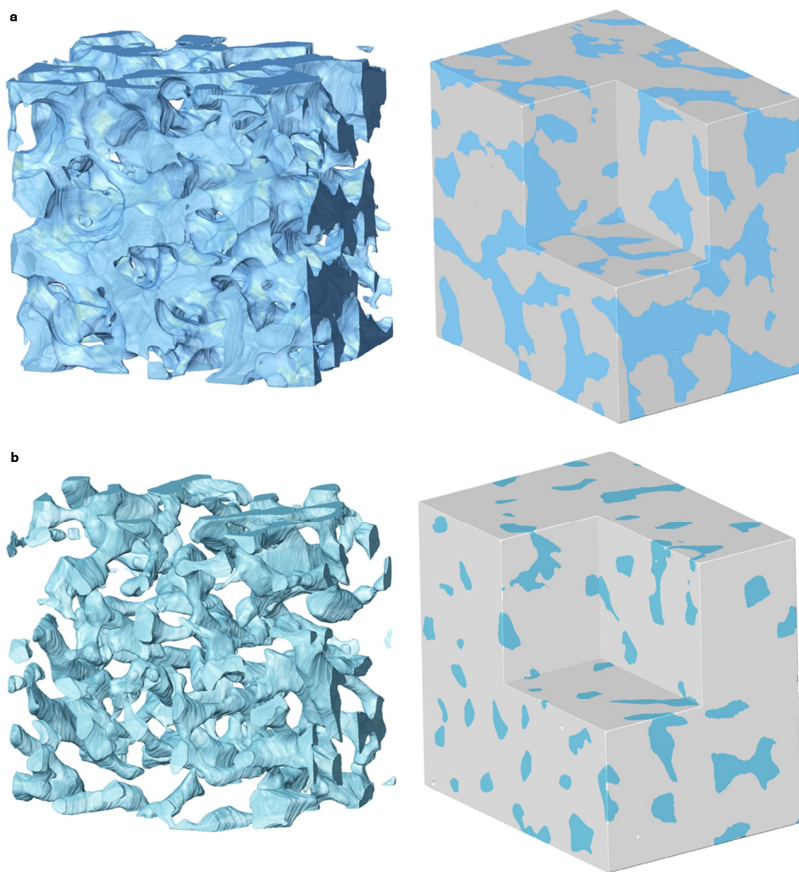


Figure 8.13 Reconstruction of nanochannels inside the scaffold. **a**, Three-dimensionally connected pore structures (blue) and scaffold (grey) from the LH section were reconstructed by FIB-FESEM tomography. **b**, Three-dimensionally connected pore structure (blue) and scaffold (grey) from the LL section were reconstructed by FIB-FESEM tomography.

This connectivity was further confirmed by Nano-scale X-ray Microscope and 3D reconstruction of synchrotron X-ray nanoimaging. Figure 8.14 is an enlarged view of our AMCD-HAP sample, observed by

ultra-nanoscale XRM (Nano-scale X-ray Microscope). Starting from the first image of the HAP scaffold, only the inner pore regions were reconstructed in three-dimensions for each subsequent image (Figure 8.14a). The resulting montaged image clearly shows pore dimensions that are at the nanometer scale. To demonstrate the connectivity of the pores within the AMCD-HAP sample, we used 3D analyzing software to identify the channel (Figure 8.14b). Using the 3D analysis software installed in ultra-nanoscale XRM, the pores' connectivity can be easily observed. Furthermore, how long the connected pores extended can be visually confirmed and measured by the 3D analysis software by measuring the volume of the pixels. Most pores were connected to each other and therefore belong to one of several interconnected groups of channels. These channels were spread throughout the whole sample and two largest interconnected channels occupied 32.9% and 30.6% of the total pore volume in the analyzed area, respectively. These channels are connected at the outside of tested region, making one large interconnected hierarchical channel. In conclusion, we showed that pores in AMCD-HAP are mostly connected to each other to form channels.

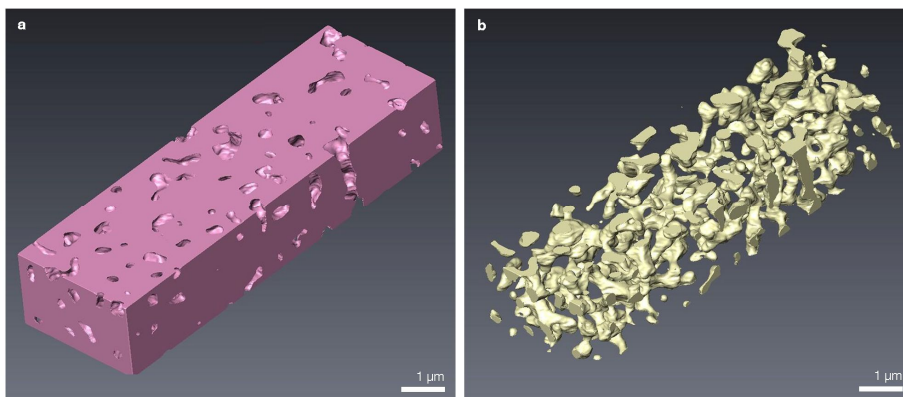


Figure 8.14 Reconstruction of nanochannel by Nano-CT. **a**, Montage of Ultra-XRM images reconstructing AMCD-HAP material (magenta color). **b**, Corresponding pore-channel structure (cream color) from the identical AMCD-HAP sample.

In addition, direct observations of the internal structure of our AMCD-HAP by ultra-XRM (Figure 8.15a) and synchrotron X-ray Nanoimaging (Figure 8.15b) analyses also support the existence of a structure that is composed of interconnected nanochannels.

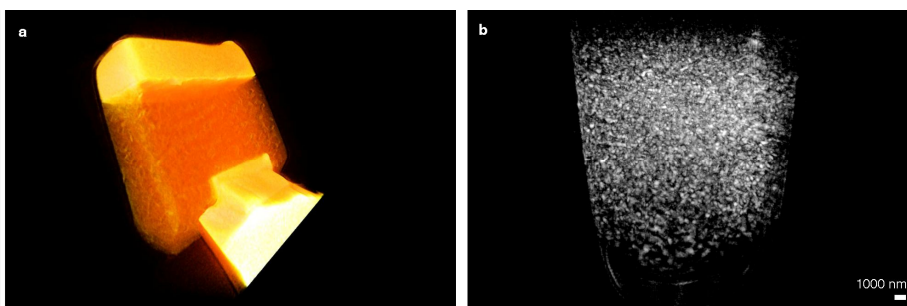


Figure 8.15 Internal structure of the AMCD-HAP pellet. Sample visualized

by: **a**, Ultra-XRM and **b**, synchrotron X-ray Nanoimaging. Void nanochannels are displayed in dark (a) and in white (b). In panel a, the light-yellow pseudo-colored area at the top and bottom is the sample holder and the orange pseudo-colored area is the AMCD-HAP sample.

For a direct visualization of nanochannels beyond the resolution limit of X-ray tomography and SEM, HRTEM analysis was also performed for the LL and L segments, as shown in Figure. 8.16a-b. TEM samples were prepared with FIB and placed on a 3 post Cu grid. The width of pores, visualized by the white contrast, was generally between 70 nm and 400 nm (Fig. 8.16a and See Figure. 8.17 and 8.18). The number of pores in a given area ($\cong 7.84 \times 3.04 \mu\text{m}^2$) is in the range of 40 ~ 50. It was also apparent that the shape of the pores is affected by the grain of the HAP. The grain size of HAP is roughly 300 ~ 1000 nm, which indicates growth from the initial 80 nm particles to this relatively larger grain size during the sintering. As shown in Figure. 8.16b, very narrow channels as small as 20 nm in width also exist and can be clearly seen in images from the L segment.

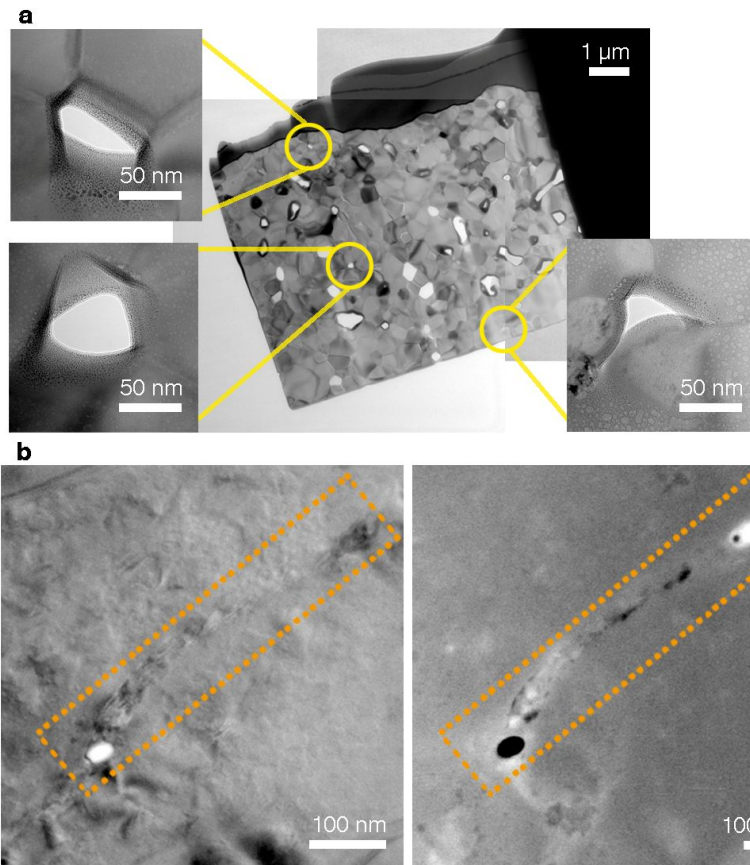


Figure 8.16 Electron microscopic characterization of AMCD-HAP. **a**, HRTEM images of pores, visualized as cross-sections of nanochannels from the LL section. **b**, HRTEM images from the L section. Nanochannel had approximately 20 nm width in both BF mode and STEM mode analysis.

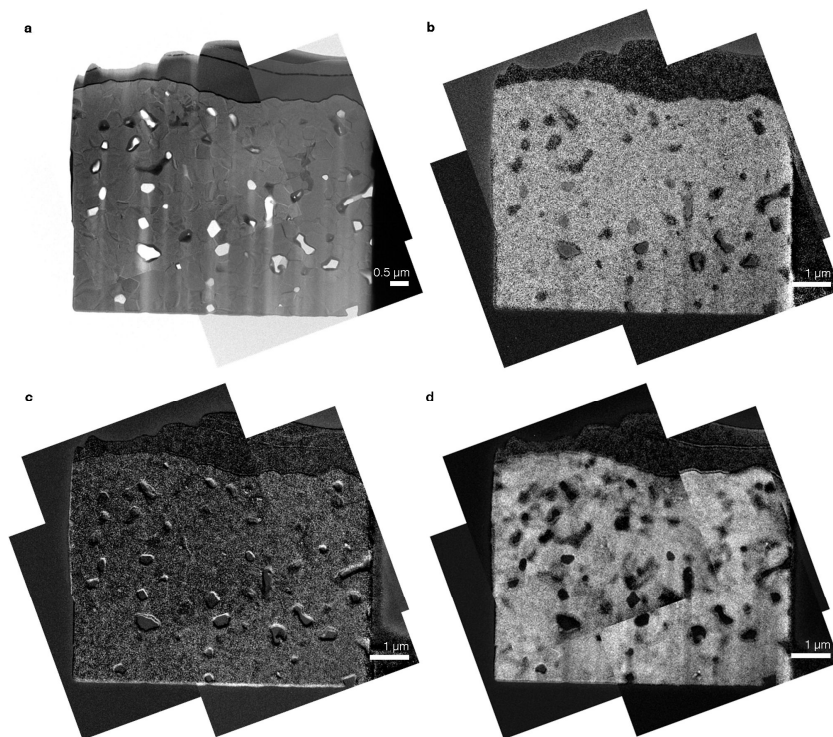


Figure 8.17 EELS mapping images of LL section from Figure 8.13a. **a**, Zero-loss image and elemental mappings of **b**, calcium, **c**, phosphate and **d**, platinum. The elemental mapping result showed that the pores in the LL section were void of any material. Therefore, we concluded that these pores were open and represented cross-sections of nanochannels.

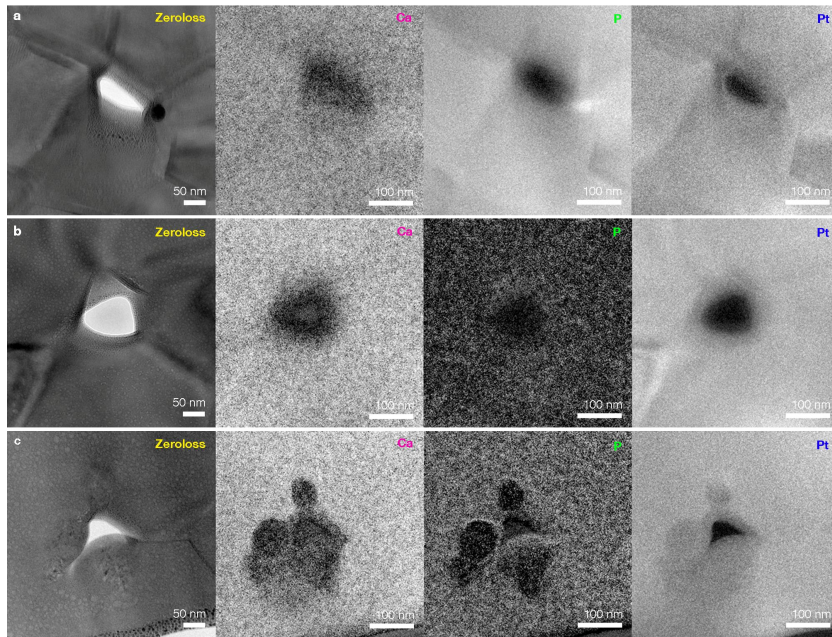


Figure 8.18 EELS mapping images of pores with nanometer dimension from Figure 8.15a. We mapped calcium, phosphate and platinum in the regions which were shown in the zero-loss images. **a-c**, Different nanopores from Figure 8.15a and Figure 8.16 were analyzed. The resulting mapping showed that pores were certainly open and not an optical illusion caused by the roughness of the samples. Therefore, we confirmed that these were cross-sections of nanochannels.

In addition, we also conducted similar experiment of giving gradual pressure energy during the sintering process with whitlockite (WH) and PEG hybrid material. By controlling the temperature condition (900 °C) of the sintering process or increasing the ratio between PEG and WH (1:2), we confirmed that this methodology can be generally applicable to other

materials. In Figure 8.19 and 8.20, altered porous conditions induced by different amount of pressurized level in an identical pellet made by WH-PEG hybrid material are shown. When the sintering temperature was controlled to 900 °C, while the mixing ratio between WH and PEG was 10:1, total pore areas of high pressurized region and low pressurized region were 9.37% and 5.74%, respectively. The average pore size of high pressurized area was 0.13 μm^2 while that of low pressurized area was 0.05 μm^2 . Each average pore radius was 0.20 μm for high pressurized part and 0.13 μm for low pressurized part. When the ratio between WH and PEG was controlled to 2:1 while the sintering temperature was set to at 1100 °C, there was also significant difference in porosity between the high pressurized region and the low pressurized region in the same sample. Total pore area, average pore size and average pore radius were measured as 2.43% versus 0.02%, 0.60 μm^2 versus 0.12 μm^2 and 0.44 μm versus 0.11 μm , respectively, for high pressurized part and low pressurized part.

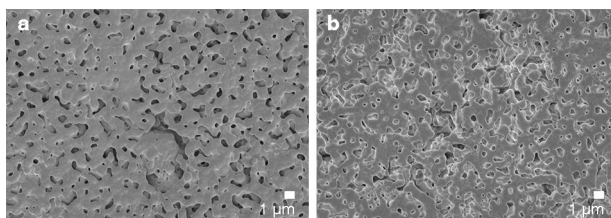


Figure 8.19 Tapered nanochannel in whitlockite (WH) made by controlling the sintering temperature at 900 °C. High pressurized region (a) of the WH-PEG pellet showed larger pore area, bigger pore size and more increased pore radius in average compare to the low pressurized region (b) of the identical WH-PEG pellet.

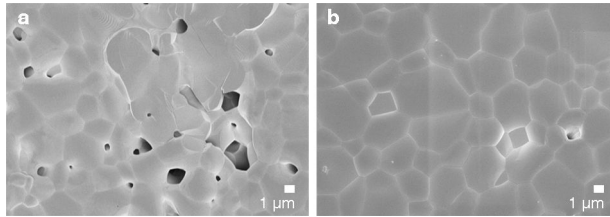


Figure 8.20 Tapered nanochannel in whitlockite made from controlling the ratio of the poly ethylene glycol (PEG) to whitlockite (WH) as 1:2. High pressurized part (a) of the WH-PEG pellet showed larger pore area, bigger pore size and more increased pore radius in average compare to the low pressurized part (b) of the same WH-PEG pellet

8.4 Capillary rise in arborized channels of a bioceramic

In conjunction with the effort to understand the inner structure of the new ceramic composite, the capability of the AMCD-HAP to draw fluid was tested. As a control, both nonporous HAP pellets and randomly porous HAP pellets, made from non-pressurized sintering processes, were tested and each showed no fluid transport. In contrast, the AMCD-HAP drew fluid very effectively from its reservoir at the base end of the pellet and delivered it to the upper surface located some 2 cm above the reservoir's fluid level. To visualize the interior capillary transport *in situ* and to assess the difference in fluid migration between the AMCD-HAP and the nonporous HAP pellets, ^{18}F -fluoro-deoxyglucose (FDG) positron emission tomography (PET) and computerized tomography (CT) scanning were performed (Figure 8.21).

Each pellet was placed vertically in a sterile container filled with distilled water containing ^{18}F -FDG and real-time images were acquired over a period of 60 minutes. In the AMCD-HAP pellet, FDG migrated through the aligned nanochannels of the pellet. In contrast, there was no migration of FDG in the nonporous conventional HAP pellet. Consistent with the physical geometries of aligned pore channels of varying diameters, the CT image analysis of the AMCP-HAP pellet showed a gradient of radiolucency along its length, and it was overall more radiolucent than the nonporous control pellet (Figure 8.22).

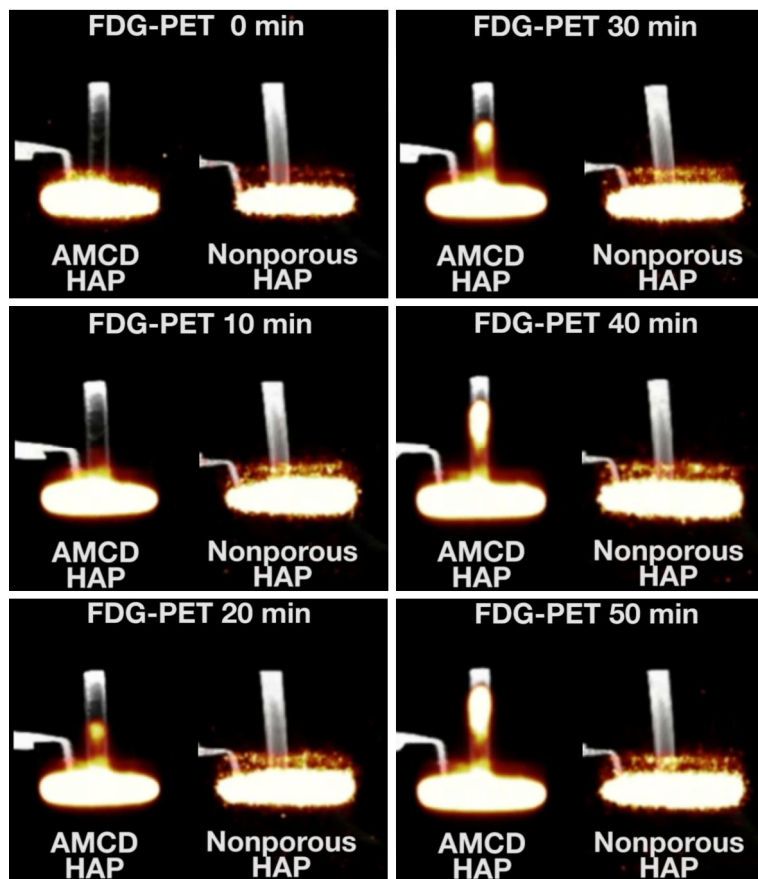


Figure 8.21 *in situ* FDG-PET imaging showed that the AMCD-HAP sample (left) exhibited a greater capillary force than a control nonporous HAP sample (right).

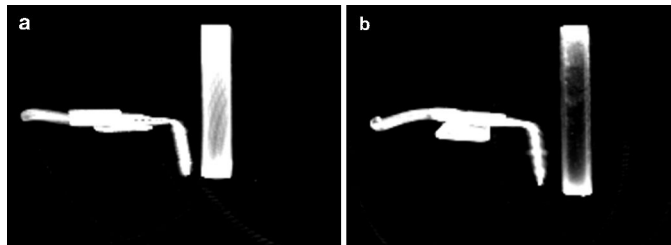


Figure 8.22 Computed tomography (CT) scanning of the inner hierarchy structure of the bone implant material. **a**, Reference solid HAP pellet showed almost no porous inner structure. **b**, AMCD-HAP pellet showed an inner structure with a gradient of porosity from bottom to top. Inner pore network was shown by darkness contrast. The dark black area at the bottom showed that pores were abundant. Light grey area at top showed that the abundance of pores decreased.

For further quantitative comparison, as shown in Figure 8.23a, AMCD-HAP, nonporous HAP, and randomly porous HAP samples were partially immersed in water in which a dye was dispersed to permit visualization of fluid flow. The rise of the dye-colored water was monitored and measured. The AMCD-HAP pellets, with their upwardly directed and narrowing channels, showed the fastest and the highest fluid rise (Figure 8.23b). When they were placed in an inverted position, with the channels widening towards the top, they also drew water but at a slower rate and to a lower height. There was no water rise in the nonporous or randomly porous HAP pellets. Further tests were conducted on samples engineered to have different porosities, created with different amounts of PEG and variable PEG chain lengths. The results in Figure 8.23c showed that the samples

containing larger amounts of PEG before sintering exhibited a greater capillary rise due to their greater porosity after sintering. In addition, by varying the molecular weight of the PEG polymer from 400 to 600,000 g/mol, we were able to establish a linear relationship between the molecular weight of the polymer and the amount of capillary rise in the resulting AMCD-HAP pellets (Figure 8.23d). We attribute this correlation to the fact that PEG entangles more with itself and therefore agglomerates more when its molecular weight is larger^{208,210,211}. However, this result only holds for samples subjected to our pressurized sintering process; if the HAP-PEG mixture was sintered without additional pressure, the resulting pellets showed only small variation in porosity over a wide range of PEG molecular weight (Figure 8.24).

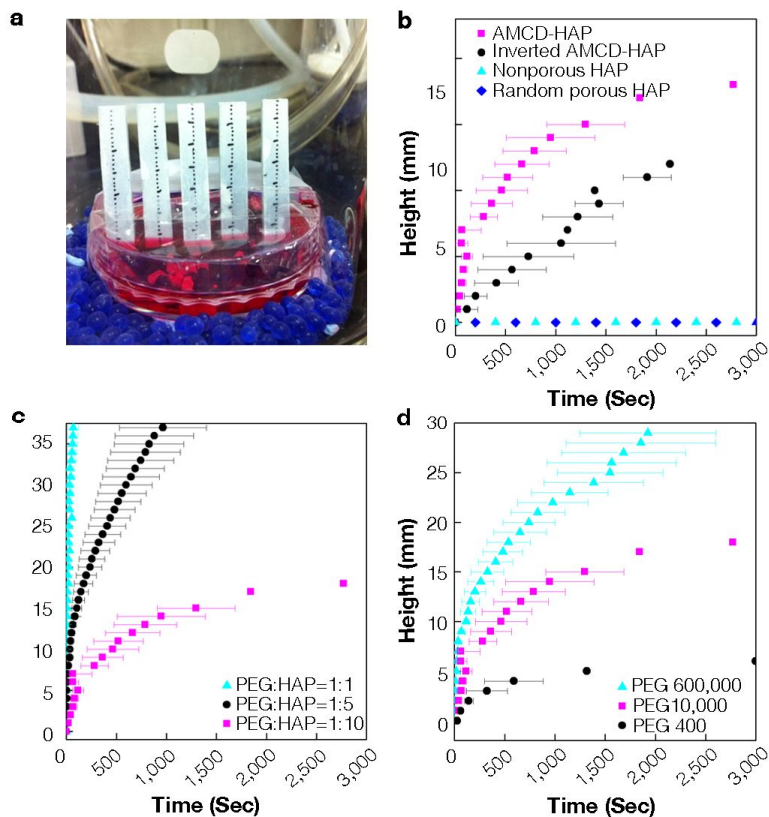


Figure 8.23 Capillary rise of AMCD-HAP. **a**, Capillary test of AMCD-HAP sample conducted under constant temperature and humidity. **b**, AMCD-HAP sample (magenta square), inverted orientation of AMCD-HAP sample (black circle), nonporous HAP sample made from HAP/PEG at a ratio of 1/10,000 by weight (cyan triangle) and randomly porous HAP samples made from HAP/PEG at a ratio of 1/10 by weight (blue diamond) were compared for their abilities to draw fluid by capillary force in real time. **c**, Comparison of capillary rise height among HAP samples sintered with different ratios of PEG polymer. PEG:HAP = 1:10 (magenta square), PEG:HAP = 1:5 (black circle), PEG:HAP = 1:1 (cyan triangle). **d**, Comparison of capillary rise

height among HAP samples sintered with different molecular weights of PEG polymer. PEG MW 400 g/mol (black circle), PEG MW 10,000 g/mol (magenta square), PEG MW 600,000 g/mol (cyan triangle).

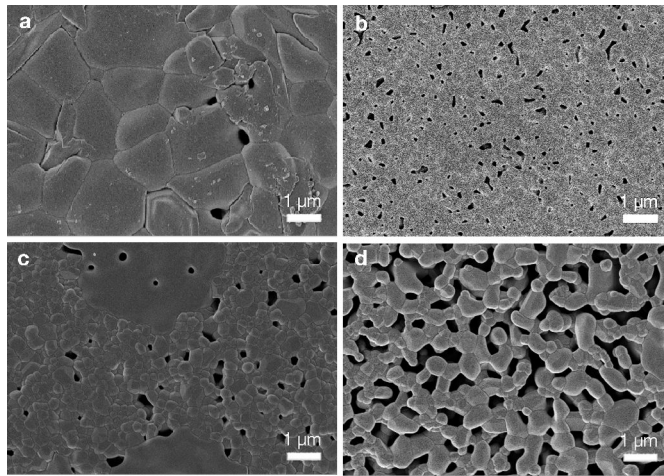


Figure 8.24 Porosity of the PEG-HAP pellet depending on the molecular weight of PEG and applied pressure level during sintering process. **a**, FESEM image of HAP and PEG 2,000 mixture after conventional sintering without pressurization. **b**, FESEM image of HAP and PEG 600,000 mixture after sintering without pressurization. **c**, FESEM image of HAP and PEG 2,000 mixture after sintering under pressure. **d**, FESEM image of HAP and PEG 600,000 mixture after sintering with pressurization. Chain length and pressure level are both important factors affecting phase separation. **a-b**, When the molecular weight of PEG was higher, the porosity of the HAP-PEG mixture increased slightly after conventional sintering. **c-d**, Pressure exerts a more important influence on porosity than polymer molecular weight, as the porosity observed became significantly greater after sintering under pressure.

8.5 Nutrient supply for the living organisms by AMCD

Based on these findings, we hypothesized that the AMCD-enabled HAP composite could mimic the vascular supply of nutrients provided by the terminal capillary network of natural hard tissues found in biological systems. Among the circulatory systems of living organisms, bone is known for having a design that utilizes hierarchically organized tubes and gradually tapered channels to supply nutrients and growth factors to its resident cells. Alterations to this intrinsic hierarchy for internal transport can pose a challenge when bone must be fitted with an implant. Some bone implant materials fail to support cell growth when circulation is impaired due to a compromised interface between the implant material and the natural host bone²²⁰⁻²²². To overcome this clinical limitation of bone implants, and in addition to millimeter or micrometer channels that are molded or machined into implants for fluidic conduction, surgeons have identified the need for future implant designs to incorporate nanoscale structure to promote circulation²²³⁻²²⁵. Therefore, it seemed natural to speculate that our AMCD-enabled HAP can address these issues and be used as a future bone implant material with a built-in, self-powered capillary transport network to support bone cell growth and differentiation at the interface with the host tissue.

In pursuit of this vision, we attempted to test whether AMCD-HAP blocks can indeed support the metabolism of living cells by efficiently supplying fluids and nutrients along the length of the material from a source located at the other end. To this end, we tested the survival, growth and differentiation of mammalian cells grown on one surface of the AMCD-HAP pellets, centimeters away from the media fluid reservoir. In these tests, an

AMCD-HAP pellet was placed standing vertically up (nanochannels narrowing towards the top) in a sterile container filled with cell culture media, along with a non-porous, but otherwise identical control HAP pellet, for comparison. Human-derived osteoblast cells (Lonza Clonetics) were seeded on the top surface of each pellet at a density of 1×10^5 cells/ml, where the surface area was approximately $7 \text{ mm} \times 2 \text{ mm}$. Containers were tightly sealed to prevent evaporative transport and maintained at $37 \text{ }^\circ\text{C}$ in an atmosphere of $5\% \text{ CO}_2$. The top surface of the HAP pellet upon which the osteoblast cells were seeded was approximately 1 cm above the nutrient media, as illustrated in Figure 8.25a. In this geometry, the osteoblast cells were maintained at the humidified air interface, with the only source of nutrients being drawn through the AMCD-HAP capillary channels over a distance of 1 cm. After variable culture periods, the nuclei and actin cytoskeleton fibers were stained with DAPI and phalloidin, respectively, and the cells were observed using fluorescence microscopy. As shown in Figure 8.25b, the surface of the AMCD-HAP pellet showed vigorous osteoblast cell growth, whereas no osteoblast cells survived on the nonporous HAP pellet.

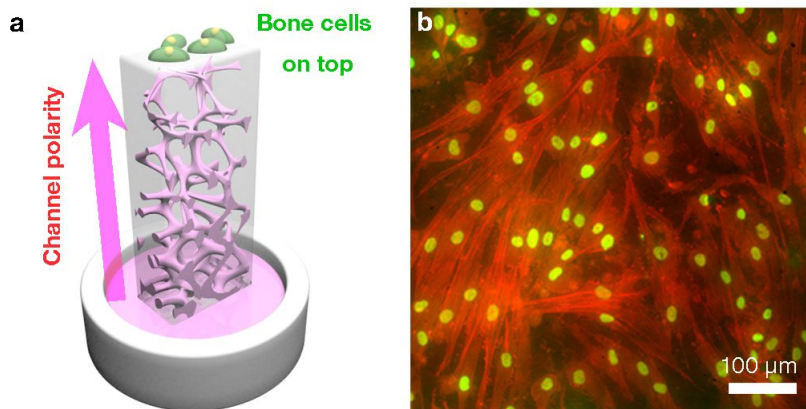


Figure 8.25 Human osteoblast cells grown on AMCD-HAP ceramic material. **a**, Schematic representation of the method of seeding human osteoblasts onto the top surface of AMCD-HAP samples. **b**, After 1 week, osteoblasts were observed growing on the surface of the HAP samples, as shown by fluorescence microscopy.

To ascertain that human bone cells grown on the capillary-delivery surface of the AMCD-HAP pellet not only survive, but also maintained their differentiated phenotype for bone matrix production, the gene expression profiles for several bone-related proteins were assayed and compared to human osteoblast cells grown on the submerged nonporous HAP, as described in Figure 8.25a. Messenger RNA (mRNA) levels were estimated using the standard technique of reverse transcription of mRNAs to complementary DNA strands followed by real time quantitative PCR analysis (RT-qPCR). Using this approach, the relative abundance of the mRNAs for selected bone matrix genes were quantified as shown in Figure 8.26. After 48 hours of cell growth depending solely on nanochannel supply,

we found that the mRNAs for bone matrix-related proteins were actively expressed and had expression levels comparable to those of osteoblasts grown on the submerged nonporous HAP surface. The data from the RT-qPCR analysis indicated that the microenvironment created at the AMCD-HAP surface supported osteoblast cell function in a manner equivalent to the bone cells maintained on submerged, nonporous HAP material.

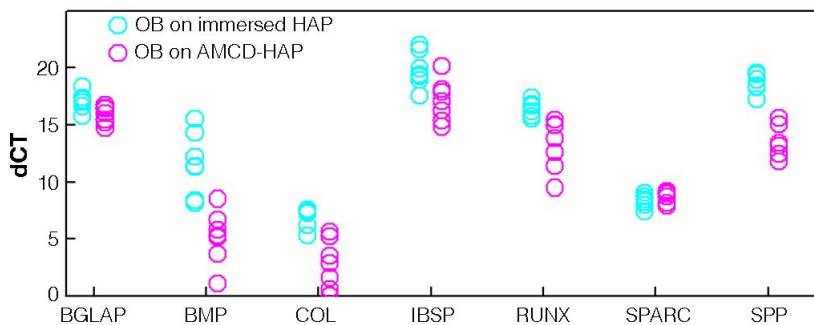


Figure 8.26 Relative gene expression measured by quantitative real time PCR revealed that osteoblasts grown on top of AMCD-HAP samples (magenta, n = 7) expressed similar levels of bone-related genes compared to the expression profile for osteoblasts grown on fully immersed HAP samples (cyan, n = 7).

We also conducted another nutrient supply experiment in which the cyanobacteria, *Synechococcus elongatus* Nägeli (ATCC 33912), were grown on top of AMCD-HAP surface for 10 days where the bacteria are dependent on only nanochannel capillarity for exchange of nutrients. Figure 8.27a shows these cyanobacteria proliferating on top of the AMCD-HAP pellet, while no cyanobacteria exist on the top surface of a solid HAP pellet Figure

8.27b. Moreover, the lateral surfaces of the AMCD-HAP pellet provide sufficient exchange of media to support the growth of a few cyanobacteria along the sides of the AMCD-HAP pellet (Figure 8.27c). Seemingly, so long as there is a regular supply of media, bacteria survive. For this experiment, cyanobacteria cultures at the log phase of growth ($OD_{730} = 0.7$) were collected and seeded on the top surface of the AMCD-HAP pellet. The container was sealed tightly to retain humidity, and maintained in an incubator at 30 °C under 2000 lux light. During the culture period of 10 days, the pellets were partially immersed in BG-11, supplemented with 10 mM of HEPES medium, yet the top of the pellet was > 1 cm above the media meniscus. After 10 days of culture, bacteria were observed by optical microscopy.



Figure 8.27 Bacterial growth atop the AMCD-HAP pellets. **a**, Cyanobacteria (green) grown on atop the AMCD-HAP pellet depend solely on a supply power of nutrients supplied by the nanochannels. **b**, No cyanobacteria survive on atop of nonporous HAP pellet in condition identical with those shown in Figure 8.25a. **c**, Cyanobacteria grow on the lateral surface of the AMCD-HAP where transport is sufficient to provide for otherwise unpowered nutrient exchange.

8.6 Summary

Looking towards the future, one can envision this study paving way for the next generation of bone implants, which could become ‘alive’ with their built-in hierarchical networks of biocapillary-like supply. While incorporating AMCD-HAP into bone implants stands out as an attractive possibility, the findings in this work could have a broader impact in other areas as well, such as lubrication in ceramic motors, fuel transport and energy conversion^{226,227}. Furthermore, it is known that living organisms metabolize most efficiently when resources are distributed throughout their tissues by a fractal network, resulting in minimal energy dissipation⁴⁰. In our research, networks of gradually tapering nanochannels showed similarly distributed and self-powered supply for bone cells to proliferate and maintain their specialized gene expression profile. This work also introduced a novel and reproducible manufacturing technique for constructing such networked capillaries within a ceramic biomaterial making use of pressure-gradient induced differentiations to phase-segregation between PEG and HAP and their solid-liquid and liquid-vapor phase-transitions.

Chapter 9. Concluding remarks

9.1 Summary

In this thesis, in order to comprehend formation mechanism and function of the bone in living system, we investigated new methodologies to control composition and structure of biomineral based on multi-disciplinary efforts that imparts the concept of material science engineering, chemistry, physics and biology. We tried to provide our foundation technologies with detailed scientific information in order to inspire and induce subsequent studies of other researchers to further reveal unknown mechanisms in our body system.

In the first half of this thesis, we presented easy synthesis of whitlockite (WH: $\text{Ca}_{18}\text{Mg}_2(\text{HPO}_4)_2(\text{PO}_4)_{12}$), the second abundant biomineral in bone tissue, in the physiologically relevant $\text{Ca}(\text{OH})_2\text{-Mg}(\text{OH})_2\text{-H}_3\text{PO}_4$ aqueous system because its formation mechanism and contribution in our body system is unknown. We showed systematic approach to find unusual precipitation condition of WH from its theoretical composition, by analyzing stability of synthetic analogue TCP material after Mg^{2+} incorporation and chemical structure of WH, which include HPO_4^{2-} . By controlling accurate ratio between Ca, Mg and P under excess Mg^{2+} and proton condition, we successfully synthesized pure phase of WH nanoparticles in gram-scale. Our synthesized WH had distinct feature to TCP from its clear existence of HPO_4^{2-} in its chemical structure. Notably, we figured out that stability of WH is higher than HAP under pH 4.2, which can be important key to understand mechanism of formation of WH in our body system.

In order to comprehend formation mechanism of WH in our body system, we analyzed kinetic mechanism of precipitation of WH in Ca(OH)₂-Mg(OH)₂-H₃PO₄ aqueous system in detail. During our experiment system, H₃PO₄ was added by dropwise into Ca(OH)₂-Mg(OH)₂ aqueous solution which made transitions of pH from base to acid in surrounding system of the precipitant. As soon as small droplet of H₃PO₄ was inserted in the Ca(OH)₂-Mg(OH)₂ solution, protons rapidly reacted with Ca²⁺ and Mg²⁺ in basic pH condition which encouraged the formation of HAP, the thermodynamically stable compound above neutral pH. Finally, when the addition of H₃PO₄ was completed, the pH of the whole system turned into approximately pH 3.3 which induced dissolution of former HAP phase and recrystallization of WH structure based on Mg²⁺. This shed new light on the possible formation mechanism of WH in our body system that it can also be occurred from acidic microenvironment by assistant of secondary ions such as Mg²⁺ and explains why WH exist in short-range distance in body system.

We also evaluated biocompatibility of WH compare to well-known HAP and TCP materials by cellular proliferation level and activity state related to bone mineralization. Notably, under the fabrication condition of this thesis, WH provided better condition as a cell scaffold and showed better proliferation level of human osteoblast cells than that of HAP or TCP. In addition, bone cells grown on WH scaffold were active in bone mineralization process as much as that of HAP, in both RNA and protein levels. WH was also be able to resorbed by osteoclast cells, while previous TCP was known to be too soluble and thus could not be resorbed by natural osteoclast activity. Taken all together, basic *in vitro* test results confirmed WH as an excellent biomaterial, comparable to HAP.

Based on our findings, we conducted some experiments to investigate available functions of WH for future applications as a biomineral, such as implants and toothpaste. We fabricated WH into porous implant and cylindrical implant for general *in vivo* test, according to its mechanical properties. Notably, we found that WH had exceptional mechanical strength compare to that of commercial HAP and TCP. In addition, WH nanoparticles were capable to coexist with free fluoride ions and thus indicating the possibility to overcome previous limitations of toothpastes composed of HAP or TCP, for efficient remineralization process of tooth. We also introduced scale-up technology for the rapid produce of WH, by addition of hydrogen peroxide as a green catalyst, which can stimulate fast nucleation of WH. Based on these findings, we expect WH can be easily utilized in various industrial applications.

In the latter half of the thesis, inspired from the interior structures of hard materials from the nature, including bone, we designed and presented novel method to induce tapered nanochannels in bioceramic in long distance ($> \text{cm}$). We gave additional pressure energy during sintering process to induce phase separation between organic and inorganic materials. By continuously varying the pressure level, we made interconnected porous network with its diameter of channel changing from micrometer scale to nanometer scale. Notably, aligned multiple channel with decreasing its diameter (AMCD) showed better capillarity compare to channel with constant diameter or inverted AMCD. Moreover, we proved that living organisms such as cells or bacteria could sustain their lives solely by the supply power of the nanochannels. This is the first achievement to build long range of tapered nanochannels in bioceramic, although these structures are

already naturally existed. We believe that our findings will contribute to reveal the effect and the role of the nanochannels in living system, especially from their exceptional properties induced from small scale.

9.2 Further suggested research ideas

In this study, we showed synthesis condition and precipitation mechanism of WH in simplified $\text{Ca}(\text{OH})_2\text{-Mg}(\text{OH})_2\text{-H}_3\text{PO}_4$ aqueous system, but more profound study should be continued to discover the formation mechanism of WH in the actual *in vivo* system. In addition, the function of WH should be revealed related to the HAP, as these two phases are the main components of bone mineral. Then, along with scientific investigation, based on easy synthesis method of WH, it can also be applied in various fields including previous areas of HAP and TCP. We already briefly introduced about possible applications of WH related to bone implant and toothpaste. Further *in vivo* test will verify the effect of WH as an implant material compare to that of HAP and TCP. In addition, more advanced research with remineralization capability of WH should be conducted to evaluate WH as a toothpaste component.

In addition, deeper investigations are required with tapered nanochannels to understand its properties related with nanometer scale and directionality. Incorporation of capillary supply networks into a bone-implant composite has been shown in our study to enable sustained bone-cell growth at the designated surfaces or local sites, thus making the composite 'alive'. Whereas the bio-functionality of this structure was proven effective

as designed, its mechanical property was not simple to predict because of the structural complexity and the dissimilarity in features which is relevant with our bone with anisotropic orientation of interconnected pore network. In this respect, bioceramic scaffold with built-in nanochannels with directionality can be used as a convenient experiment platform to analyze directionality effect and thus illuminate cause of the structure of the natural bone. In addition, until now, researches related to comprehending mechanical behaviors in nanometer scale have not been fully developed because of limited technology to fabricate tapered nanochannels in inorganic material. Therefore, our nanochannel structure will provide opportunities to reveal the mechanical behavior of our bone with its structure in nanometer scale. While our research may be viewed as a first step to meet the ‘living composite’ paradigm challenge in material research, we expect that our present result can eventually be developed to contribute for efficient circulations in bio-composite and load-bearing joints, robotics, and aircraft valves by powerful supplying design. We also believe the composite with built-in capillary network structures to exhibit superior mechanical and thermal properties that could be tailored for incorporation of distributed autonomous lubrication and/or cooling in ceramic devices and components for light-weight extreme temperature chemo-corrosion-EM resistant operations (micro-machines, robotics, aircraft valves, and embedded electronics), while also maximizing the strength/weight ratio.

초 록

자연계에 존재하는 단단한 재료 중에서 특히 골과 같은 생물의 경조직은 열역학적으로 가장 안정한 형태의 상에 속하는 나노 입자들이 자가조립에 의해 계층적 질서를 이루면서 정렬되어 있다. 이에 고무되어 인공적으로 구현한 재료들은 마이크로미터 범주까지는 자연계의 물질과 유사한 특성을 보이며 다양한 분야에서 활용되어 왔지만, 나노미터 범주에서는 아직까지 충분한 연구가 진행되지 않은 상태이다. 따라서 본 논문에서는 자연계 물질에 대한 이해 및 모사를 위해서 나노미터 범주에서의 새로운 조성 및 구조와 관련된 연구를 진행하여 추후에 연계될 수 있는 관련 연구 분야의 과학적 기반을 제공하고자 하였다.

논문의 전반부에서는 골 성분과 유사한 조성을 개발하기 위하여, 하이드록시 아파타이트 (hydroxyapatite: $\text{Ca}_{10}(\text{PO}_4)_6(\text{OH})_2$) 와 더불어 생체 내 무기물질 중에서 가장 많이 존재하는 상인 휘트라카이트 (whitlockite: $\text{Ca}_{18}\text{Mg}_2(\text{HPO}_4)_2(\text{PO}_4)_{12}$)에 대한 연구를 소개하였다. 기존의 골 임플란트에 대한 연구는 주로 하이드록시 아파타이트를 이용하여 진행되어 왔는데, 그 이유는 생리학적 환경과 유사한 조건에서 휘트라카이트의 합성법이 잘 정립되지 않았기 때문이다. 본 논문에서는 $\text{Ca}(\text{OH})_2\text{-Mg}(\text{OH})_2\text{-H}_3\text{PO}_4$ 를 출발 원료로 하여 수용액 환경에서 대량으로 단일상의 휘트라카이트 나노입자를 얻는 방법을 체계적으로 서술하였다. 또한 합성된 휘트라카이트를 유사 물질인 트리칼슘포스페이트 (tricalcium phosphate:

$\text{Ca}_3(\text{PO}_4)_2$ 와 비교해가면서 재료적 물성에 대해 평가하였다. 그리고 생체 내에서 휘트라카이트가 형성되는 과정을 이해하기 위해서 합성이 진행되는 동안의 동역학적 과정에 대해서 분석하였으며, 그 결과 중성 이상의 pH 환경에서 안정적인 하이드록시 아파타이트가 산성 영역에서 녹으면서 Mg^{2+} 와 HPO_4^{2-} 를 중심으로 Ca^{2+} , PO_4^{3-} 가 새롭게 안정한 휘트라카이트 구조를 형성하는 것을 확인하였다. 특히, 휘트라카이트는 *in vitro* 환경에서 임플란트 재료로 이미 널리 사용되고 있던 하이드록시 아파타이트와 트리칼슘포스페이트 이상으로 높은 세포 증식률을 보였으며, 휘트라카이트 표면에서 자란 골 세포들은 골 형성과 관련된 활동을 활발하게 진행하여 좋은 생체 적합성을 보였다. 또한 이 외에도 휘트라카이트는 하이드록시 아파타이트와 트리칼슘포스페이트에 비해서 강한 기계적 물성에 가져서 여러 가지 형태의 임플란트로 가공할 수 있는 용이성과 치약 재료와 같은 다양한 생체 재료로써의 응용 가능성을 보여 실제로 여러 분야에 적용할 수 있는 큰 잠재성을 나타내었다.

논문의 후반부에서는 골과 유사한 구조를 나노미터 단위에서 구현하기 위하여, 하이드록시 아파타이트 내부에 직경이 나노미터에서 마이크로미터로 연속적으로 변화하는 나노채널을 형성하였다. 나무 구조와 유사한 나노 기공 연결망은 모세관 현상을 극대화시키며 가장 효율적인 순환체계를 형성한다고 알려져 있는데, 특히 폭이 점차 가늘어지는 채널의 경우에 넓은 직경의 도입 부분은 투과력에 유리하며 전체 유속을 빠르게 할 수 있다는 장점을 갖는다. 본 논문에서는 열처리를 하는 동안 추가적인 압력에너지를 가해주어 폴리에틸렌글라이콜 (polyethylene glycol)

고분자와 하이드록시 아파타이트 나노입자 사이의 상분리를 유도하였으며, 특히 압력에너지를 점진적으로 가해주어서 상분리의 정도가 다르게 일어나도록 유도하여 나노채널의 직경을 변화시켰다. 이렇게 형성된 직경이 점차 좁아지는 나노 채널 (Aligned Multiple Capillary networks with gradually decreasing Diameter)은 FIB-FESEM, TEM, Nano-CT 분석을 통해서 나노미터 단위에서 연속된 기공망으로 이어져 있는 것으로 직접적으로 확인되었다. 또한 나노채널의 좁아지는 방향이 유체를 공급하는 방향과 일치할 때, 역방향에 비해서 모세관 현상이 더 우세한 것을 검증하였다. 무엇보다도 세포와 박테리아와 같은 작은 생명체를 나노채널 끝에서 자라게 하였을 때, 단지 나노채널을 통해 공급되는 영양분에만 의존해서 생명을 유지할 수 있는 것을 보여주어 생명체에서 나노채널이 갖는 중요성에 대해 확인하였다.

본 논문에서 제시한 나노미터 단위에서의 조성 및 구조에 대한 연구는 자연계에 존재하는 단단한 재료의 생성 메커니즘과 생명 활동에 기여하는 역할을 이해하는 데 도움이 되리라 본다. 그리고 앞으로 보다 생체 골과 유사한 재료를 구현하는 데 직접적으로 이바지 할 것으로 전망하며, 생체 재료 분야 이외에도 나노미터 규모와 관련된 다양한 연구 분야에 기반이 되리라 기대된다.

주요어: 칼슘 포스페이트, 바이오미네랄, 휘트라카이트, 나노 채널,
골, 임플란트

학 번: 2010-30784

Bibliography

- 1 Driessens, F. C. M. & Verbeeck, R. M. H. *Biominerals*. (CRC PressINC, 1990).
- 2 Elliott, J. C. *Structure and Chemistry of the Apatites and Other Calcium Orthophosphates*. (Elsevier Science & Technology, 1994).
- 3 Hannig, M. & Hannig, C. Nanomaterials in preventive dentistry. *Nature Nanotechnology* **5**, 565-569 (2010).
- 4 Colfen, H. Biomineralization: A crystal-clear view. *Nature Materials* **9**, 960-961 (2010).
- 5 Jackson, S. F. & Randall, J. T. The Fine Structure of Bone. *Nature* **178**, 798-798 (1956).
- 6 Traub, W., Arad, T. & Weiner, S. Three-dimensional ordered distribution of crystals in turkey tendon collagen fibers. *Proceedings of the National Academy of Sciences* **86**, 9822-9826 (1989).
- 7 Hartgerink, J. D., Beniash, E. & Stupp, S. I. Self-assembly and mineralization of peptide-amphiphile nanofibers. *Science* **294**, 1684-1688 (2001).
- 8 Weiner, S. & Wagner, H. D. The material bone: structure-mechanical function relations. *Annual Review of Materials Science* **28**, 271-298 (1998).
- 9 Brookes, M., Elkin, A., Harrison, R. & Heald, C. A new concept of capillary circulation in bone cortex: some clinical applications. *The Lancet* **277**, 1078-1081 (1961).
- 10 Dickson, K., Bergeron, J., Philip, A., O'Connor-McCourt, M. & Warshawsky, H. Localization of specific binding sites for ¹²⁵I-TGF-β1 to fenestrated endothelium in bone and anastomosing capillary networks in enamel organ suggests a role for TGF-β1

- in angiogenesis. *Calcified Tissue International* **68**, 304-315 (2001).
- 11 Calvo, C. & Gopal, R. The crystal structure of whitlockite from the Palermo Quarry. *American Mineralogist* **60**, 120-133 (1975).
- 12 Frondel, C. Whitlockite: a new calcium phosphate, $\text{Ca}_3(\text{PO}_4)_2$. *American Mineralogist* **26**, 145-152 (1941).
- 13 Ionov, D. A. *et al.* Discovery of whitlockite in mantle xenoliths: Inferences for water- and halogen-poor fluids and trace element residence in the terrestrial upper mantle. *Earth and Planetary Science Letters* **244**, 201-217 (2006).
- 14 Sha, L.-K. Whitlockite solubility in silicate melts: some insights into lunar and planetary evolution. *Geochimica et Cosmochimica Acta* **64**, 3217-3236 (2000).
- 15 Lagier, R. & Baud, C. A. Magnesium Whitlockite, a Calcium Phosphate Crystal of Special Interest in Pathology. *Pathology - Research and Practice* **199**, 329-335 (2003).
- 16 Scotchford, C. A., Vickers, M. & Yousuf Ali, S. The isolation and characterization of magnesium whitlockite crystals from human articular cartilage. *Osteoarthritis and Cartilage* **3**, 79-94 (1995).
- 17 Hayashi, Y. High-resolution electron microscopy of mineral deposits on a thin layer of pellicle adhering to intact enamel surface. *Journal of Electron Microscopy* **45**, 501-504 (1996).
- 18 Palamara, J., Phakey, P. P., Rachinger, W. A. & Orams, H. J. Electron microscopy of surface enamel of human unerupted and erupted teeth. *Archives of Oral Biology* **25**, 715-725 (1980).
- 19 Meinke, D. K., Skinner, H. C. W. & Thomson, K. S. X-ray diffraction of the calcified tissues in *Polypterus*. *Calcified Tissue International* **28**, 37-42 (1979).

- 20 Quint, P., Althoff, J., Hohling, H. J., Boyde, A. & Laabs, W. A. Characteristic molar ratios of magnesium, carbon-dioxide, calcium and phosphorus in the mineralizing fracture callus and pre-dentine. *Calcified Tissue International* **32**, 257-261 (1980).
- 21 Albee, A. & Chodos, A. A. Microprobe investigations on Apollo 11 samples. *Geochimica et Cosmochimica Acta Supplement* **1**, 135 (1970).
- 22 Neal, C. R. & Taylor, L. A. Evidence for metasomatism of the lunar highlands and the origin of whitlockite. *Geochimica et Cosmochimica Acta* **55**, 2965-2980 (1991).
- 23 Jolliff, B. L., Haskin, L. A., Colson, R. O. & Wadhwa, M. Partitioning in REE-saturating minerals: Theory, experiment, and modelling of whitlockite, apatite, and evolution of lunar residual magmas. *Geochimica et Cosmochimica Acta* **57**, 4069-4094 (1993).
- 24 Hsu, W. Rare earth element geochemistry and petrogenesis of ilmenite (Ilm) silicate inclusions. *Geochimica et Cosmochimica Acta* **67**, 4807-4821 (2003).
- 25 Vankemenade, M. & Debruyne, P. L. A kinetic study of precipitation from supersaturated calcium phosphate solutions. *Journal of Colloid and Interface Science* **118**, 564-585 (1987).
- 26 Terpstra, R. & Driessens, F. Magnesium in tooth enamel and synthetic apatites. *Calcified Tissue International* **39**, 348-354 (1986).
- 27 Kumar, R., Prakash, K. H., Cheang, P. & Khor, K. A. Temperature driven morphological changes of chemically precipitated hydroxyapatite nanoparticles. *Langmuir* **20**, 5196-5200 (2004).
- 28 Prakash, K. H., Kumar, R., Ooi, C. P., Cheang, P. & Khor, K. A. Apparent solubility of hydroxyapatite in aqueous medium and its influence on the morphology of nanocrystallites with pre-

- precipitation temperature. *Langmuir* **22**, 11002-11008 (2006).
- 29 Damien, C. J. & Parsons, J. R. Bone graft and bone graft substitutes: A review of current technology and applications. *Journal of Applied Biomaterials* **2**, 187-208 (1991).
- 30 Gross, K. A. & Berndt, C. C. Biomedical application of apatites. *Reviews in mineralogy and geochemistry* **48**, 631-672 (2002).
- 31 Yamagishi, K. *et al.* Materials chemistry: a synthetic enamel for rapid tooth repair. *Nature* **433**, 819-819 (2005).
- 32 Niwa, M. *et al.* Polishing and whitening properties of toothpaste containing hydroxyapatite. *Journal of Materials Science: Materials in Medicine* **12**, 277-281 (2001).
- 33 Redbord, K. P., Busso, M. & Hanke, C. W. Soft-tissue augmentation with hyaluronic acid and calcium hydroxyl apatite fillers. *Dermatology and Therapy* **24**, 71-81 (2011).
- 34 Rigano, L., Lionetti, N., Gazzaniga, G., Rastrelli, F. & Bonfigli, A. A new biologically compatible physical sunscreen with skin firming properties. *SÖFW Journal* **135**, 20 (2009).
- 35 Roy, M., Vamsi Krishna, B., Bandyopadhyay, A. & Bose, S. L. Laser processing of bioactive tricalcium phosphate coating on titanium for load-bearing implants. *Acta Biomaterialia* **4**, 324-333 (2008).
- 36 Chae, J. C., Collier, J. P., Mayor, M. B., Surprenant, V. A. & Dauphinais, L. A. Enhanced ingrowth of porous-coated CoCr implants plasma-sprayed with tricalcium phosphate. *Journal of Biomedical Materials Research* **26**, 93-102 (1992).
- 37 West, G. B. & Brown, J. H. The origin of allometric scaling laws in biology from genomes to ecosystems: towards a quantitative unifying theory of biological structure and organization. *Journal of Experimental Biology* **208**, 1575-1592 (2005).

- 38 West, G. B., Brown, J. H. & Enquist, B. J. A general model for the origin of allometric scaling laws in biology. *Science* **276**, 122-126 (1997).
- 39 West, G. B., Brown, J. H. & Enquist, B. J. The fourth dimension of life: Fractal geometry and allometric scaling of organisms. *Science* **284**, 1677-1679 (1999).
- 40 Banavar, J. R., Maritan, A. & Rinaldo, A. Size and form in efficient transportation networks. *Nature* **399**, 130-132 (1999).
- 41 Prakash, M., Quere, D. & Bush, J. W. M. Surface tension transport of prey by feeding shorebirds: The capillary ratchet. *Science* **320**, 931-934 (2008).
- 42 Zheng, Y. M. *et al.* Directional water collection on wetted spider silk. *Nature* **463**, 640-643 (2010).
- 43 Anfodillo, T., Carraro, V., Carrer, M., Fior, C. & Rossi, S. Convergent tapering of xylem conduits in different woody species. *New Phytologist* **169**, 279-290 (2006).
- 44 Heinzer, S. *et al.* Hierarchical microimaging for multiscale analysis of large vascular networks. *Neuroimage* **32**, 626-636 (2006).
- 45 Zhou, J. *et al.* Elaborate architecture of the hierarchical hen's eggshell. *Nano Research* **4**, 171-179 (2011).
- 46 Seidl, B. *et al.* Ultrastructure and mineral distribution in the tergite cuticle of the beach isopod *Tylos europaeus* Arcangeli, 1938. *Journal of Structural Biology* **174**, 512-526 (2011).
- 47 Nogueiras-Nieto, L., Gómez-Amoza, J., Delgado-Charro, M. B. & Otero-Espinar, F. Hydration and N-acetyl-l-cysteine alter the microstructure of human nail and bovine hoof: Implications for drug delivery. *Journal of Controlled Release* **156**, 337-344 (2011).
- 48 Rubner, M. Materials science: Synthetic sea shell. *Nature* **423**,

- 925-926 (2003).
- 49 Munch, E. *et al.* Tough, bio-inspired hybrid materials. *Science* **322**, 1516-1520 (2008).
- 50 Gao, H., Ji, B., Jäger, I. L., Arzt, E. & Fratzl, P. Materials become insensitive to flaws at nanoscale: Lessons from nature. *Proceedings of the National Academy of Sciences* **100**, 5597-5600 (2003).
- 51 Diekwisch, T. G., Ware, J., Fincham, A. G. & Zeichner-David, M. Immunohistochemical similarities and differences between amelogenin and tuftelin gene products during tooth development. *Journal of Histochemistry & Cytochemistry* **45**, 859-866 (1997).
- 52 Fincham, A. G., Moradian-Oldak, J. & Simmer, J. P. The structural biology of the developing dental enamel matrix. *Journal of Structural Biology* **126**, 270-299 (1999).
- 53 Bernard, G. W. Ultrastructural observations of initial calcification in dentine and enamel. *Journal of ultrastructure research* **41**, 1-17 (1972).
- 54 Katchburian, E. Initiation of mineral deposition in dentine. *Calcified Tissue International* **22**, 179-184 (1976).
- 55 Almuddaris, M. & Dougherty, W. The association of amorphous mineral deposits with the plasma membrane of pre- and young odontoblasts and their relationship to the origin of dentinal matrix vesicles in rat incisor teeth. *American Journal of Anatomy* **155**, 223-244 (1979).
- 56 Leblond, C. & Warshawsky, H. Dynamics of enamel formation in the rat incisor tooth. *Journal of Dental Research* **58**, 950-979 (1979).
- 57 Brudevold, F., Steadman, L. T. & Smith, F. A. Inorganic and organic components of tooth structure. *Annals of the New York*

- Academy of Sciences* **85**, 110-132 (1960).
- 58 Frostell, G., Larsson, S., Lodding, A., Odelius, H. & Petersson, L. SIMS study of element concentration profiles in enamel and dentin. *European Journal of Oral Sciences* **85**, 18-21 (1977).
- 59 Gross, R. Die kristalline Struktur von Dentin und Zahnschmelz. *Festschr Zahn Inst Univ Greifswald*, 59-69 (1926).
- 60 LeGeros, R., Miravite, M., Quiroigico, G. & Curzon, M. The effect of some trace elements on the lattice parameters of human and synthetic apatites. *Calcified Tissue International* **22**, 362-367 (1976).
- 61 Sudarsanan, K. & Young, R. Structure of strontium hydroxide phosphate, $\text{Sr}_5(\text{PO}_4)_3\text{OH}$. *Acta Crystallographica Section B: Structural Crystallography and Crystal Chemistry* **28**, 3668-3670 (1972).
- 62 Jervoe, P. & Lundager, H. E. Calcium phosphates with apatite structure. 1. Precipitation at different temperatures. *Acta Chemica Scandinavica Series a-Physical and Inorganic Chemistry A* **28**, 477-481 (1974).
- 63 Daculsi, G. & Kerebel, B. High-resolution electron microscope study of human enamel crystallites: size, shape, and growth. *Journal of ultrastructure research* **65**, 163-172 (1978).
- 64 Wang, L., Guan, X., Yin, H., Moradian-Oldak, J. & Nancollas, G. H. Mimicking the self-organized microstructure of tooth enamel. *The Journal of Physical Chemistry C* **112**, 5892-5899 (2008).
- 65 Schroeder, L. & Frank, R. High-resolution transmission electron microscopy of adult human peritubular dentine. *Cell and tissue research* **242**, 449-451 (1985).
- 66 Imbeni, V., Kruzic, J., Marshall, G., Marshall, S. & Ritchie, R. The dentin–enamel junction and the fracture of human teeth.

- Nature Materials* **4**, 229-232 (2005).
- 67 Holcomb, D. & Young, R. Thermal decomposition of human tooth enamel. *Calcified Tissue International* **31**, 189-201 (1980).
- 68 Elliott, J. Recent progress in the chemistry, crystal chemistry and structure of the apatites. *Calcified Tissue Research* **3**, 293-307 (1969).
- 69 Dykes, E. & Elliott, J. The occurrence of chloride ions in the apatite lattice of Holly Springs hydroxyapatite and dental enamel. *Calcified Tissue Research* **7**, 241-248 (1971).
- 70 Van der Lugt, W., Knottnerus, D. & Young, R. NMR determination of fluorine position in mineral hydroxyapatite. *Caries Research* **4**, 89-95 (1970).
- 71 Young, R. Mechanism for fluorine inhibition of diffusion in hydroxyapatite. *Nature* **223**, 729-730 (1969).
- 72 Engel, G. & Klee, W. Infrared spectra of the hydroxyl ions in various apatites. *Journal of Solid State Chemistry* **5**, 28-34 (1972).
- 73 Young, R., Bartlett, M., Spooner, S., Mackie, P. & Bonel, G. Reversible high temperature exchange of carbonate and hydroxyl ions in tooth enamel and synthetic hydroxyapatite. *Journal of Biological Physics* **9**, 1-26 (1981).
- 74 Young, R. & Spooner, S. Neutron diffraction studies of human tooth enamel. *Archives of Oral Biology* **15**, 47-63 (1970).
- 75 Pasteris, J. D. *et al.* Lack of OH in nanocrystalline apatite as a function of degree of atomic order: implications for bone and biomaterials. *Biomaterials* **25**, 229-238 (2004).
- 76 Driessens, F., Heyligers, H., Wöltgens, J. & Verbeeck, R. X-ray diffraction of enamel from human premolars several years after eruption. *Journal de biologie buccale* **10**, 199-206 (1982).
- 77 Fosdick, L. & Hutchinson, A. The mechanism of caries of den

- tal enamel. *Annals of the New York Academy of Sciences* **131**, 758-770 (1965).
- 78 Brudevold, F., Aasenden, R. & Bakhos, Y. A preliminary study of posteruptive maturation of teeth in situ. *Caries Research* **16**, 243-248 (1982).
- 79 Featherstone, J., Mayer, I., Driessens, F., Verbeeck, R. & Heijligers, H. Synthetic apatites containing Na, Mg, and CO₃ and their comparison with tooth enamel mineral. *Calcified Tissue International* **35**, 169-171 (1983).
- 80 Kodaka, T., Debari, K. & Abe, M. Hexahedrally based crystals in human tooth enamel. *Caries Research* **26**, 69-76 (1992).
- 81 Lefevre, R., Frank, R. & Voegel, J. The study of human dentine with secondary ion microscopy and electron diffraction. *Calcified tissue research* **19**, 251-261 (1975).
- 82 Marshall, G. W., Balooch, M., Gallagher, R. R., Gansky, S. A. & Marshall, S. J. Mechanical properties of the dentinoenamel junction: AFM studies of nanohardness, elastic modulus, and fracture. *Journal of Biomedical Materials Research* **54**, 87-95 (2001).
- 83 Felix, R. & Fleisch, H. The role of matrix vesicles in calcification. *Calcified tissue research* **21**, 344-348 (1975).
- 84 Bab, I., Muhrad, A. & Sela, J. Ultrastructural and biochemical study of extracellular matrix vesicles in normal alveolar bone of rats. *Cell and tissue research* **202**, 1-7 (1979).
- 85 Herring, G. The organic matrix of bone. *The biochemistry and physiology of bone* **1**, 127-189 (1972).
- 86 Gebauer, D. & Cölfen, H. Prenucleation clusters and non-classical nucleation. *Nano Today* **6**, 564-584 (2011).
- 87 Mahamid, J., Sharir, A., Addadi, L. & Weiner, S. Amorphous calcium phosphate is a major component of the forming fin bo

- nes of zebrafish: Indications for an amorphous precursor phase. *Proceedings of the National Academy of Sciences of the United States of America* **105**, 12748-12753 (2008).
- 88 Dey, A. *et al.* The role of prenucleation clusters in surface-induced calcium phosphate crystallization. *Nature Materials* **9**, 1010-1014 (2010).
- 89 De Jong, W. La substance minerale dans les os. *Recueil des Travaux Chimiques des Pays-Bas* **45**, 445-448 (1926).
- 90 Taylor, N. W. & Sheard, C. Microscopic and X-ray investigations on the calcification of tissue. *Journal of Biological Chemistry* **81**, 479-493 (1929).
- 91 Roseberry, H. H., Hastings, A. B. & Morse, J. X-ray analysis of bone and teeth. *Journal of Biological Chemistry* **90**, 395-407 (1931).
- 92 Hendricks, S. B. & Hill, W. L. The inorganic constitution of bone. *Science* **96**, 255-257 (1942).
- 93 Roufosse, A. H., Landis, W. J., Sabine, W. K. & Glimcher, M. J. Identification of brushite in newly deposited bone mineral from embryonic chicks. *Journal of ultrastructure research* **68**, 235-255 (1979).
- 94 Lörcher, K. & Newesely, H. Calcium carbonate (calcite) as a separate phase besides calcium phosphate apatite in medullary bone of laying hens. *Calcified tissue research* **3**, 358-362 (1969).
- 95 Johnsson, M. S.-A. & Nancollas, G. H. The role of brushite and octacalcium phosphate in apatite formation. *Critical Reviews in Oral Biology & Medicine* **3**, 61-82 (1992).
- 96 Speckman, T. W. & Norris, W. P. Bone crystallites as observed by use of the electron microscope. *Science (New York, NY)* **126**, 753 (1957).
- 97 Fernandez-Moran, H. & Engström, A. Electron microscopy and

- X-ray diffraction of bone. *Biochimica et biophysica acta* **23**, 260-264 (1957).
- 98 Johansen, E. & Parks, H. F. Electron microscopic observations on the three-dimensional morphology of apatite crystallites of human dentine and bone. *The Journal of biophysical and biochemical cytology* **7**, 743-746 (1960).
- 99 Finean, J. & Engström, A. The low-angle scatter of X-rays from bone tissue. *Biochimica et biophysica acta* **11**, 178-189 (1953).
- 100 Carlström, D. & Glas, J.-E. The size and shape of the apatite crystallites in bone as determined from line-broadening measurements on oriented specimens. *Biochimica et biophysica acta* **35**, 46-53 (1959).
- 101 Moore, G. On brushite, a new mineral in phosphatic guano. *American Journal of Science* **39**, 43-44 (1865).
- 102 Lonsdale, K. Human stones limited studies give some details of composition, rates of growth, distribution, and possible causes. *Science* **159**, 1199-1207 (1968).
- 103 Golden, D. C., Stewart, R. B., Tillman, R. W. & White, R. E. Partially acidulated reactive phosphate rock (PAPR) fertilizer and its reactions in soil. 2. mineralogy and morphology of the reaction-products. *Fertilizer Research* **28**, 295-304 (1991).
- 104 Piepenbrink, H. Two examples of biogenous dead bone decomposition and their consequences for taphonomic interpretation. *Journal of Archaeological Science* **13**, 417-430 (1986).
- 105 Beevers, C. The crystal structure of dicalcium phosphate dihydrate, $\text{CaHPO}_4 \cdot 2\text{H}_2\text{O}$. *Acta Crystallographica* **11**, 273-277 (1958).
- 106 Borggreven, J., Driessens, F. & Van Dijk, J. Dissolution and precipitation reactions in human tooth enamel under weak acid conditions. *Archives of Oral Biology* **31**, 139-144 (1986).

- 107 Oliveira, C., Ferreira, A. & Rocha, F. Dicalcium Phosphate Dihydrate Precipitation: Characterization and Crystal Growth. *Chemical Engineering Research and Design* **85**, 1655-1661 (2007).
- 108 Perez, L., Shyu, L. J. & Nancollas, G. H. The phase transformation of calcium phosphate dihydrate into octacalcium phosphate in aqueous suspensions. *Colloids and Surfaces* **38**, 295-304 (1989).
- 109 Zhang, J., Ebrahimpour, A. & Nancollas, G. H. Dual constant composition studies of phase transformation of dicalcium phosphate dihydrate into octacalcium phosphate. *Journal of Colloid and Interface Science* **152**, 132-140 (1992).
- 110 Rowles, S. The precipitation of whitlockite from aqueous solutions. *Bulletin de la Société Chimique de France* **1968**, 802 (1968).
- 111 Shepard, C. U. On two new minerals, monetite and monite, with a notice of pyroclastite. *American Journal of Science* **400-405** (1882).
- 112 Lenart, G., Bidló, G. & Pinter, J. Some basic problems in the examination of the calcium hydrogen phosphates of bone. *Clinical Orthopaedics and Related Research* **83**, 263-272 (1972).
- 113 Dickens, B., Bowen, J. & Brown, W. A refinement of the crystal structure of CaHPO_4 (synthetic monetite). *Acta Crystallographica Section B: Structural Crystallography and Crystal Chemistry* **28**, 797-806 (1972).
- 114 Frèche, M. & Heughebaert, J. Calcium phosphate precipitation in the 60–80 °C range. *Journal of Crystal Growth* **94**, 947-954 (1989).
- 115 Dorozhkin, S. Calcium orthophosphates. *Journal of Materials Science* **42**, 1061-1095 (2007).
- 116 Martin, R. I. & Brown, P. W. Effects of sodium fluoride, potas

- sium fluoride and ammonium fluoride solutions on the hydrolysis of CaHPO_4 at 37.4°C . *Journal of Crystal Growth* **183**, 417-426 (1998).
- 117 LeGeros, R., Daculsi, G., Kijkowska, R. & Kerebel, B. The effect of magnesium on the formation of apatites and whitlockites. *Magnesium in Health and Disease, John Libbey*, 11-19 (1989).
- 118 Elliott, J. Monoclinic space group of hydroxyapatite. *Nature* **230**, 72-72 (1971).
- 119 Elliott, J. C., Mackie, P. & Young, R. Monoclinic hydroxyapatite. *Science* **180**, 1055-1057 (1973).
- 120 Kay, M. I., Young, R. A. & Posner, A. S. Crystal structure of hydroxyapatite *Nature* **204**, 1050-1052 (1964).
- 121 Hata, M., Okada, K., Iwai, S., Akao, M. & Aoki, H. Cadmium hydroxyapatite. *Acta Crystallographica Section B: Structural Crystallography and Crystal Chemistry* **34**, 3062-3064 (1978).
- 122 Hochrein, O., Kniep, R. & Zahn, D. Atomistic simulation study of the order/disorder (monoclinic to hexagonal) phase transition of hydroxyapatite. *Chemistry of materials* **17**, 1978-1981 (2005).
- 123 Suda, H., Yashima, M., Kakihana, M. & Yoshimura, M. Monoclinic \leftrightarrow Hexagonal phase transition in hydroxyapatite studied by X-ray powder diffraction and differential scanning calorimeter techniques. *The Journal of Physical Chemistry* **99**, 6752-6754 (1995).
- 124 Christoffersen, J., Christoffersen, M. R., Kolthoff, N. & Barenholdt, O. Effects of strontium ions on growth and dissolution of hydroxyapatite and on bone mineral detection. *Bone* **20**, 47-54 (1997).
- 125 Yasukawa, A., Kidokoro, M., Kandori, K. & Ishikawa, T. Preparation and characterization of barium–strontium hydroxyapatites.

- Journal of Colloid and Interface Science* **191**, 407-415 (1997).
- 126 Badraoui, B., Aissa, A., Bigi, A., Debbabi, M. & Gazzano, M. Synthesis and characterization of $\text{Sr}_{(10-x)}\text{Cd}_x(\text{PO}_4)_6\text{Y}_2$ (Y = OH and F): A comparison of apatites containing two divalent cations. *Materials Research Bulletin* **44**, 522-530 (2009).
- 127 Pizzala, H. *et al.* A solid-state NMR study of lead and vanadium substitution into hydroxyapatite. *Journal of the American Chemical Society* **131**, 5145-5152 (2009).
- 128 Rodríguez-Lorenzo, L. M., Hart, J. N. & Gross, K. A. Influence of fluorine in the synthesis of apatites. Synthesis of solid solutions of hydroxy-fluorapatite. *Biomaterials* **24**, 3777-3785 (2003).
- 129 Kannan, S., Rebelo, A. & Ferreira, J. M. F. Novel synthesis and structural characterization of fluorine and chlorine co-substituted hydroxyapatites. *Journal of Inorganic Biochemistry* **100**, 1692-1697 (2006).
- 130 Gibson, I. R. & Bonfield, W. Novel synthesis and characterization of an AB-type carbonate-substituted hydroxyapatite. *Journal of Biomedical Materials Research* **59**, 697-708 (2002).
- 131 Gupta, S. K., Rao, P. V. R. & Narasaraju, T. S. B. Physicochemical aspects of calcium vanadate apatite. *Journal of Materials Science* **21**, 161-164 (1986).
- 132 Flis, J., Borkiewicz, O., Bajda, T., Manecki, M. & Klasa, J. Synchrotron-based X-ray diffraction of the lead apatite series $\text{Pb}_{10}(\text{PO}_4)_6\text{Cl}_2\text{-Pb}_{10}(\text{AsO}_4)_6\text{Cl}_2$. *Journal of Synchrotron Radiation* **17**, 207-214 (2010).
- 133 Pan, Y. M. & Fleet, M. E. in *Phosphates: Geochemical, Geological, and Materials Importance* Vol. 48 *Reviews in Mineralogy & Geochemistry* (eds M. J. Kohn, J. Rakovan, & J. M. Hughes) 13-49 (Mineralogical Soc America, 2002).

- 134 Zawacki, S. J., Heughebaert, J. C. & Nancollas, G. H. The growth of nonstoichiometric apatite from aqueous solution at 37°C: II. Effects of pH upon the precipitated phase. *Journal of Colloid and Interface Science* **135**, 33-44 (1990).
- 135 Bonel, G., Heughebaert, J. C., Heughebaert, M., Lacout, J. L. & Lebugle, A. Apatitic calcium orthophosphates and related compounds for biomaterials preparation. *Annals of the New York Academy of Sciences* **523**, 115-130 (1988).
- 136 Meyer, J. L. & Fowler, B. O. Lattice defects in nonstoichiometric calcium hydroxylapatites. A chemical approach. *Inorganic Chemistry* **21**, 3029-3035 (1982).
- 137 Bigi, A. *et al.* Magnesium influence on hydroxyapatite crystallization. *Journal of Inorganic Biochemistry* **49**, 69-78 (1993).
- 138 Fuierer, T. A., Lore, M., Puckett, S. A. & Nancollas, G. H. A mineralization adsorption and mobility study of hydroxyapatite surfaces in the presence of zinc and magnesium ions *Langmuir* **10**, 4721-4725 (1994).
- 139 Amjad, Z., Koutsoukos, P. G. & Nancollas, G. H. The crystallization of hydroxyapatite and fluorapatite in the presence of magnesium-ions. *Journal of Colloid and Interface Science* **101**, 250-256 (1984).
- 140 Dickens, B., Schroeder, L. W. & Brown, W. E. Crystallographic studies of the role of Mg as a stabilizing impurity in β -Ca₃(PO₄)₂. The crystal structure of pure β -Ca₃(PO₄)₂. *Journal of Solid State Chemistry* **10**, 232-248 (1974).
- 141 Welch, J. & Gutt, W. High-temperature studies of the system calcium oxide-phosphorus pentoxide. *Journal of the Chemical Society (Resumed)*, 4442-4444 (1961).
- 142 Descamps, M., Hornez, J. C. & Leriche, A. Effects of powder stoichiometry on the sintering of β -tricalcium phosphate. *Journ*

- al of the European Ceramic Society* **27**, 2401-2406 (2007).
- 143 SPĂȚARU, M., ȚĂRDEI, C., NEMȚANU, M. R. & Bogdan, F.
Rheology of tricalcium phosphate (β -TCP) suspensions. *Revue
Roumaine de Chimie* **53**, 955-959 (2008).
- 144 Jolyon, R. & Ida, C. *Whitlockite*, <<http://www.mindat.org/min-4280.html>> (2013).
- 145 Gopal, R., Calvo, C., Ito, J. & Sabine, W. K. Crystal-structure
of synthetic Mg-whitlockite, $\text{Ca}_{18}\text{Mg}_2\text{H}_2(\text{PO}_4)_{14}$. *Canadian Jour
nal of Chemistry* **52**, 1155-1164 (1974).
- 146 Enderle, R., Götz-Neunhoeffler, F., Göbbels, M., Müller, F. A.
& Greil, P. Influence of magnesium doping on the phase transf
ormation temperature of β -TCP ceramics examined by Rietveld
refinement. *Biomaterials* **26**, 3379-3384 (2005).
- 147 Kuyper, A. C. The chemistry of bone formation I. The compos
ition of precipitates formed from salt solutions. *Journal of Biol
ogical Chemistry* **159**, 411-416 (1945).
- 148 Calvo, C. & Gopal, R. Crystal-structure of whitlockite from pa
lermo quarry. *American Mineralogist* **60**, 120-133 (1975).
- 149 Gee, A. & Deitz, V. R. Pyrophosphate formation upon ignition
of precipitated basic calcium phosphates. *Journal of the Ameri
can Chemical Society* **77**, 2961-2965 (1955).
- 150 Gopal, R. & Calvo, C. Structural relationship of whitlockite an
d beta $\text{Ca}_3(\text{PO}_4)_2$. *Nature-Physical Science* **237**, 30-32 (1972).
- 151 Studart, A. R., Gonzenbach, U. T., Tervoort, E. & Gauckler, L.
J. Processing routes to macroporous ceramics: A review. *Jour
nal of the American Ceramic Society* **89**, 1771-1789 (2006).
- 152 Ohji, T. & Fukushima, M. Macro-porous ceramics: processing
and properties. *International Materials Reviews* **57**, 115-131 (20
12).
- 153 Lin, C., Xiao, C. & Shen, Z. Nano pores evolution in hydroxy

- apatite microsphere during spark plasma sintering. *Science of Sintering* **43**, 39-46 (2011).
- 154 Bernache-Assollant, D., Ababou, A., Champion, E. & Heughebaert, M. Sintering of calcium phosphate hydroxyapatite $\text{Ca}_{10}(\text{PO}_4)_6(\text{OH})_2$ I. Calcination and particle growth. *Journal of the European Ceramic Society* **23**, 229-241 (2003).
- 155 Ramay, H. R. & Zhang, M. Preparation of porous hydroxyapatite scaffolds by combination of the gel-casting and polymer sponge methods. *Biomaterials* **24**, 3293-3302 (2003).
- 156 Roy, D. M. & Linnehan, S. K. Hydroxyapatite formed from coral skeletal carbonate by hydrothermal exchange. *Nature* **247**, 220-222 (1974).
- 157 Liu, D. M. Influence of porosity and pore size on the compressive strength of porous hydroxyapatite ceramic. *Ceramics International* **23**, 135-139 (1997).
- 158 Deville, S., Saiz, E., Nalla, R. K. & Tomsia, A. P. Freezing as a path to build complex composites. *Science* **311**, 515-518 (2006).
- 159 Binner, J. & Reichert, J. Processing of hydroxyapatite ceramic foams. *Journal of Materials Science* **31**, 5717-5723 (1996).
- 160 Sugiyama, K. & Tokonami, M. Structure and crystal chemistry of a dense polymorph of tricalcium phosphate $\text{Ca}_3(\text{PO}_4)_2$: A host to accommodate large lithophile elements in the earth's mantle. *Phys Chem Minerals* **15**, 125-130 (1987).
- 161 Schroeder, L., Dickens, B. & Brown, W. Crystallographic studies of the role of Mg as a stabilizing impurity in $\beta\text{-Ca}_3(\text{PO}_4)_2$. II. Refinement of Mg-containing $\beta\text{-Ca}_3(\text{PO}_4)_2$. *Journal of Solid State Chemistry* **22**, 253-262 (1977).
- 162 Koutsoukos, P., Amjad, Z., Tomson, M. B. & Nancollas, G. H. Crystallization of calcium phosphates. A constant composition

- study. *Journal of the American Chemical Society* **102**, 1553-1557 (1980).
- 163 Ben Abdelkader, S. *et al.* Enthalpie de formation de la whitlockite $\text{Ca}_{18}\text{Mg}_2\text{H}_2(\text{PO}_4)_{14}$. *Journal of thermal analysis and calorimetry* **77**, 863-871 (2004).
- 164 Okazaki, M., Takahashi, J. & Kimura, H. Unstable behavior of magnesium containing hydroxyapatites. *Caries Research* **20**, 324-331 (1986).
- 165 Ryan, L. M. *et al.* Cellular responses to whitlockite. *Calcified Tissue International* **65**, 374-377 (1999).
- 166 Rothwell, W. P., Waugh, J. S. & Yesinowski, J. P. High-resolution variable-temperature phosphorus-31 NMR of solid calcium phosphates. *Journal of the American Chemical Society* **102**, 2637-2643 (1980).
- 167 Verbeeck, R. M. H., De Bruyne, P. A. M., Driessens, F. C. M., Terpstra, R. A. & Verbeeck, F. Solubility Behaviour of Mg-Containing $\beta\text{-Ca}_3(\text{PO}_4)_2$. *Bulletin des Sociétés Chimiques Belges* **95**, 455-476 (1986).
- 168 Martens, C. S. & Harriss, R. C. Inhibition of apatite precipitation in the marine environment by magnesium ions. *Geochimica et Cosmochimica Acta* **34**, 621-625 (1970).
- 169 Nancollas, G., Tomazic, B. & Tomson, M. The precipitation of calcium phosphates in the presence of magnesium. *Croatica Chemica Acta* **48**, 431-438 (1976).
- 170 LeGeros, R., Shirra, W., Miravite, M. & LeGeros, J. Amorphous calcium phosphates: synthetic and biological. *Colloques Internationaux CNRS* **230**, 105-115 (1975).
- 171 Trautz, O. R., Zapantal.R & Legeros, J. P. Effect of magnesium on various calcium phosphates. *Journal of Dental Research* **43**, 751-754 (1964).

- 172 Walser, M. Ion association. VI. Interactions between calcium, magnesium, inorganic phosphate, citrate and protein in normal human plasma. *Journal of Clinical Investigation* **40**, 723-730 (1961).
- 173 Ferron, M. *et al.* Insulin signaling in osteoblasts integrates bone remodeling and energy metabolism. *Cell* **142**, 296-308 (2010).
- 174 Teitelbaum, S. L. Bone resorption by osteoclasts. *Science* **289**, 1504-1508 (2000).
- 175 Silver, I. A., Murrills, R. J. & Etherington, D. J. Microelectrode studies on the acid microenvironment beneath adherent macrophages and osteoclasts. *Experimental Cell Research* **175**, 266-276 (1988).
- 176 Jalota, S., Bhaduri, S. B. & Tas, A. C. In vitro testing of calcium phosphate (HA, TCP, and biphasic HA-TCP) whiskers. *Journal of Biomedical Materials Research* **78A**, 481-490 (2006).
- 177 Monchau, F. *et al.* Calcite as a bone substitute. Comparison with hydroxyapatite and tricalcium phosphate with regard to the osteoblastic activity. *Materials Science and Engineering: C* **33**, 490-498 (2013).
- 178 Ogose, A. *et al.* Comparison of hydroxyapatite and beta tricalcium phosphate as bone substitutes after excision of bone tumors. *Journal of Biomedical Materials Research* **72B**, 94-101 (2005).
- 179 Cho, J. S., Chung, C. P. & Rhee, S. H. Bioactivity and osteoconductivity of biphasic calcium phosphates. *Bioceramics Development and Applications* **1** (2011).
- 180 Yamada, S., Heymann, D., Bouler, J. M. & Daculsi, G. Osteoclastic resorption of calcium phosphate ceramics with different hydroxyapatite/ β -tricalcium phosphate ratios. *Biomaterials* **18**, 1037-1041 (1997).
- 181 Tang, Y. *et al.* TGF- β 1-induced migration of bone mesenchyma

- l stem cells couples bone resorption with formation. *Nature Medicine* **15**, 757-765 (2009).
- 182 Detsch, R., Mayr, H. & Ziegler, G. Formation of osteoclast-like cells on HA and TCP ceramics. *Acta Biomaterialia* **4**, 139-148 (2008).
- 183 Sader, M. S., LeGeros, R. Z. & Soares, G. A. Human osteoblasts adhesion and proliferation on magnesium-substituted tricalcium phosphate dense tablets. *Journal of Materials Science: Materials in Medicine* **20**, 521-527 (2009).
- 184 Webster, T. J., Ergun, C., Doremus, R. H. & Bizios, R. Hydroxylapatite with substituted magnesium, zinc, cadmium, and yttrium. II. Mechanisms of osteoblast adhesion. *Journal of Biomedical Materials Research* **59**, 312-317 (2002).
- 185 Bracci, B. *et al.* Effect of Mg^{2+} , Sr^{2+} , and Mn^{2+} on the chemical-physical and in vitro biological properties of calcium phosphate biomimetic coatings. *Journal of Inorganic Biochemistry* **103**, 1666-1674 (2009).
- 186 Webster, T. J., Massa-Schlueter, E. A., Smith, J. L. & Slamovich, E. B. Osteoblast response to hydroxyapatite doped with divalent and trivalent cations. *Biomaterials* **25**, 2111-2121 (2004).
- 187 Huang, S., Gao, S. & Yu, H. Effect of nano-hydroxyapatite concentration on remineralization of initial enamel lesion in vitro. *Biomedical Materials* **4**, 034104 (2009).
- 188 Niwa, M. *et al.* The adsorptive properties of hydroxyapatite to albumin, dextran and lipids. *Bio-Medical Materials and Engineering* **9**, 163-169 (1999).
- 189 Featherstone, J. D. Prevention and reversal of dental caries: role of low level fluoride. *Community dentistry and oral epidemiology* **27**, 31-40 (1999).
- 190 de La Rica, R. & Stevens, M. M. Plasmonic ELISA for the ul

- trasensitive detection of disease biomarkers with the naked eye. *Nature Nanotechnology* **7**, 821-824 (2012).
- 191 Bejan, A. & Lorente, S. Constructal theory of generation of configuration in nature and engineering. *Journal of Applied Physics* **100** (2006).
- 192 Parker, A. R. & Lawrence, C. R. Water capture by a desert beetle. *Nature* **414**, 33-34 (2001).
- 193 Brookes, M., Elkin, A. C., Harrison, R. G. & Heald, C. B. A new concept of capillary circulation in bone cortex: some clinical applications *The Lancet* **277**, 1078-1081 (1961).
- 194 Dickson, K. M., Bergeron, J. J. M., Philip, A., O'Connor-McCourt, M. & Warshawsky, H. Localization of specific binding sites for ¹²⁵I-TGF-beta1 to fenestrated endothelium in bone and anastomosing capillary networks in enamel organ suggests a role for TGF-beta1 in angiogenesis. *Calcified Tissue International* **68**, 304-315 (2001).
- 195 Zhou, J. *et al.* Elaborate Architecture of the Hierarchical Hen's Eggshell. *Nano Research* **4**, 171-179 (2011).
- 196 Seidl, B. *et al.* Ultrastructure and mineral distribution in the tergite cuticle of the beach isopod *Tylos europaeus* Arcangeli, 1938. *Journal of Structural Biology* **174**, 512-526 (2011).
- 197 Nogueiras-Nieto, L., Gomez-Amoza, J. L., Delgado-Charro, M. B. & Otero-Espinar, F. J. Hydration and N-acetyl-l-cysteine alter the microstructure of human nail and bovine hoof: Implications for drug delivery. *Journal of Controlled Release* **156**, 337-344 (2011).
- 198 Deville, S. Freeze-casting of porous ceramics: A review of current achievements and issues. *Advanced Engineering Materials* **10**, 155-169 (2008).
- 199 Barber, R. W. & Emerson, D. R. Optimal design of microfluid

- ic networks using biologically inspired principles. *Microfluidics and Nanofluidics* **4**, 179-191 (2008).
- 200 Eijkel, J. C. T. Scaling revisited. *Lab on a Chip* **7**, 1630-1632 (2007).
- 201 Balazs, A. C., Emrick, T. & Russell, T. P. Nanoparticle polymer composites: Where two small worlds meet. *Science* **314**, 1107-1110 (2006).
- 202 Gupta, S., Zhang, Q., Emrick, T., Balazs, A. C. & Russell, T. P. Entropy-driven segregation of nanoparticles to cracks in multilayered composite polymer structures. *Nature Materials* **5**, 229-233 (2006).
- 203 Gupta, S., Zhang, Q., Emrick, T. & Russell, T. P. "Self-corraling" nanorods under an applied electric field. *Nano Letters* **6**, 2066-2069 (2006).
- 204 Rasa, H., Mohsen-Nia, M. & Modarress, H. Phase separation in aqueous two-phase systems containing poly(ethylene glycol) and magnesium sulphate at different temperatures. *The Journal of Chemical Thermodynamics* **40**, 573-579 (2008).
- 205 Gosh, R. C. *et al.* The effect of NaCl on the eutectic phase behavior of aqueous poly(ethylene glycol) solutions. *Polymer* **50**, 1304-1310 (2009).
- 206 Snyder, S. M., Cole, K. D. & Szlag, D. C. Phase compositions, viscosities, and densities for aqueous two-phase systems composed of polyethylene glycol and various salts at 25 °C. *Journal of Chemical & Engineering Data* **37**, 268-274 (1992).
- 207 Bailey, F. E. & Callard, R. W. Some properties of poly(ethylene oxide) in aqueous solution. *Journal of Applied Polymer Science* **1**, 56-62 (1959).
- 208 Sakellariou, P., Rowe, R. C. & White, E. F. T. An evaluation of the interaction and plasticizing efficiency of the polyethylene

- glycols in ethyl cellulose and hydroxypropyl methylcellulose films using the torsional braid pendulum. *International Journal of Pharmaceutics* **31**, 55-64 (1986).
- 209 Ozdemir, C. & Guner, A. Solution thermodynamics of poly(ethylene glycol)/water systems. *Journal of Applied Polymer Science* **101**, 203-216 (2006).
- 210 McNamee, C. E., Yamamoto, S. & Higashitani, K. Effect of the physicochemical properties of poly(ethylene glycol) brushes on their binding to cells. *Biophysical Journal* **93**, 324-334 (2007).
- 211 Trimm, D. L. & Stanislaus, A. The control of pore-size in alumina catalyst supports - A review. *Applied Catalysis* **21**, 215-238 (1986).
- 212 Trimble, H. M. & Potts, W. Glycol-water mixtures: Vapor pressure-boiling point-composition relations. *Industrial and Engineering Chemistry* **27**, 66-68 (1935).
- 213 Weidner, E., Wiesmet, V., Knez, Z. & Skerget, M. Phase equilibrium (solid-liquid-gas) in polyethyleneglycol-carbon dioxide systems. *The Journal of Supercritical Fluids* **10**, 139-147 (1997).
- 214 Chaklade, A. C. 'Reactive hot pressing': a new ceramic process. *Nature* **206**, 392-393, (1965).
- 215 Yang, J. F., Zhang, G. J. & Ohji, T. Porosity and microstructure control of porous ceramics by partial hot pressing. *Journal of Materials Research* **16**, 1916-1918 (2001).
- 216 Weibel, A., Bouchet, R., Denoyel, R. & Knauth, P. Hot pressing of nanocrystalline TiO₂ (anatase) ceramics with controlled microstructure. *J. Eur. Ceram. Soc.* **27**, 2641-2646 (2007).
- 217 Carter, D. R. & Hayes, W. C. Bone compressive strength: the influence of density and strain rate. *Science* **194**, 1174-1176 (1976).

- 218 Keller, T. S. Predicting the compressive mechanical behavior of
bone. *Journal of biomechanics* **27**, 1159-1168 (1994).
- 219 Boivin, G. *et al.* The role of mineralization and organic matrix
in the microhardness of bone tissue from controls and osteopo
rotic patients. *Bone* **43**, 532-538 (2008).
- 220 Santos, M. I. & Reis, R. L. Vascularization in bone tissue engi
neering: Physiology, current strategies, major hurdles and future
challenges. *Macromolecular Bioscience* **10**, 12-27 (2010).
- 221 Novosel, E. C., Kleinhans, C. & Kluger, P. J. Vascularization i
s the key challenge in tissue engineering. *Advanced Drug Deliv
ery Reviews* **63**, 300-311 (2011).
- 222 Winet, H. The role of microvasculature in normal and perturbe
d bone healing as revealed by intravital microscopy. *Bone* **19**,
S39-S57 (1996).
- 223 Hollister, S. J. Porous scaffold design for tissue engineering. *N
ature Materials* **4**, 518-524 (2005).
- 224 Tai, K., Dao, M., Suresh, S., Palazoglu, A. & Ortiz, C. Nanos
cale heterogeneity promotes energy dissipation in bone. *Nature
Materials* **6**, 454-462 (2007).
- 225 Burger, E. H. & Klein-Nulend, J. Mechanotransduction in bone
-role of the lacuno-canalicular network. *Federation of American
Societies for Experimental Biology* **13**, S101-S112 (1999).
- 226 Sparreboom, W., van den Berg, A. & Eijkel, J. C. T. Principle
s and applications of nanofluidic transport. *Nature Nanotechno
logy* **4**, 713-720 (2009).
- 227 Sparreboom, W., van den Berg, A. & Eijkel, J. C. T. Transport
in nanofluidic systems: a review of theory and applications. *N
ew Journal of Physics* **12** (2010).